Novel electromagnetic surveying and interpretation methods for improved near surface characterization and deep exploration

by

Michal Kolaj

A thesis submitted in partial fulfillment
of the requirements for the degree of
Doctor of Philosophy (PhD) in Mineral Deposits and Precambrian Geology

The Faculty of Graduate Studies
Laurentian University
Sudbury, Ontario, Canada

THESIS DEFENCE COMMITTEE/COMITÉ DE SOUTENANCE DE THÈSE
Laurentian Université/Université Laurentienne
Faculty of Graduate Studies/Faculté des études supérieures

Title of Thesis Titre de la thèse	Novel electromagnetic surveying and interpretation methods for improved near surface characterization and deep exploration
Name of Candidate Nom du candidat	Kolaj, Michal
Degree Diplôme	Doctor of Philosophy
Department/Program Département/Programme	Mineral Deposits and Precambrian Geology
Date of Defence June 17, 2015 Date de la soutenance	

APPROVED/APPROUVÉ

Thesis Examiners/Examinateurs de thèse:

Dr. Richard Smith
(Supervisor/Directeur(trice) de thèse)

Professor Ben Polzer
(Committee member/Membre du comité)

Dr. Michael Schindler
(Committee member/Membre du comité)

Approved for the Faculty of Graduate Studies
Approuvé pour la Faculté des études supérieures
Dr. David Lesbarrères
Monsieur David Lesbarrères
Acting Dean, Faculty of Graduate Studies
Doyen intérimaire, Faculté des études supérieures

Dr. Colin Farquharson
(External Examiner/Examinateur externe)

Prof. Clarence Virtue
(Internal Examiner/Examinateur interne)

ACCESSIBILITY CLAUSE AND PERMISSION TO USE

Abstract

Inductive electromagnetic (EM) geophysical methods are often applied and their data processed for two different purposes. One is to create images of the distribution of electrical conductivity of the subsurface while the second is to derive simple robust physical estimates of the location, size and attributes of discrete conductors. In order to improve both the ability to efficiently image the subsurface and to derive simple robust physical properties of discrete conductors, several surveying methods and interpretation algorithms have been developed.

To improve the lateral near-surface resolution of thin conductors, such as overburden, nickel laterites and mine waste, two interpretation methods were developed which rely on the measurement of the vertical spatial derivative of the time-varying magnetic field. The first method does not require grid or line data, but, is less accurate than the second inversion method when the spatial gradient of the resistance is strong and/or when the horizontal magnetic fields are large. When applied to data collected over an old mine tailings pond, the two methods produced similar high resolution maps of the conductance.

For both shallow and deep exploration a simple and robust conductance estimation method for borehole EM data was developed. The method relies on the calculation of the vertical spatial derivative of the magnitude of the magnetic field using adjacent down-hole stations. In a field trial, a reliable conductance was calculated for two deep sulfide bodies.

To improve the resolution of EM surveying, a multi-transmitter surveying processing method was developed. Individual targets are highlighted by calculating a weighted-sum of the multiple transmitter data and the method is shown to produce high signal-to-noise ratio data for high-

finesse surveys in complex conductor environments where many transmitter-to-target coupling angles are required and/or for deep focused exploration. A field example over an offset dyke located in the Sudbury Basin showcased the ability of the surveying and processing method to determine the location and orientation of a sulfide body.

To provide geoscientists with low-cost and efficient interpretation tools, a fast approximate 3D inversion for fixed-loop surface data was developed. The method solves for the causative subsurface current system which is approximated with a 3D subsurface grid of 3D magnetic (closed loop current) or electric (current element) dipoles. Ground data from a deep massive sulfide body was inverted and the results were consistent with existing interpretation and a second example over a near-surface mine tailings pond highlighted the strength of being able to invert magnetic field data using either magnetic or electric dipoles.

Keywords

Electromagnetics, mining, environmental, inversion, interpretation, case history, borehole, near-surface, deep exploration

Co-Authorship Statement

This is a manuscript based thesis and the main body (Chapters 3 to 7) is composed of five research papers. Chapters 3 to 5 have been peer-reviewed and published in the journal *Geophysics*. Chapter 6 has been peer-reviewed and accepted to *Geophysics* pending minor revisions. Lastly, a version of Chapter 7 is going to be submitted to a peer-reviewed journal.

All five papers/chapters are co-authored by my supervisor Dr. Richard S. Smith. Dr. Smith proposed the original research, oversaw the research, provided support and advice and had an editorial role in the writing of the papers/chapters.

Acknowledgments

This project would not be possible without the continuous support and guidance from my thesis supervisor, Dr. Richard S. Smith. Richard is the type of supervisor that would always make time for his students and regardless of how simple or complicated your question was he would do his best to set you on the right track. Richard has been a role model for me and any future success I may have as a geophysicist is a reflection of the curiosity he instilled within me.

I would also like to acknowledge the meaningful discussions and advice provided by my committee, Ben Polzer and Dr. Michael Schindler. I am also thankful to the external and internal examiners, Dr. Colin Farquharson and Dr. Clarence Virtue for their value input during my defence.

I am grateful to the financial support provided by the IRC sponsors: the Natural Sciences and Engineering Research Council of Canada (NSERC), Vale, Sudbury Integrated Nickel Operations, a Glencore Company, Wallbridge Mining, KGHM International and the Centre for Excellence in Mining Innovation. In addition to their financial support, the geophysicists and geologists were invaluable in their advice and feedback, in particular: Sean Dickie, Joshua Bailey, Warren Hughes, and Bill Spicer. In addition, the staff of Vale were incredibly helpful, specifically in setting up an office for myself and for their invaluable assistance with the logistics, acquisition, and processing of the field data, in particular, Sean Dickie, Glenn McDowell and John Reipas. MultiLoop III was graciously provided by Lamontagne Geophysics, and Dr. Peter Walker guided me in its use.

I am also thankful to Abitibi Geophysics, in particular, Roman Wasylechko, Pierre Berube, Jonathan Collins, and Eric Gilbert, who supplied assistance, equipment, and personnel that allowed for some of the field data to be collected. Thanks also to Dr. Claire Samson of Carleton University for convincing me to move to Sudbury to study under Richard Smith and for her assistance during the M.Sc. portion of my research.

Furthermore, I am incredibly grateful to the following organizations for the significant scholarships they provided me with: NSERC, the Society of Exploration Geophysicists (SEG) and the Canadian Exploration Geophysical Society (KEGS).

Many thanks is also due to the many friends I made along the way in Sudbury, in particular, Josh Lymburner, Devon Parry, Olaniyan Oladele, Christoph Schaub, Marek Moroz, Remy Poulin, Omid Mahmoodi and Tom Naprstek.

Now take all of those acknowledgements, multiply them by a hundred, and you don't even get close to the amount of thanks that are due to Melanie Hill. She not only put up with my constant neuroticisms, but also proof read every single thing I have ever written (this included). Because of her I have been incredibly fortunate to not have to learn the basic uses of commas and apostrophes.

Lastly, as my doctoral project began as an extension of Richard Smith's M.Sc. thesis, I cannot think of a better to way to end it other than with his final sentence:

> *"Finally, I would like to thank all those who are reading this acknowledgement, as what use would a thesis be if it was never read!*"

Table of Contents

List of Figures

Chapter 1

1 Introduction

1.1 Research motivation

Inductive electromagnetic (EM) methods are routinely applied to study both shallow (e.g. near-surface mineral exploration, geotechnical analysis, environmental and engineering studies) and deep (e.g. mineral exploration, groundwater) geological structures (Palacky, 1987; Fitterman and Labson, 2005; Smith, 2014). The equations which govern inductive EM represent diffusive wave propagation (Grant and West, 1965), and as such, the resolution and maximum depths of exploration are limited by the inherent physics of the method. Furthermore, interpretation of inductive EM surveys (determining the subsurface electrical properties) can be time consuming and often relies on using proprietary software and/or consultants where short turnaround interpretations may not be feasible. The goal of this thesis is to present novel surveying methods which can increase both the near-surface resolution and depth of exploration of inductive EM methods and develop complementary short turnaround methods for the interpretation of inductive EM data.

1.2 Near-surface characterization

The use of spatial derivatives is standard practice in potential field methods (i.e. magnetics and gravity) due to their superior near-surface resolution as the signal from deeper geological bodies

is attenuated (Elkins, 1951; Grant and West, 1965; Hansen et al., 2005). The use of spatial field derivatives of time-varying magnetic fields in EM surveys has also seen notable research in magnetotelluric (MT) geophysics (Jones, 1983; Vozoff, 1991; Patella and Siniscalchi, 1994, and the references therein). Sattel and Macnae (2001) argued that spatial inductive EM derivatives may offer increased resolution to the near-surface conductivity structure and provide noise reduction due to the cancellation of spatially homogenous ambient noise. Several EM gradiometer systems have also been developed for utility and tunnel detection (Bartel et al., 1997; McKenna et al., 2011), but little research has been undertaken in measuring and using spatial EM derivatives on the larger scales required for prospecting or near-surface geological mapping.

One situation in which improved near-surface resolution is required and spatial EM derivatives can be measured is in the characterization of mine tailings. Tailings are the waste material produced after processing ore to extract valuable metals. The processing techniques used to remove base and precious metals from the original rock are not completely effective even today and certainly were not effective over 100 years ago when some of these tailings were first produced (Brown et al., 1999; Marcuson and Diaz, 2007). Thus, the older mine tailings may contain metal concentrations which by today's standard may be economical to extract, and reprocessing them may prove to be an alternate source of easy-to-access metals (Xie et al., 2005). As such, delineating the electrical properties of mine tailings may aid in identifying zones of high concentrations of metals (Chouteau et al., 2006; Lacob and Orza, 2008; Martinez-Pagan et al., 2009; Anterrieu et al., 2010). Furthermore, since some mine tailings are composed of silt to sand-size grains, the metals can seep into the surface contaminating subsurface water and thus their characterization is also important from an environmental standpoint (Aplin and Argall,

1973; Akcil and Koldas, 2006). Finding the metals and reprocessing them will also reduce the potential for seepage in the future.

In Chapters 3 and 4, a frequency domain and a spatial derivative EM survey were performed and interpreted over an old mine tailings pond located in Sudbury, ON, Canada. The spatial derivative measured was the secondary vertical magnetic field (dH_z^s/dz, termed the vertical spatial derivative) which was used in conjunction with new interpretation tools to produce a high resolution map of the laterally varying conductance over the tailings pond (to be discussed further in Section 1.4).

1.3 Deep exploration

With the continual depletion of mineral resources, exploration for deeper ore bodies will be essential in sustaining current mine production levels and future demand for resources. From an EM geophysical exploration point of view, deeper ore bodies present technical challenges as the measured responses from these deep ore bodies are small and often below background noise levels (poor signal-to-noise, S/N, ratio). The main strategy to overcome this issue has been to use large high powered transmitters with large magnetic moments (Zhdanov, 2010). These high moment transmitters increase the S/N ratio of deeper ore bodies by producing larger magnetic fields at greater depths (Nabighian and Macnae, 1991). However, the logistical issues associated with using transmitter wire loops several kilometers in length and transmitter current generators that are very large and cumbersome are often difficult as well as being costly and impractical (Zhdanov, 2010). Furthermore, since the drop-off rate of the magnetic field amplitude of a large transmitter loop approaches an inverse cube relation far from the loop, the transmitter moment has to be increased tremendously to have a noticeable impact on the depth of exploration. As an

example, increasing the transmitter moment by a factor of two by either doubling the transmitter loop area or the transmitted current would only increase the depth of exploration by roughly 25%.

An alternative strategy, originally presented in Lymburner and Smith (2014), which aims to address the issues of depth of penetration for the exploration of deeper ore bodies, is to repeat the profile or grid with many, potentially smaller, transmitters. Chapter 6 revisits and extends the method of Lymburner and Smith (2014) to show how the multiple transmitter data can increase the S/N ratio for high-finesse surveys in complex conductor environments where many transmitter-to-target coupling angles are required and for deep focused exploration. The method is tested with a multiple transmitter survey conducted over an offset dyke in the north-east range of the Sudbury Basin.

1.4 Simple interpretation tools

In inductive EM there are a variety of interpretation methods available and they range from stitched one-dimensional (1D) conductivity-depth sections (either through 1D inversions and/or conductivity depth imaging/transforms; Macnae, 2007) and/or trial-and-error forward modeling whereby the interpreter adjusts synthetic models until the generated synthetic data resembles the field data (Hohmann and Raiche, 1987). While full physics 3D inversions, such as the ones suggested in Haber et al. (2002), Cox et al. (2010), and Oldenburg et al. (2013) are increasing in popularity, their widespread use is limited due to their inherent complexity which restricts their availability and increases their cost (both monetary and in time). As such, many prefer to use simplified approaches whereby the dominant method depends strongly on the system used, the geology and the goal of the survey.

The thin sheet approximation (a parametric model) which assumes that current is constrained to flow in a sheet that is inductively thin (Price, 1949), has been used extensively to simplify the equations used to solve for the electromagnetic fields in 3D media and has been effective in forward modeling and inversion routines (West et al., 1984; Macnae and Lamontagne, 1987; Keating and Crossley 1990; Nabighian and Macnae, 1991; Liu and Asten, 1993; Smith, 2000; Tartaras et al., 2000; Swidinsky and Edwards, 2009). The success of the thin sheet assumption is due to many factors, namely the magnetic fields from a thin sheet are easy to visualize; many mineral exploration targets can be represented as thin sheets (Grant and West, 1965; Palacky 1987); sedimentary layers can, as a first approximation, be thought of as stacked thin sheets (Tartaras et al., 2000; Walker and Lamontagne, 2007) and thin sheets are described by a conductance (product of conductivity and thickness) which is, at times, a more robust parameter to determine than the corresponding conductivity and thickness (Liu and Asten, 1993). The thin sheet approximation is relatively robust and generally valid as long as the thickness of the sheet is smaller than the skin depth or diffusion depth in the frequency and time domain, respectively (Joshi et al., 1988; Frischknecht et al., 1991). As such, while solving the full physics 3D inversion is sometimes preferred in terms of its accuracy, an inversion scheme based on thin sheets is an attractive shortcut in circumstances where the geology is consistent with the inherent assumptions.

Chapters 3 and 4 develop two simple interpretation tools based on the measurement of the vertical spatial field derivative (for improved near-surface resolution) and the thin-sheet approximation. The developed tools can be used to provide a high resolution map of the laterally varying conductance which is useful in many circumstances such as in nickel laterite exploration where the nickel content is, at times, associated with areas of high conductance in the variable

saprolite (Peric, 1981; Rutherford et al., 2001); in the characterization of mine, mill or smelter waste (Chouteau et al., 2006); and/or in the characterization or exploration over variable overburden (Seigel and Pitcher, 1978; Irvine and Staltari, 1984). The two developed methods can be subdivided into 1) an approximate direct transform of the measured data at each station (Chapter 3) and 2) an inversion on gridded data (Chapter 4). Both methods were used to calculate a high spatial resolution laterally varying conductance over an old dry mine tailings pond (described in Section 1.2). An extension and generalization of the direct transform method (to include all vertical derivative components, i.e. $d\mathbf{H}^S/dz$) is also developed for borehole EM data and is tested on several deep massive sulfide targets in Chapter 5.

Another parametric model from which a simple interpretation tool can be developed is the dipole model. The dipole model is considerably less complicated than that the 3D models that describe the full physics and as such they can often be incorporated into automated inversion routines (King and Macnae, 2001; Sattel and Reid, 2006; Smith and Salem, 2007; Schaa and Fullagar, 2010). For example, Smith and Salem (2007) used free-space magnetic dipole look-up tables to fit airborne and ground EM data. Sattel and Reid (2006) used a combination of magnetic dipoles and electric dipoles (cross-strike directed line current) embedded in a layered earth to fit spatially discrete airborne EM anomalies. There is also considerable research into dipole based interpretation within the unexploded ordinance community (Pasion and Oldenburg 2001; Beran et al., 2012 and references therein). While the other work generally fit discrete EM anomalies with single dipoles, using the concepts of moments (Smith and Lee 2001, 2002), Schaa and Fullagar (2010) and Fullagar et al. (2015) developed a 3D inversion which fit resistive-limit EM data using a discretized subsurface grid of magnetic dipoles. By using resistive-limit data, they were able to take full advantage of a potential-field style linear inversion which is significantly

faster than traditional 3D EM inversion. As dipole based inversions can provide significant information at a low cost, it is an attractive choice, especially for preliminary, short turnaround interpretations.

In Chapter 7, a 3D dipole inversion interpretation tool is developed. The method assumes that at a given fixed time, the measured magnetic field (a potential field) can be calculated from the subsurface current distribution at that time and that the current system can be approximated with a 3D subsurface grid of static magnetic dipoles (a unit area circular current loop) or electric dipoles (a small current element). Unlike the approach by Schaa and Fullagar (2010), this approach can determine the amplitude and orientation of the dipoles (which can be either magnetic or electric) at a single time or potentially for a series of times and can therefore provide significant detail about the location and migration of currents in the subsurface. This knowledge can be used as is or as a starting model for more rigorous interpretation. The developed method is tested on a deep massive sulfide body (mineral exploration example) and on the near-surface mine tailings pond discussed in Chapters 2 and 3.

1.5 Thesis arrangement

This is a manuscript based thesis and the main body (Chapters 3 to 7) is composed of five research papers. Chapters 3 to 5 have been peer-reviewed and published in the journal *Geophysics*. Chapter 6 has been peer-reviewed and accepted to *Geophysics* pending minor revisions. Lastly, a version of Chapter 7 is going to be submitted to a peer-reviewed journal. Due to the manuscript nature of this thesis, there is some duplication of information between chapters, especially in introductory material.

This thesis consists of three major topics, near-surface characterization, deep exploration and interpretation tools. Chapter 2 provides fundamental aspects of electromagnetic theory and how they apply to the work discussed in Chapters 3 to 7. Chapters 3 and 4 are related to near-surface characterization and interpretation tools. Chapter 5 and 6 are concerned with deep exploration and interpretation tools. Lastly, Chapter 7 presents a novel interpretation tool (3D dipole inversion) and the examples presented showcase the developed tool for both near and deep subsurface imaging. Chapter 8 summarizes the results of the thesis and provides suggestions for future research.

1.6 Mathematical nomenclature

Unless otherwise stated, a bold letter (i.e. **A**) refers to a vector (lower case) or matrix (upper case). An exception to this rule are the EM vectors, **J**, **E**, **D**, **H** and **B**, which are displayed in upper case bold. Italics are used to denote a scalar quantity (i.e. σ).

1.7 References

Beran, L., B. Zelt, L. Pasion, S. Billings, K. Kingdon, N. Lhomme, L. Song, and D. Oldenburg, 2013, Practical strategies for classification of unexploded ordnance: Geophysics, **78**(1), E41-E46.

Chouteau, M., O. Anterrieu, M. Aubertin, C. Dubreuil-Boisclair, and J. Poisson, 2006, Geophysical characterization of an AMD-generating waste rock pile using ground and borehole techniques: SAGEEP Proceedings 2006, 128-139.

Cox, L. H., G. A. Wilson, and M. S. Zhdanov, 2010, 3D inversion of airborne electromagnetic data using a moving footprint: Exploration Geophysics, **41**, 250–259.

Elkins, A. T., The second derivative method of gravity interpretation: Geophysics, **16**, 29-50.

Fitterman, V. D., and V. F. Labson, 2005, Electromagnetic induction methods for environmental problems, *in* D. K. Butler, ed., Near-Surface Geophysics, 301-356.

Frischknecht, F. C., V. F. Labson, B. R. Spies, and W. L. Anderson, 1991, Profiling methods using small sources, *in* M. N. Nabighian, ed., Electromagnetic methods in applied geophysics, *Applications, Part A and B: SEG, Investigations in Geophysics No. 3, Volume **2**, 105–270.*

Fullagar, P. K., G. A. Pears, J. E. Reid, and R. Schaa, 2015, Rapid approximate inversion of airborne TEM: Exploration Geophysics, **46**, 112-117.

Grant, F. S., and G. F. West, 1965, Interpretation theory in applied geophysics. McGraw-Hill.

Haber, E., D. W. Oldenburg, and R. Shekhtman, 2007, Inversion of time domain three-dimensional electromagnetic data: Geophysical Journal International, **171**, 550–564.

Hansen, R. O., L. Racic, and V. J. S. Grauch, 2005, Magnetic methods in near-surface geophysics, *in* D. K. Butler, ed., Near-Surface Geophysics, 151-175.

Hohmann, G. W., and A. P. Raiche 1987, Inversion of controlled-source electromagnetic data, *in* M. N. Nabighian, ed., Electromagnetic methods in applied geophysics, *Theory, Investigations in Geophysics Volume **1**, 469-503.*

Irvine, R. J., and G. Staltari, 1984, Case history illustrating problems in transient electromagnetic surveys: Exploration Geophysics, **15**, 155-167.

Joshi, M. S., O. P. Gupta, and J. G. Negi, 1988, On the effects of thickness of the half-plane model in HLEM induction prospecting over sulphide dykes in a highly resistive medium: Geophysical Prospecting, **36**, 551– 558.

Keating, P. B., and D. J. Crossley, 1990, The inversion of time-domain airborne electromagnetic data using the plate model: Geophysics, **55**, 705-711.

Liu, G., and M. Asten, 1993, Conductance–depth imaging of airborne TEM data: Exploration Geophysics, **24**, 655– 662.

Macnae, J., 2007, Developments in broadband airborne electromagnetics in the past decade, *in* B. Milkereit, ed., Proceedings of Exploration 07: Fifth Decennial International Conference on Mineral Exploration, 387–398.

Nabighian, M. N., and J. C. Macnae, 1991, Time domain electromagnetic prospecting methods, *in* M. N. Nabighian, ed., Electromagnetic methods in applied geophysics, *Applications, Part A and B: SEG, Investigations in Geophysics No. 3, Volume **2**, 427–520*

Oldenburg, D. W., E. Haber, and R. Shekhtman, 2013, Three dimensional inversion of multisource time domain electromagnetic data: Geophysics, **78**(1), E47-E57.

Palacky, G. J., 1987, Resistivity characteristics of geological targets, *in* M. N. Nabighian, ed., Electromagnetic methods in applied geophysics, *Theory, Investigations in Geophysics Volume **1**, 53-125.*

Pasion, L., and D. Oldenburg, 2001, A Discrimination Algorithm for UXO Using Time Domain Electromagnetics: Journal of Environmental and Engineering Geophysics, **6**, 91-102.

Peric, M., 1981, Exploration of Burundi nickeliferous laterites by electrical methods: Geophysical Prospecting, **29**, 274-287.

Price, A. T., 1949, The induction of electric currents in non uniform thin sheets and shells: Quarterly Journal of Mechanics and Applied Mathematics, **2**, 283-310.

Rutherford, J., T. Munday, J. Meyers, and M. Cooper, 2001, Relationship between regolith materials, petrophysical properties, hydrologeology and mineralisation at the Cawse Ni laterite deposits, Western Australia: Implications for exploring with airborne EM: Exploration Geophysics, **32**, 160-170.

Sattel, D., and J. Reid, 2006, Modelling of airborne EM anomalies with magnetic and electric dipoles buried in a layered earth: Exploration Geophysics, **37**, 254-260.

Schaa, R., and P. K. Fullagar, 2010, Rapid approximate 3D inversion of transient electromagnetic (TEM) data: 80th Annual International Meeting, SEG, Expanded Abstracts, 650–654.

Seigel, H. O., and D. H. Pitcher, 1978, Mapping earth conductivities using a multifrequency airborne electromagnetic system: Geophysics, **43**, 563-575.

Smith, R. S., and A. S. Salem, 2007, A discrete conductor transformation of airborne electromagnetic data: Near Surface Geophysics, **5**, 87-95.

Smith, R. S., 2000, The realizable resistive limit: A new concept for mapping geological features spanning a broad range of conductances: Geophysics, **65**, 1124–1127.

Smith, R.S., and T. J. Lee, 2001, The impulse response moments of a conductive sphere in a uniform field, a versatile and efficient electromagnetic model: Exploration Geophysics, 32, 113-118.

Smith, R. S., and T. J. Lee, 2002, The moments of the impulse response: a new paradigm for the interpretation of transient electromagnetic data: Geophysics, **67**, 1095-1103.

Smith, R. S., 2014, Electromagnetic induction methods in mining geophysics from 2008-2012: Surveys in Geophysics, **35**, 123-156.

Swidinsky, A., and R. N. Edwards, 2009, The transient electromagnetic response of a resistive sheet: straightforward but not trivial: Geophysical Journal International, **179**, 1488–1498.

Tartaras, E., M. S. Zhdanov, K. Wada, A. Saito, and T. Hara, 2000, Fast imaging of TDEM data based on S-inversion: Journal of Applied Geophysics, **43**, 15–32.

Walker, P., and Y. Lamontagne, 2007, Electromagnetic modeling of the Cree Lake Extension Millenium Deposit, with MultiLoop III, *in* B. Milkereit, ed., Proceedings of Exploration 07: Fifth Decennial International Conference on Mineral Exploration, 1077–1080.

West, G. F., J. C. Macnae, and Y. Lamontagne, 1984, A time-domain EM system measuring the step response of the ground: Geophysics, **49**, 1010–1026.

Zhdanov, M. S., 2010, Electromagnetic geophysics: Notes from the past and the road ahead: Geophysics, **75**, No. 5, 75A49-75A66.

Chapter 2

2 Electromagnetic Theory

2.1 Introduction

The following sections describe the fundamental aspects of electromagnetic theory and how they apply to the work discussed in Chapters 3 to 7. Section 2.2 provides a brief overview of Maxwell's equations and the related Laws which govern the electromagnetic phenomenon and how they are used in inductive electromagnetic geophysics. Section 2.3 provides the necessary background and theory for the thin-sheet approximation (an inductively thin conductor) which is used extensively throughout Chapters 3 to 5. Lastly, Section 2.4 derives the necessary equations to calculate the magnetic fields from a magnetic and electric dipole source which is used in Chapters 5 to 7.

2.2 Maxwell's Equations

The EM theory as described below is a brief overview of the main aspects of the EM phenomena which are relevant to inductive EM geophysics and this thesis. A complete description of the theory can be found in Grant and West (1965) and/or Ward and Hohmann (1988) and/or West and Macnae (1991).

Maxwell's equations fully describe the physics of EM fields and, as such, they are a natural starting point to gain insight into how EM fields are used for geophysical applications. In the time domain they are,

$$\nabla \cdot \mathbf{D} = \rho \,, \tag{2-1a}$$

$$\nabla \cdot \mathbf{B} = 0 \,, \tag{2-2a}$$

$$\nabla \times \mathbf{E} = -\frac{\partial \mathbf{B}}{\partial t} \,, \tag{2-3a}$$

and

$$\nabla \times \mathbf{H} = \mathbf{J} + \frac{\partial \mathbf{D}}{\partial t} \,, \tag{2-4a}$$

where the electric field is described via the electric field intensity (**E**) or electric flux density (**D**) vectors and the magnetic field is described using the magnetic field intensity (**H**) or magnetic flux density (**B**) vectors. **J** is the electric current density, ρ is electric charge and t is time. Using Stokes' theorem, Maxwell's equations can also be described in integral form as,

$$\oiint \mathbf{D} \cdot \mathrm{d}\mathbf{S} = \iiint \rho dV \,, \tag{2-1b}$$

$$\oiint \mathbf{B} \cdot \mathrm{d}\mathbf{S} = 0 \,, \tag{2-2b}$$

$$\oint \mathbf{E} \cdot d\mathbf{l} = -\frac{d}{dt} \iint \mathbf{B} \cdot d\mathbf{S} \,, \tag{2-3b}$$

and

$$\oint \mathbf{H} \cdot d\mathbf{l} = \iint \mathbf{J} \cdot d\mathbf{S} + \frac{d}{dt} \iint \mathbf{D} \cdot d\boldsymbol{S} \,, \tag{2-4b}$$

where $\oint$ and $\oiint$ represent closed line and surface integrals, and $\iint$ and $\iiint$ represent surface and volume integrals, respectively. Equations (2-1a) and (2-1b) represent Gauss' Law which states that the total electric flux passing through a closed surface is proportional to the net electric charge (i.e. volume charge) enclosed within that surface. Similarly, Gauss' Law for magnetism

(equations (2-2a) and (2-2b)) states that the total magnetic flux through a closed surface is always zero. Conceptually, these two laws imply that electric fields radiate away from electric charges (monopoles), whereas, magnetic fields flow in a closed loop (i.e. fields from a dipole). These two relationships are illustrated in Figure 2-1.

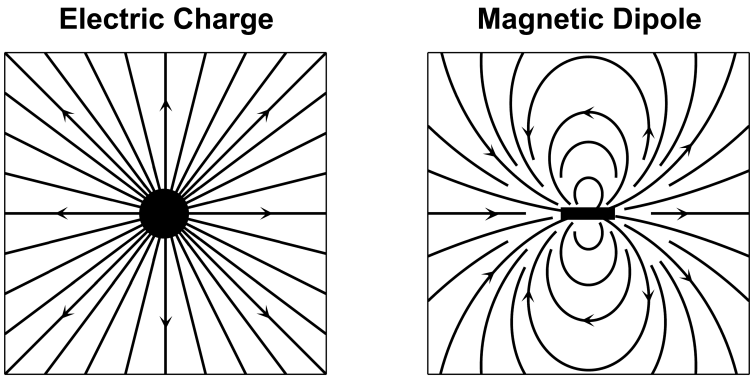

Figure 2-1: Radiation of electric fields from an electric monopole source (left) and magnetic fields from a magnetic dipole source (right) (after West and Macnae, 1991).

Equations (2-3a)/(2-3b) and (2-4a)/(2-4b) are Faraday's Law and Ampere's Law, respectively, and they describe the coupling effect between electric and magnetic fields. Faraday's Law states that a circulating electric field is created around any time varying magnetic field while Ampere's Law states that a circulating magnetic field is created around any electric current density or time-varying electric field. These relationships are illustrated in Figure 2-2.

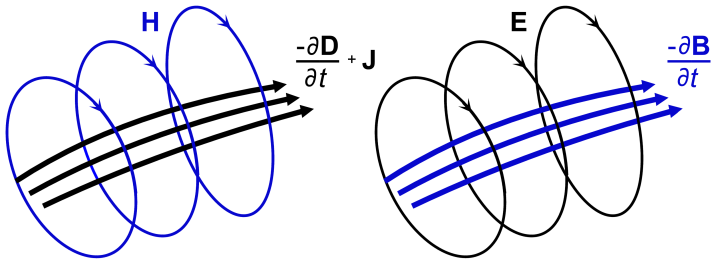

Figure 2-2: Graphical representation of the relationships of electric (black) and magnetic (blue) fields using Ampere's Law (left) and Faraday's Law (right) (after West and Macnae, 1991).

While Maxwell's equations exactly describe EM phenomena, several other relationships, known as the constitutive equations, are required to determine the link between the multiple electric and magnetic field vectors (i.e. **E** and **D** and **B** and **H**, respectively) and the intrinsic properties of materials, namely, the conductivity (σ), magnetic permeability (μ) and the electric permittivity (ε). They are,

$$\mathbf{J} = \sigma\mathbf{E}\,, \tag{2-5}$$

$$\mathbf{B} = \mu\mathbf{H}\,, \tag{2-6}$$

and

$$\mathbf{D} = \epsilon\mathbf{E}\,. \tag{2-7}$$

In order to gain a better understand of how the constitutive equations change Maxwell's equations, they can be substituted into equations (2-3a) and (2-4a) to form,

$$\nabla\times\mathbf{E} = -\frac{\partial}{\partial t}\mu\mathbf{H}\,, \tag{2-8}$$

and

$$\nabla\times\mathbf{H} = \sigma\mathbf{E} + \frac{\partial}{\partial t}\varepsilon\mathbf{E}. \tag{2-9}$$

It is convenient to switch to the frequency domain briefly, whereby, $\frac{\partial}{\partial t}$ is replaced with $i\omega$, where ω is the angular frequency, to form (Keller, 1988),

$$\nabla\times\mathbf{E} = -i\omega\mu\mathbf{H}\,, \tag{2-10}$$

and

$$\nabla\times\mathbf{H} = (\sigma + i\omega\varepsilon)\mathbf{E}. \tag{2-11}$$

Equations (2-10) and (2-11) can be combined for either the **E** or **H** field to make (in a homogenous medium),

$$(\nabla^2 + k^2)\begin{matrix}\mathbf{E}\\ \mathbf{H}\end{matrix} = 0 \tag{2-12}$$

where

$$k^2 = \varepsilon\mu\omega^2 - i\omega\mu\sigma\,. \tag{2-13}$$

As a result, all geo-electric parameters (and frequency) can be grouped into a single term, the wavenumber, *k*, which characterizes the interaction between electromagnetic fields and the medium which they pass through. It can be shown that for the typical frequencies used in inductive electromagnetic geophysics, the real term in equation (2-13) is negligible and the wavenumber can be well approximated with (Grant and West, 1965; Keller, 1988; Ward and Hohmann, 1988; West and Macnae, 1991),

$$k^2 \approx -i\omega\mu\sigma\,. \tag{2-14}$$

This is frequently referred to as the 'quasi-static' approximation as the displacement current term in Ampere's Law (time derivative term in equations (2-4a), (2-4b) and (2-9)) can be neglected due to the removal of the dependence on electric permittivity in equation (2-14). This logic equally holds in the time-domain given that the bandwidth of the electromagnetic systems and the measurement times fall within the zone in which equation (2-14) is considered valid. Another

important note is that most minerals are diamagnetic or paramagnetic, and as such, their magnetic permeability generally differs from the free space value by less than 0.01% (Keller, 1988). Therefore, magnetic permeability can generally be left at its free-space value (μ_0). In contrast to the magnetic permeability, the conductivities of minerals and rocks typically varies over many orders of magnitude. As such, Maxwell's equations, and thus, the measured EM fields in inductive EM geophysics, are primarily a function of the conductivity of the subsurface.

It is important to note that the measured electromagnetic response is not only a function of the electrical properties of the subsurface but also of several intrinsic parameters of the survey methodology. One key parameter is the current waveform in the transmitter which is used to create the primary electromagnetic fields which interact with the subsurface. Mathematically, the magnetic field response of the subsurface, $H(t)$, is equal to the impulse response of the subsurface, $I(t)$, convolved by the transmitter current waveform, $S(t)$, generated by the transmitter, i.e.,

$$H(t) = A\int_{-\infty}^{\infty} S(\eta)I(t-\eta)d\eta \tag{2-15}$$

where η is a dummy integration variable, and A is a scalar coupling factor. Equation (2-15) is general and vector notation could be used when there are multiple components in the vector fields (i.e. x, y and z in the Cartesian coordinate system). As evident in equation (2-15), the magnetic field response is essentially a sum of a train of impulse responses scaled by the shape of the transmitter current waveform. As such, different waveforms will produce different responses and an understanding of how different waveforms will affect the measured response is often critical to optimizing and interpreting electromagnetic surveys. The properties of time-domain waveforms can vary from system to system and from survey to survey and example

waveforms and waveform parameters and shapes are depicted in Figures 2-3 and 2-4. The pulse width is the duration (in seconds) of the on-time (non-zero transmitter current) portion of the waveform, the duty cycle is the percentage of the on-time period relative to the off-time and the frequency is the repetition rate of the bipolar waveform in Hz. Additionally, the shape of the waveform is also important; in Figure 2-3 a square waveform is used. Other typical waveforms include: exponential turn-on linear-ramp off, half-sine and triangle (Figure 2-4). In frequency domain surveying, the current waveform is a full-duty sine/cosine wave.

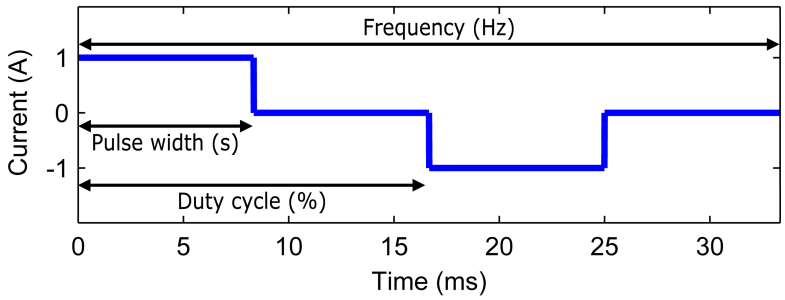

Figure 2-3: A 30 Hz (frequency), 8.33 ms (pulse width), 50 % (duty cycle) square current waveform.

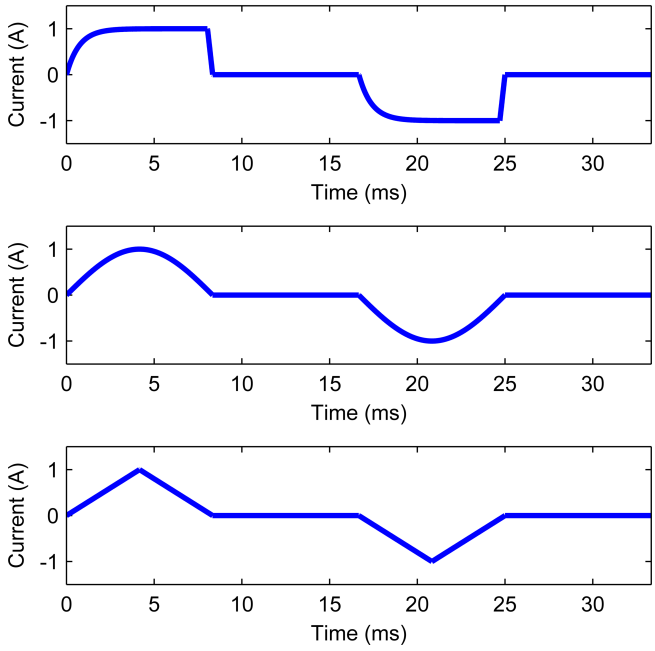

Figure 2-4: Other frequently used current waveforms in electromagnetic prospecting. Top: exponential turn-on linear ramp-off. Middle: half-sine. Bottom: triangle.

As the general theory and concepts behind inductive EM are now explained, the surveying principles can be briefly described. A time-varying magnetic field is created via Ampere's Law (equation (2-4a)) by a wire-loop connected to a waveform generator and a power source. Where such a field is created in the absence of any conductive material it is termed the primary field $\mathbf{H}^P$. Where the time-varying magnetic field encounters conductive material, a current density is induced via Faraday's Law and Ohm's Law (equations (2-3a) and (2-5), respectively). This induced current will initially be confined to the surface of the conductor, but with the passage of time, it will begin to dissipate and the currents will begin to diffuse into the conductor. Furthermore, the induced currents produce their own magnetic field via Ampere's Law (termed the secondary field, $\mathbf{H}^S$). This secondary field (or the total field, $\mathbf{H}$, i.e. $\mathbf{H}^P + \mathbf{H}^S$) is then

measured at many locations (either in the air, at the surface or in a borehole) using either a magnetometer (response proportional to **H**) or coil (response proportional to $d\mathbf{H}/dt$) sensor and averaged over distinct time channels/windows (or a measurement of the in-phase and quadrature component in frequency domain surveying). Time windows rather than instantaneous measurements are made so as to average the response over several adjacent samples. The time windows are generally narrower close to the switch-off or switch-on of the transmitter current waveform in order to sample any quickly decaying secondary fields. Since the current waveform is periodic, this process is repeated and the results are averaged over several wave periods (i.e. boxcar stacking). The goal of inductive EM interpretation is to determine the subsurface conductivity distribution which produced the measured field.

2.3 Non-uniform conductive thin sheet

Electromagnetic induction in a thin sheet was studied by Price (1949) and the theory as outlined here follows his work and that of Grant and West (1965) and Smith and West (1987). A thin sheet is an idealized conductor shape whereby the conductor is assumed to be "inductively thin". This approximation is valid as long as the thickness of the sheet is smaller than one-half the skin depth in the frequency domain or diffusion depth in the time domain (Joshi et al., 1988; Frischknecht et al., 1991). The thin sheet approximation allows for a reasonably simple relationship between the secondary magnetic field ($\mathbf{H}^S$) and the total magnetic field, **H**, to be derived for a thin sheet in a non-conductive medium.

Let us consider any flat thin sheet with a non-uniform distribution of conductive material with a non-conductive medium on either side. This sheet's extent may be infinite or bounded and is assumed to have a sufficiently large conductivity (σ) such that even if its thickness (d)

approaches zero, the product, σd (conductance), remains finite. For convenience, let this sheet be in the $z = 0$ plane in a Cartesian coordinate system. The resistance (R) can be thus defined as

$$R = \frac{1}{\sigma\, d}. \tag{2-16}$$

Let us assume this sheet is excited by a time-varying primary magnetic field ($\mathbf{H}^P$) that is due to currents external to the sheet such that electric currents are induced in the sheet. Since the currents will be confined within the sheet, we can define a surface current ($\mathbf{K}$) using Ohm's Law (2-5) as

$$\mathbf{K} = \mathbf{J}d = \frac{\mathbf{E}}{R}. \tag{2-17}$$

The boundary conditions which apply to a thin sheet are as follows: the primary field ($\mathbf{H}^P$) and the normal component of the secondary component ($\mathbf{H}^S$) must be continuous through the sheet and the symmetrical properties of the field (around the surface current, $\mathbf{K}$) suggest the tangential components of the $\mathbf{H}^S$ will change in sign (i.e. both H^S_x and H^S_y will be equal in magnitude, but opposite in sign on the negative and positive sides of the sheet). These conditions can be mathematically written as

$$\mathbf{H}^P_+ - \mathbf{H}^P_- = 0\,, \tag{2-18a}$$

$$\mathbf{n} \cdot (\mathbf{H}^S_+ - \mathbf{H}^S_-) = 0\,, \tag{2-18b}$$

and

$$\mathbf{n} \times (\mathbf{H}^S_+ + \mathbf{H}^S_-) = 0 \tag{2-18c}$$

where the positive and negative subscripts represent the field above (+) and below (-) the sheet respectively, and $\mathbf{n}$ is the vector normal to the sheet (Grant and West, 1965).

We can apply the quasi-static Ampere's Law (equation (2-4b) without displacement current) to an infinitesimally small rectangular circuit, with two horizontal sides of length, *dl*, that are parallel to the sheet (one above and one below, Figure 2-5) at an angle of θ with **K**. The other two edges are vertical and normal to the sheet and by the boundary conditions in equation (2-18), their contributions to the closed line integral in equation (2-4b) will be zero since $H^S_{z+} - H^S_{z-} = 0$ (alternatively, the vertical side in the circuit could be made small enough such that the contribution from the vertical component is negligible, Figure 2-5), so we obtain

$$dl\left(\left|\mathbf{H}^s_{(x,y)+}\right| - \left|\mathbf{H}^s_{(x,y)-}\right|\right) = |\mathbf{K}| dl \sin\theta \,, \tag{2-19}$$

where | | represents the magnitude of the respective vector and $\mathbf{H}^S_{(x,y)}$ is the horizontal component of the secondary magnetic field.

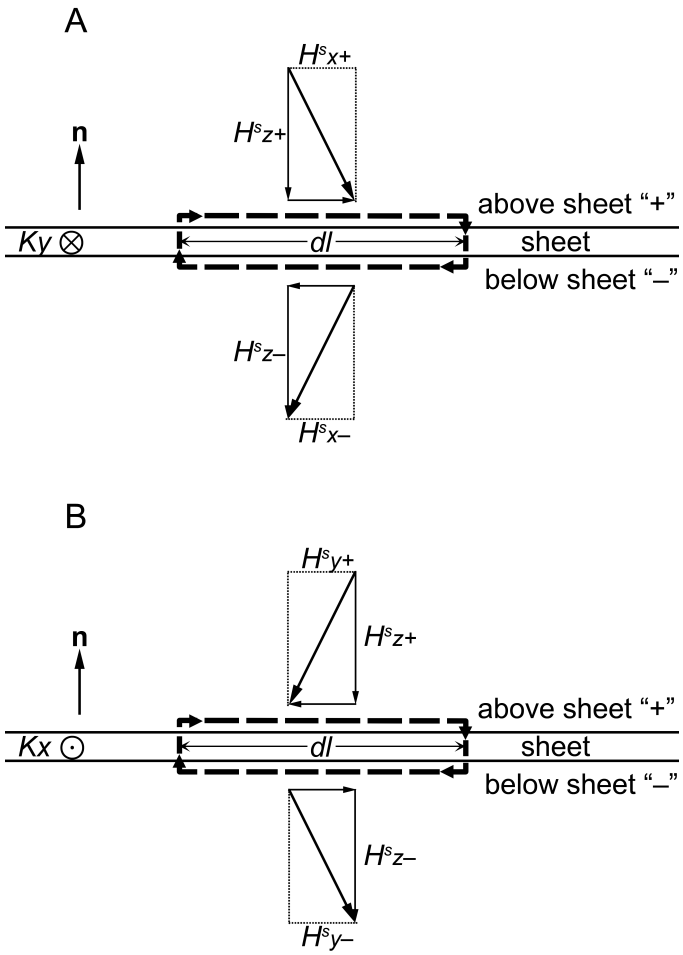

Figure 2-5: The thin sheet model illustrating the surface current, **K**, on a horizontal sheet in the $z = 0$ plane, which generates the secondary field, $\mathbf{H}^S$ (H^S_x, H^S_y and H^S_z). The path, upon which the line integral is calculated for Ampere's Law, is denoted with a thick dashed line. The secondary magnetic field is drawn for two cases: Panel A shows H^S_x when K_y is oriented into the page and panel B shows H^S_y when K_x is oriented out of the page. In both cases $\theta = 90°$ to produce only one surface current and secondary horizontal magnetic field component.

Since equation (2-19) is valid for all values of θ, the two components of the surface current (K_x and K_y) can be obtained and, by applying the boundary conditions listed in equation (2-18) (i.e. $H^S_{x+} = -H^S_{x-}$ and $H^S_{y+} = -H^S_{y-}$, Figure 2-5), the positive and negative contributions from the horizontal magnetic field components can be summed to yield

$$K_x = -2H^s_{y+}\,, \tag{2-20}$$

and

$$K_y = 2H^s_{x+}\,, \tag{2-21}$$

where the difference in sign in front of H^S_{x+} and H^S_{y+} can be visualized by applying the right-hand rule to a simple one directional current.

Lastly, applying Faraday's Law (equation (2-3a)) on the surface of the sheet, the normal component (**n**) may be written as

$$\frac{\partial E_y}{\partial x} - \frac{\partial E_x}{\partial y} = -\mu \frac{\partial H_z}{\partial t}\,. \tag{2-22}$$

The necessary relationship for $\mathbf{H}^S$ to **H** can be obtained by incorporating equations (2-20) and (2-21) into the alternative form of Ohm's Law (equations (2-17)) and placing the resultant into equation (2-22) to form,

$$2\left[\frac{\partial\left(RH^s_{y+}\right)}{\partial y} + \frac{\partial(RH^s_{x+})}{\partial x}\right] = -\mu \frac{\partial H_z}{\partial t}\,. \tag{2-23}$$

The derivative product rule means that the two derivatives in equation (2-23) yield four terms, two of which involve derivatives of the resistance multiplied by the fields. The other two involve derivatives of the horizontal fields multiplied by the resistance. These horizontal field derivatives can be converted into a single vertical spatial derivative using Gauss' Law for magnetism

(equation (2-2a)). By dropping the positive subscript, +, (since all measurements are made above the sheet) we can then obtain

$$-\frac{\partial H_z^s}{\partial z}R + \frac{\partial R}{\partial y}H_y^s + \frac{\partial R}{\partial x}H_x^s = -\frac{\mu}{2}\frac{\partial H_z}{\partial t}. \tag{2-24}$$

Equation (2-24) provides our required link between the measured magnetic fields and the resistance at any point along the sheet.

2.4 Magnetic fields from a dipole source

Magnetic and electric dipoles are frequently used as the sources of electromagnetic fields and potentially as interpretation tools by approximating a conductive body with that of one or many dipoles. In order to solve for the magnetic fields from a dipole source, it is convenient to reduce the number of unknowns by using a vector potential from which the electric and magnetic fields can be derived (Grant and West, 1965). The vector potential most frequently used is the magnetic vector potential, **A**,

$$\mathbf{B} = \nabla\times\mathbf{A} \tag{2-25}$$

which automatically satisfies Gauss' Law for magnetism (equation (2-2a)) as the divergence of the curl of any vector field is always zero. By inserting equation (2-25) into Faraday's Law (equation (2-3a)), it allows us to observe that,

$$\mathbf{E} = -\frac{\partial \mathbf{A}}{\partial t}. \tag{2-26}$$

Replacing both **E** and **B** fields with **A** in the quasi-static form of Ampere's Law and using the identity, $\nabla \times \nabla\times\mathbf{A} = \nabla(\nabla \cdot \mathbf{A}) - \nabla^2\mathbf{A}$, (where $\nabla \cdot \mathbf{A} = 0$) gives,

$$\nabla^2 \mathbf{A} = -\mu \mathbf{J}, \tag{2-26}$$

which is Poisson's equation which has the solution,

$$\mathbf{A}(\mathbf{s}) = \frac{\mu}{4\pi} \int \frac{\mathbf{J}(\mathbf{r})}{|\mathbf{s} - \mathbf{r}|} d^3 r, \tag{2-27}$$

where **s** is the position where **A** is to be calculated and **r** is the position of the current density element (**J**). Taking the curl of equation (2-27) and setting $\mathbf{J}(\mathbf{r})\, d^3r = Id\mathbf{l}$ (i.e. thin current carrying wire as opposed to a volume current) gives the classical formulation of Biot-Savart's Law,

$$\mathbf{B}(\mathbf{s}) = \frac{\mu}{4\pi} \oint \frac{Id\mathbf{l} \times (\mathbf{r} - \mathbf{s})}{4\pi |\mathbf{r} - \mathbf{s}|^3}, \tag{2-28}$$

where I is the magnitude of the current and $d\mathbf{l}$ is a unit vector in the direction of the current.

In this work, an electric dipole is an infinitesimal line current element $Id\mathbf{l}$ (similar definition can be found in Ward and Hohmann, 1988) whose magnetic field can be directly calculated from the current element in equation (2-28. Furthermore, the fields due to a magnetic dipole source (an infinitesimally small current carrying loop) can be found by solving equation (2-28) over a unit circle which has the general solution for an arbitrary directed dipole (Grant and West, 1965),

$$\mathbf{B}(\mathbf{s}) = \frac{|\mathbf{m}|}{4\pi |\mathbf{r} - \mathbf{s}|^3} \left[\frac{3\, \hat{\mathbf{m}} \cdot (\mathbf{r} - \mathbf{s})}{|\mathbf{r} - \mathbf{s}|^2} (\mathbf{r} - \mathbf{s}) - \hat{\mathbf{m}} \right], \tag{2-29}$$

where $|\mathbf{m}|$ is equal to the magnetic dipole moment of the dipole (for a current carrying loop this is equal to the current multiplied by the area) and $\hat{\mathbf{m}}$ is equal to the unit vector of the magnetic dipole direction.

2.5 References

Frischknecht, F. C., V. F. Labson, B. R. Spies, and W. L. Anderson, 1991, Profiling methods using small sources, *in* M. N. Nabighian, eds., Electromagnetic methods in applied geophysics, *Applications, Part A and B: SEG, Investigations in Geophysics No. 3, Volume **2**, 105–270.*

Grant, F. S., and G. F. West, 1965, Interpretation theory in applied geophysics. McGraw-Hill.

Joshi, M. S., O. P. Gupta, and J. G. Negi, 1988, On the effects of thickness of the half-plane model in HLEM induction prospecting over sulphide dykes in a highly resistive medium: Geophysics Prospecting, **36**, 551-558.

Keller, G.V, 1988, Rock and Mineral Properties, *in* M. N. Nabighian, ed., Electromagnetic methods in applied geophysics: theory, SEG, Volume **1**, 13-51.

Nabighian, M. N., and J. C. Macnae, 1991, Time domain electromagnetic prospecting methods, *in* M. N. Nabighian, eds., Electromagnetic methods in applied geophysics, *Applications, Part A and B: SEG, Investigations in Geophysics No. 3, Volume **2**, 427–520.*

Price, A. T., 1949, The induction of electric currents in non uniform thin sheets and shells: Quarterly Journal of Mechanics and Applied Mathematics, **2**, 283-310.

Smith, R. S., and G. F. West, 1987, Electromagnetic induction in an inhomogeneous conductive thin sheet: Geophysics, **52**, 1677-1688.

Ward, S. H., and G. W. Hohmann, 1988, Electromagnetic theory for geophysical applications, *in* M. N. Nabighian, ed., Electromagnetic methods in applied geophysics: theory, SEG, Volume **1**, 130–311.

West, G. F., and J. C. Macnae, 1991, Physics of the electromagnetic induction exploration method, *in* M. N. Nabighian, eds., Electromagnetic methods in applied geophysics, *Applications,* Part A and B: SEG, Investigations in Geophysics No. 3, Volume **2**, 5-45.

Chapter 3

3 Using spatial derivatives of electromagnetic data to map lateral conductance variations in thin sheet models: applications over mine tailings ponds

3.1 Abstract

Mine waste, variable overburden or the saprolite associated with nickel laterites have a conductivity thickness (conductance) that varies laterally. In order for electromagnetic methods to be used to easily map lateral changes in conductance over thin sheet like bodies such as these, a simple conductance estimation method has been developed from Price's equation. Through forward modeling we show that assuming a uniform conductance and solving for an apparent conductance is sensitive enough to identify lateral conductance changes. The method does not require knowledge of the transmitted waveform or the location of the transmitter and each measurement provides a direct estimate of the apparent conductance below that station. The receiver can be moved around quickly allowing for lateral variations in apparent conductance to be determined efficiently. However, one of the required terms in the equation used is the vertical derivative of the secondary vertical magnetic field (dH_z^s/dz). The accurate measurement of spatial electromagnetic derivatives requires a good signal-to-noise (S/N) ratio which can be hampered by low derivative signal values. Field studies performed over a dry tailings pond in Sudbury, Ontario, Canada showed that a S/N ratio greater than 3 was achievable even with dH_z^s/dz values of less than 0.5 pT/(Am). Apparent conductance estimates revealed that the

tailings had a large resistive zone associated with surface vegetation which may be correlated with favorable growing conditions and/or less conductive or thinner tailing material. Larger apparent conductances in other areas may be related to zones of thicker tailings and/or more conductive material (possibly due to increased metal content). Further drilling and sampling work is required to answer these ambiguities. Regardless, mapping the conductance of a thin sheet is an important step towards assessing if there are remaining metals in mine waste. However, the developed method is general and can be used in many other situations involving laterally varying thin bodies.

3.2 Introduction

Mapping terrain with laterally varying conductivity using electromagnetic (EM) geophysical techniques is a potentially important step in characterizing mine waste, exploring over variable overburden or in the characterization of the saprolite associated with nickel laterites. One way of simplifying the interpretation of this data is to use the thin sheet approximation which assumes that all the induced current is constrained to flow in the plane of the sheet (Grant and West, 1965). This assumption has proven to be effective in modeling and inversion as it allows for simplifications in the equations which describe the interactions between EM fields and the medium (Price, 1949; Grant and West, 1965; West et al., 1984; Macnae and Lamontagne, 1987; Nabighian and Macnae, 1991; Smith, 2000; Swidinsky and Edwards, 2009).

However, variations in conductance (product of conductivity and thickness) within the sheet are often not considered and many modeling routines do not allow for such variations which is non-ideal and may produce erroneous and/or misleading results in situations where the thickness and/or conductivity of the sheet varies laterally. Such variations would be expected in

exploration over variable overburden (Irvine and Staltari, 1984), nickel laterite exploration (Peric, 1981; Rutherford et al., 2001) or in the characterization of mine, mill or smelter waste (Chouteau et al., 2006). The electromagnetic induction in a thin sheet with laterally varying conductance obeys a differential equation derived by Price (1949). Smith and West (1987) adapted the equation for EM prospecting and created a computational method to calculate the EM response of a sheet with variable conductance, however no inversion based on this method has been developed. One of the terms in the equation is the vertical derivative of the secondary vertical magnetic field (dH_z^s/dz), termed the vertical spatial derivative henceforth. Spatial EM derivatives can be approximated with a finite difference operator (using two sensors and taking the difference between their individual measurements). As the difference in the field can be small, the sensors must be sensitive with low instrument noise levels.

Sattel and Macnae (2001) argued that spatial EM derivatives may offer increased resolution to the near-surface conductivity structure and provide noise reduction due to the cancellation of EM noise that varies slowly spatially, such as the electromagnetic impulses of "spherics" or distant lightning strikes or the magnetic fields from distant power lines (i.e. spatially homogenous noise). However, the measurements are hampered by non-spatially homogenous noise or noise which originates within the individual sensors used to estimate the spatial derivative (i.e. thermal noise of a sensor coil or the electronics from the receiver). The use of spatial magnetic field derivatives has seen notable research in magnetotelluric (MT) geophysics (Jones, 1983; Vozoff, 1991; Patella and Siniscalchi, 1994, and the references therein) which is not surprising considering that the electric field used in the standard MT ratio (impedance) resistivity calculation (Vozoff, 1991) can be expressed in terms of spatial magnetic field derivatives via Ampere's Law. Several EM gradiometer systems have also been developed for utility and tunnel

detection (Bartel et al., 1997; McKenna et al., 2011), but little research has been undertaken in measuring and using spatial EM derivatives on the larger scales required for prospecting purposes.

One of the situations where spatial EM derivatives should be measureable and where a simple method to map lateral variations in conductance is useful is in the characterization of mine tailings. Tailings are the waste material produced after processing ore to extract valuable metals. The mine tailings waste dumps can be as large as several kilometers in length and several tens of meters in height and are found close to mines and mine processing facilities. The processing techniques used to remove the base and precious metals of interest from the original rock are not completely effective even today and certainly were not over 100 years ago when some of these tailings were first produced (Brown et al., 1999; Marcuson and Diaz, 2007). Thus, the older mine tailings may contain metal concentrations which by today's standard may be economical to extract and reprocessing them may prove to be an alternate source of easy-to-access metals (Xie et al., 2005). As such, delineating the electrical proprieties of mine tailings may aid in identifying zones of high concentrations of metals (Chouteau et al., 2006; Lacob and Orza, 2008; Martinez-Pagan et al., 2009; Anterrieu et al., 2010). Furthermore, since some mine tailings are composed of silt to sand-size grains, the metals can seep into the surface and subsurface water and thus their characterization is also important from an environmental standpoint (Aplin and Argall, 1973; Akcil and Koldas, 2006). The delineation of the structure of mine tailings will not only allow for the potential reprocessing of remaining metals (which will reduce the potential for seepage in the future) but may also prove valuable to the understanding of the internal processes occurring within them (i.e. fluid/metal migration). The EM geophysical data may not be able to distinguish between enhanced conductance due to changes in thickness or conductivity and

increased clay, water or metal content. However, these ambiguities can be solved through drilling and sampling work on areas of interest identified by the geophysical work.

In this paper, the solution to the problem of electromagnetic induction in laterally varying thin sheets is simplified to require only two measured quantities from which the conductance of the sheet can be calculated. In addition, forward modeling is used to generate typical apparent conductance results at various conductances. Lastly, we present results from field data collected overtop a laterally extensive dry mine tailings pond (variably covered by vegetation and hay) situated on Vale property in Sudbury, Ontario, Canada, where the vertical spatial derivative of the magnetic field was measured during an inductive time-domain electromagnetic (TDEM) survey.

3.3 Theory

In the thin sheet approximation, the sheet's thickness is considered small enough such that the current density induced in the sheet by the exciting primary magnetic field, $\mathbf{H}^P$, is constrained to flow in the plane of the sheet (i.e. no current flow normal to the sheet, Price, 1949). Such a sheet is often referred to as being "inductively thin". This condition is valid as long as the thickness of the sheet is smaller than one-half the skin depth in the frequency domain or diffusion depth in the time domain (Joshi et al., 1988; Frischknecht et al., 1991). This approximation allows for a reasonably simple relationship between the secondary magnetic field ($\mathbf{H}^S$) and the total magnetic field, $\mathbf{H}$ (i.e. $\mathbf{H}^P + \mathbf{H}^S$), to be derived for a flat-lying thin sheet in a non-conductive medium (Price, 1949; Smith and West, 1987),

$$-\frac{dH_z^s}{dz}R+\frac{dR}{dy}H_y^s+\frac{dR}{dx}H_x^s=-\frac{\mu}{2}\frac{dH_z}{dt}, \tag{3-1}$$

where μ is the magnetic permeability, $R(x,y)$ is the resistance of the sheet (the resistance directly below the measurement point (x,y)), and the variables dH_z^s/dz, H_y^s, H_x^s and dH_z/dt are measured directly above (or below) the sheet. As a result of having a vanishing thickness, the sheet is represented by a single parameter, the resistance (product of resistivity and thickness, inverse of conductance) rather than two parameters, the resistivity and thickness. As such, in realistic scenarios where the sheet has a thickness but the thin sheet approximation is still valid, both the thickness and resistivity information are incorporated into the resistance value.

Equation (3-1) can be simplified if we assume that the sheet is infinite in extent and that the resistance is constant in the x and y direction, i.e. set dR/dy and dR/dx equal to zero such that equation (3-1) reduces to

$$\frac{dH_z^s}{dz}R=\frac{\mu}{2}\frac{dH_z}{dt}. \tag{3-2}$$

If the vertical spatial derivative (dH_z^s/dz) and the vertical component time derivative (dH_z/dt) are sensitive to lateral changes in resistance and the terms with resistance derivatives in the lateral direction in equation (3-1) are very small (i.e. $H_y^s dR/dy \approx 0$ and $H_x^s dR/dx \approx 0$), then equation (3-2) can also be used to estimate the "apparent resistance" in sheets where the resistance varies laterally. This apparent resistance assumes a thin sheet model with a uniform resistance (equation (3-2)) in the same way that apparent resistivity in the DC resistivity method normally assumes a

uniform half-space model. If viable, this simplification implies that laterally variable resistance could be determined experimentally (or analytically) at each location by measuring only the vertical component of the magnetic field at two heights. Only one transmitter would be required (either on the ground or in the air) and the receiver could be moved around quickly allowing for lateral variations in apparent resistance to be determined efficiently using equation (3-2). A further simplification can be achieved by setting dH_z^P/dt equal to zero (all terms become secondary magnetic fields). This is true in the off time or when the transmitted waveform has a constant valued magnetic field (i.e. $dH_z^P/dt = 0$). As such, the location and properties of the transmitter do not need to be known in order to solve equation (3-2). Furthermore, since there is no explicit dependence on time in equation (3-2), multiple resistance profiles can be calculated, one for each time channel. The apparent resistance calculated using different time channels should be equal if the inductively thin sheet and uniform resistance approximations are valid. If the solution to equation (3-2) at $t = 0$ s is $H^s(x,y,z)$, then $H^s(x,y,z+vt)$ is the solution at $t > 0$ where the velocity, v, is equal to $2R/\mu$. This is known as the Maxwell retreating image solution (Grant and West, 1965; Smith and West, 1987). Inspection of equation (3-2) reveals that v is equal to dH_z^s/dt divided by dH_z^s/dz which makes physical sense as the time derivative describes the change in the vertical magnetic field as a function of time while the vertical derivative describes the change with distance. A direct consequence is that equation (3-2) is thus valid at any distance away from the sheet. Similarly, equation (3-2) has no explicit dependence on depth, but dH_z^s/dz will inherently limit the applicability of this method for non near-surface targets as dH_z^s/dz from deeper targets will become obscured in background noise levels. Lastly, in this study the magnetic permeability, μ, is set to be that of free-space (non-magnetic material) but it may be

possible in future work to include variability in μ to map magnetic permeability variations in addition to resistance.

A method to estimate the subsurface resistance using the thin sheet approximation is not a new endeavor but estimating the resistance using equation (3-1) (or the simplified version, equation (3-2)) has not been done previously. This is likely due to the potentially problematic measurement of the vertical spatial derivative. Furthermore, unlike the approach presented here, other methods generally involve using some form of inversion which is considerably more difficult to solve (Keating and Crossley, 1990; Liu and Asten, 1993).

3.4 Forward Modeling

In the following section, we test the idea of using the equation which describes the electromagnetic induction in thin sheets with a constant resistance (equation (3-2)) on models with laterally varying resistance. The forward modeling was performed using Multiloop III (Walker and Lamontagne, 2006).

A simple non-uniform resistance case can be represented by a small circular feature in the center of a large sheet (pseudo-infinite). A two magnetic field sensor ground survey (to measure the vertical spatial derivative with a 2 m sensor separation) with a 30 Hz 100% duty periodic square wave transmitted waveform was simulated in Multiloop for the model shown in Figure 3-1. The time channels were measured over 10 windows spaced in a binary geometric progression (common ratio of 2, West et al., 1984). The data from this was used to solve for the resistance using equation (3-2) (simplified method) to produce Figures 3-2 and 3-3 (6 representative time windows shown). The survey was simulated inside of the transmitter loop (Tx loop, Figure 3-1)

as this was found to give the best results given that the vertical magnetic field is the largest in this layout (i.e. increases the likelihood that the ignored terms in equation (3-1) are small).

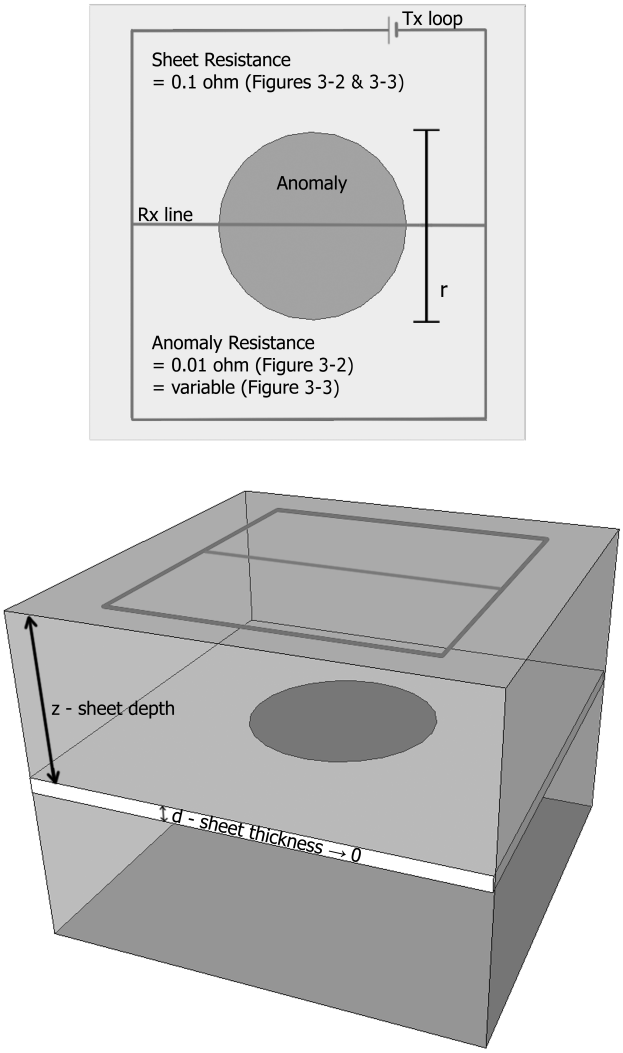

Figure 3-1: Plan view (top) and oblique view (bottom) of the generalized survey geometry and model used to produce the forward models in Figures 3-2 and 3-3 using Multiloop III. Tx and Rx stand for transmitter and receiver, respectively. The sheet is at a depth (z) of 30 m, the background sheet resistance is 0.1 ohm, the diameter of the anomaly (r) is 80 m and 180 m for Figures 3-2 and 3-3, respectively, and the dark grey circle represents the zone of anomalous resistance within the sheet. Model is not to scale.

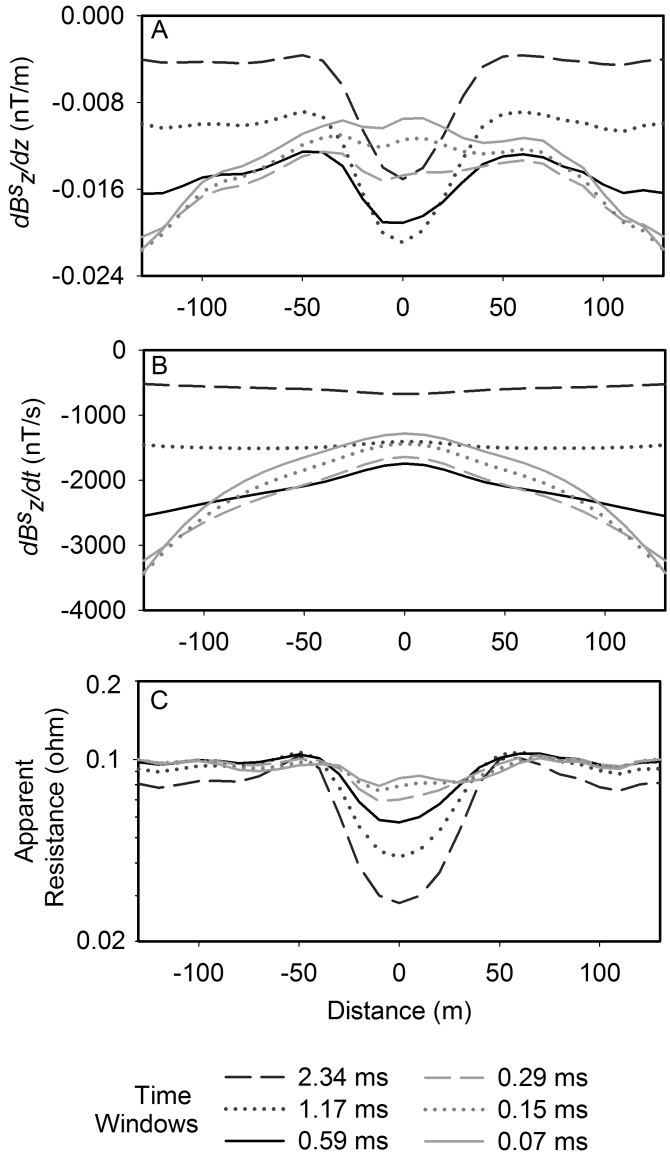

Figure 3-2: Forward model corresponding to a synthetic survey utilizing the survey geometry seen in Figure 3-1 (500 m by 500 m transmitter loop, background and anomaly resistance of 0.1 ohm and 0.01 ohm, respectively). Panel A is the vertical spatial derivative; panel B is the time derivative of the vertical magnetic field; and C is the apparent resistance calculated using equation (3-2). The different curves represent apparent resistance calculations using different sets of time channels. Note that the **B** rather than **H** magnetic fields are shown in this and subsequent figures because **B**-field units (nT) are more commonly used in practice ($\mathbf{B}=\mu\mathbf{H}$).

Since the modeled data provides the vertical magnetic field (H_z^s) averaged over several time intervals (windows or channels) at two heights, the vertical spatial derivative (dH_z^s/dz) was calculated by using the difference in the H_z^s field at these two heights (Figure 3-2A). Since dH_z^P/dt is equal to zero everywhere, apart from where the current changes polarity, the vertical component time derivative (dH_z/dt) was calculated by taking a forward difference between adjacent channels (Figure 3-2B). Since the time derivative was calculated by using two adjacent channels, the vertical derivative was averaged over the same two adjacent channels. If the time derivative (Figure 3-2B) is divided by the vertical derivative (Figure 3-2A) and multiplied by $\mu/2$, the apparent model resistance is calculated (Figure 3-2C). Since each time channel can be used in equation (3-2), multiple resistance profiles can be calculated, one for each set of adjacent time channels. Note the increased resolution to the anomalous zone with dH_z^s/dz and how the apparent resistance anomaly is more strongly a function of dH_z^s/dz than dH_z/dt. Although equation (3-2) is independent of the time channel used, each time channel produces slightly different apparent resistances. Despite this, the background resistance of the sheet and the dimension of the anomaly are estimated to be 0.1 ohm and about 80-100 m in diameter, respectively, which are consistent with the input values. The resistance of the anomaly was over-predicted at an approximate resistance of 0.08 (late time channels) to 0.03 (early time channels) ohm versus the input model resistance of 0.01 ohm.

The method can be further tested using a variety of resistance contrasts. Figure 3-3 utilizes the survey geometry seen in Figure 3-1 with a 400 m by 400 m transmitter loop, background resistance of 0.1 ohm and with a varying resistance for the circular anomaly (0.01 ohm, 0.05 ohm, 0.5 ohm and 1 ohm). Panels A, B and C show the estimated apparent resistance at early, intermediate and late time channels, respectively. For reference, a constant resistance model (i.e.

no anomaly) is also shown (solid line). The same pattern as in Figure 3-2 is seen. Note that in Figure 3-3C, the most conductive case (0.01 ohm) generates negative results in the late-time response (which cannot be shown in the log plot). This is a function of small dH_z^s/dz fields in the vicinity of a zero-crossover allowing for the small numerical noise to cause erratic apparent resistances. Forward modeling has revealed that while the calculated resistance of the anomaly is under-predicted for resistive anomalies or over-predicted for conductive anomalies (a common problem in estimating conductivity from EM data due to the lack of sensitivity of the EM response to changes in the resistivity of highly resistive and/or small features), it is in the correct sense (more or less resistive than background) and its spatial dimensions are well defined.

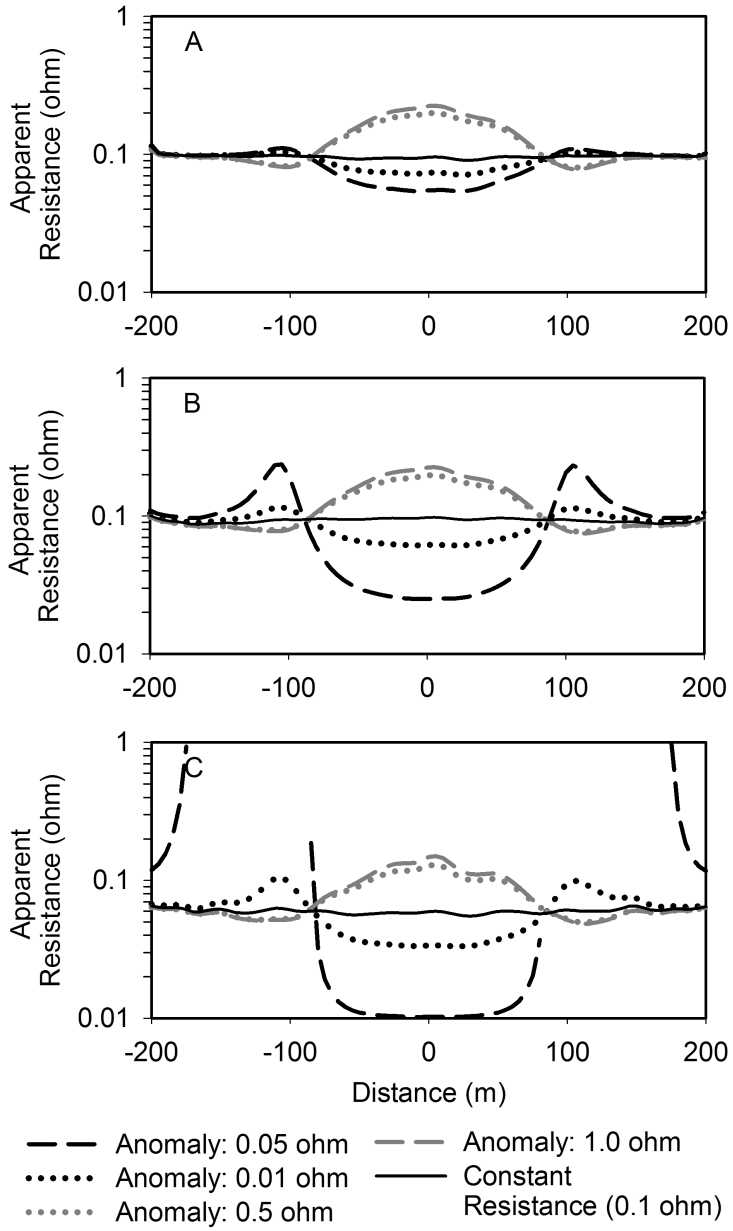

Figure 3-3: Apparent resistance calculated using equation (3-2) for synthetic models corresponding to surveys utilizing the survey geometry seen in Figure 3-1 (400 m by 400 m transmitter loop) at various resistance contrasts and various time channels. Panel A shows the early time; panel B the intermediate time and C the late time.

Two adverse side effects emerge from using an infinite sheet and uniform resistance assumption on models that are finite in size and/or laterally varying. They are the under-prediction or over-prediction of the input model resistance and the disagreement between the resistances calculated using each set of time channels (Figure 3-3). They arise from the fact that each time channel corresponds to a different sampled area (due to the nature of the diffusing currents); the later in time, the larger the diffused current system. As such, each time channel may invalidate the method's assumptions (infinite, inductively thin, and uniform resistance) differently. Changing the depth of the sheet will have a similar effect on the apparent resistance calculated as the established current systems will be different. The calculated resistance in Figures 3-2 and 3-3 are progressively smaller towards the later time channels because these channels are associated with currents that are impacted by the edge of the sheet. The difference is not as pronounced in more conductive models because the currents do not diffuse as quickly. It is important to use all of the available time channels as they may be sensitive to different areas within the sheet and by investigating the resistance calculated at each set of time channels, it may be possible to estimate the size of the sheet and/or the resistivity with depth.

3.5 Field Data

It should be possible to model a shallow and laterally extensive dry mine tailings pond situated on Vale property in Sudbury, Ontario, Canada, as an inductively thin sheet as its small thickness should satisfy the thin sheet approximation criteria. It is also suspected to contain a laterally varying resistance as is sometimes found in waste rock piles (Chouteau et al., 2006). The resistance variations may be due to changes in the thickness of the tailing based on the underlying topography of the ground (which was unknown) or due to conductivity variations as a

result of dumping of different material over the lifespan of the tailings pond. A Geonics EM34-3 (J.D. McNeil, 1980, Geonics Ltd. Tech., note TN-6) survey was first performed to obtain an independent data set to which the results from equation (3-2) could be compared. See Figure 3-4 for the station locations for the EM34-3 (open squares) and dH_z^s/dz TDEM (closed circles) surveys and the TDEM transmitter loop location (dashed line). The shape of the transmitter loop is largely a result of the ground conditions and the desire to minimize transmitter noise (signal leakage into the off-time) by placing the loop edges further from the survey lines.

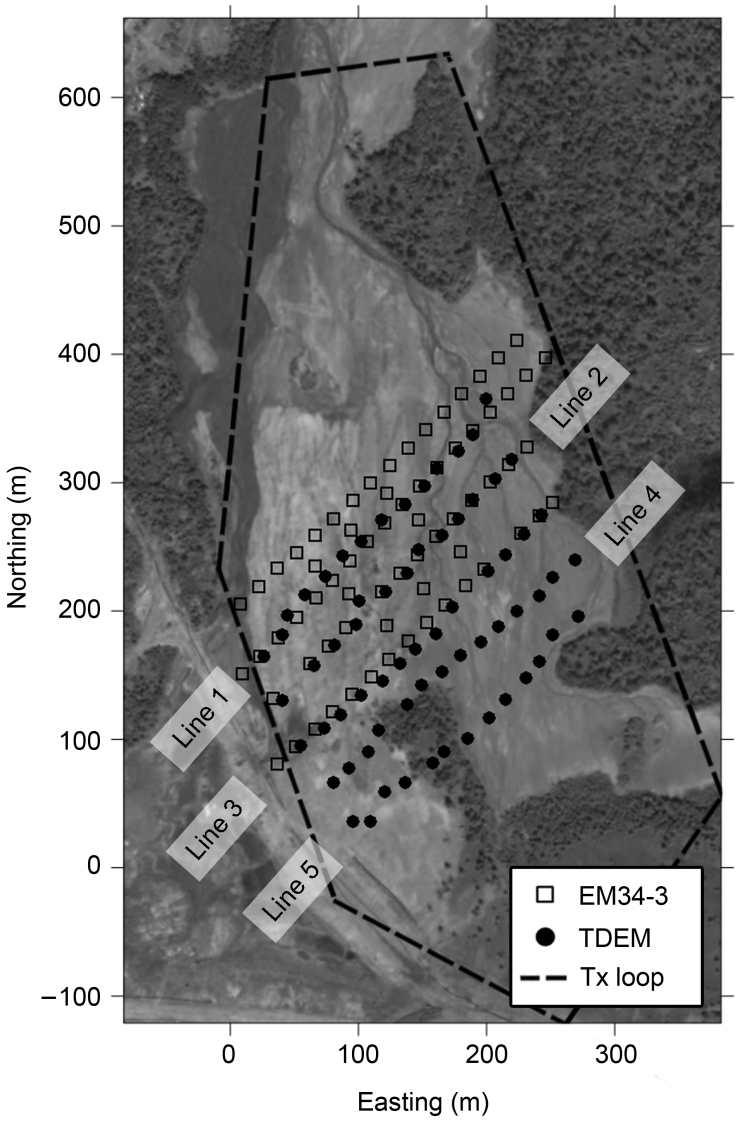

Figure 3-4: Station locations for the Geonics EM34-3 and vertical spatial derivative TDEM surveys superimposed atop an aerial image of the dry tailings pond on Vale property located in Sudbury, Ontario, Canada. The lines indicated (e.g. 'Line 1') are for the TDEM survey. Open squares are the locations for the EM34-3 survey, closed symbols are for the TDEM receiver locations, and the black dashed line represents the approximate location of the transmitter loop for the TDEM survey.

3.5.1 Geonics EM34-3

The EM34-3 survey was carried out over 4 lines spaced 40 m apart with stations every 20 m and an additional 3 stations spaced 40 m apart centered between each of the lines (Figure 3-4). The sensors were located directly on the ground and the transmitter-receiver offset was held at a constant 10 m and was operated in horizontal and vertical dipole mode to provide effective depths of exploration of 7.5 m and 15 m, respectively. A two layer model (tailing and basement) with a basement conductivity of 0 S/m was assumed (reasonable assumption for the area). This resulted in two equations (one for each dipole mode) with two unknowns (conductivity and thickness) using the formulae found in Geonics Limited Technical Note 6 (J.D. McNeil, 1980, Geonics Ltd. Tech., note TN-6). This system of equations was solved and the conductance of the tailings pond was calculated from the product of the conductivity and thickness (Figure 3-5). The high values of conductance to the northwest are likely to be the result of a large pipe or a road running from north to south along the western edge of the survey area. Therefore, the general observed pattern can be thought of as a conductive area in the center with a resistive area along the edges.

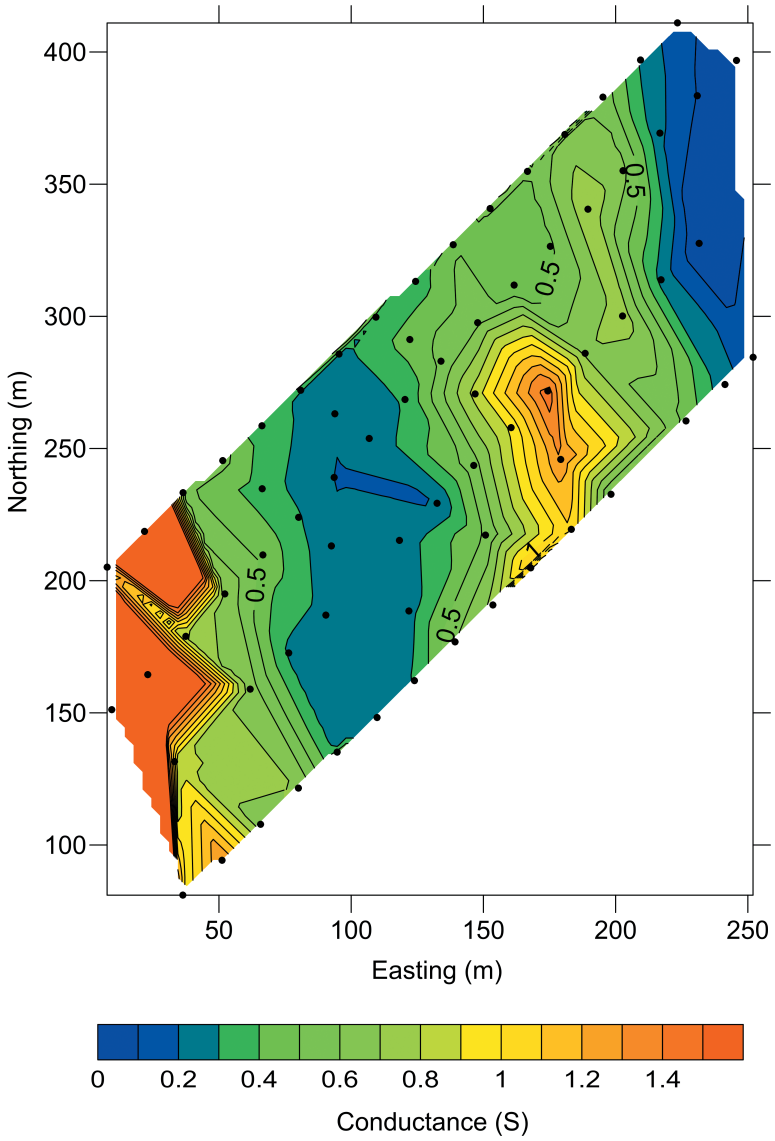

Figure 3-5: Contoured conductance over the dry tailings pond calculated by assuming a two layer case with the bottom layer having a conductivity of 0 S/m. Survey data was acquired using the Geonics EM34-3 at a transmitter-receiver separation of 10 m. Black dots represent station locations. Gridding on this and subsequent figures used triangulation with linear interpolation.

3.5.2 TDEM Survey

The TDEM survey was performed inside of a loop roughly 700 m by 350 m with a 30 Hz 50 % duty cycle exponential turn on linear ramp off waveform generated using a Geonics TEM-57 transmitter. The transmitter is not identical to the one tested in the forward modeling section but should produce the same results as in both cases dH_z^P/dt is equal to zero making equation (3-2) independent of the primary magnetic field. A SMARTem 24 receiver was used with Geonics 3D-3 sensor coils measuring the horizontal (x and y, inline and crossline, respectively) and vertical (z) components. Three 3D-3 coils were located on three different platforms spaced vertically apart by 1.1 m. In addition to the Geonics sensors, three vertical feedback coils (magnetometers) were also used, however their use is not relevant to this paper. The structure that held these sensors was composed entirely of PVC pipe and wood (Figure 3-6). In this experiment, the prototype structure was designed to be dragged along a clear opening atop snow but similar structures could be designed to meet specific requirements. The survey was performed over 5 lines spaced 40 m apart with stations every 20 m along the line. The southern 3 lines of the Geonics EM34-3 survey corresponded approximately to lines 1-3 in this survey (Figure 3-4).

Figure 3-6: Vertical spatial derivative measurement structure made of PVC pipe and wood housing three Geonics 3D-3 coils (x, y and z components) and 3 vertical B-field feedback sensors with each level separated by 1.1 m. The apparatus was dragged from station to station.

Each station measurement included five readings of about 30 seconds (756 waveform stacks) and the coil sensor output was proportional to the time derivative of the magnetic field (dB_x/dt, dB_y/dt, dB_z/dt). This was integrated to give the magnetic field (B_x, B_y, B_z) using the full waveform data (Smith and Annan, 2000). The data were then windowed and averaged (B_z and B_x at the base

level coil can be seen in Figure 3-7 and 3-8, respectively). The crossover in the B_z component and the peak in the B_x component (trending NW-SE) are suggested to be caused by the edge of the conductive portion of the tailings pond. Noise estimates, calculated by taking the standard deviation between 5 stacked and windowed waveforms, were found to range from approximately 0.01 pT/A to 0.1 pT/A (mean of 0.04 pT/A) for the vertical components. The vertical spatial derivative (dH_z^s/dz) was obtained by calculating the vertical derivative using the difference between the base and the average of the mid and upper sensors as this combination had the lowest noise (Figure 9). As would be expected by taking a spatial derivative, many of the subtle changes along the profiles in Figure 3-7 are more pronounced in Figure 3-9. For reference, a thick black line is used to indicate the noise levels averaged over the first 5 windows (mean of 0.03 pT/(Am)). The signal-to-noise (S/N) ratio (relative error, Figure 3-10) for window 1 (t = 192 μs) is, on average, well below 33 % (larger over lines 2 and 3 and where the signal is very low) which provides an adequate S/N on which equation (3-2) can be tested.

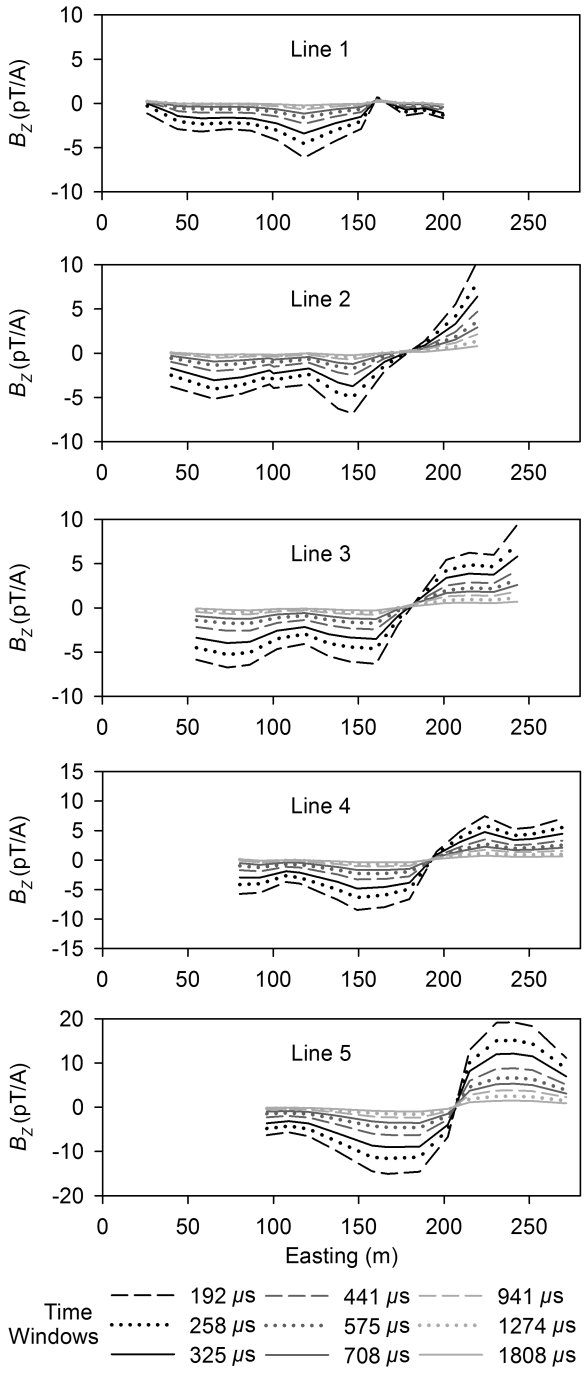

Figure 3-7: Off time, integrated, windowed and stacked B_z for the base level Geonics coil. The quantity measured is the magnetic field integrated from the measured voltage. Noise estimates were found to range from approximately 0.01 pT/A to 0.1 pT/A (mean of 0.04 pT/A for all 3 sensors).

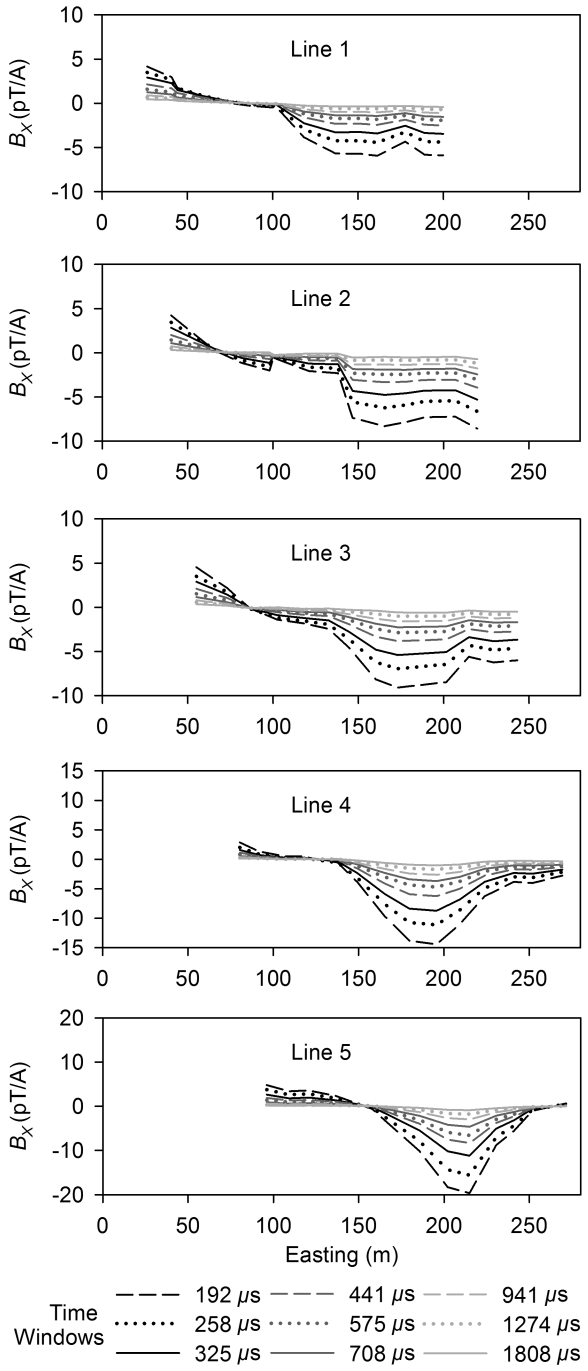

Figure 3-8: Off time, integrated, windowed and stacked B_x (inline) for the base level Geonics coil. The quantity measured is the magnetic field integrated from the measured voltage.

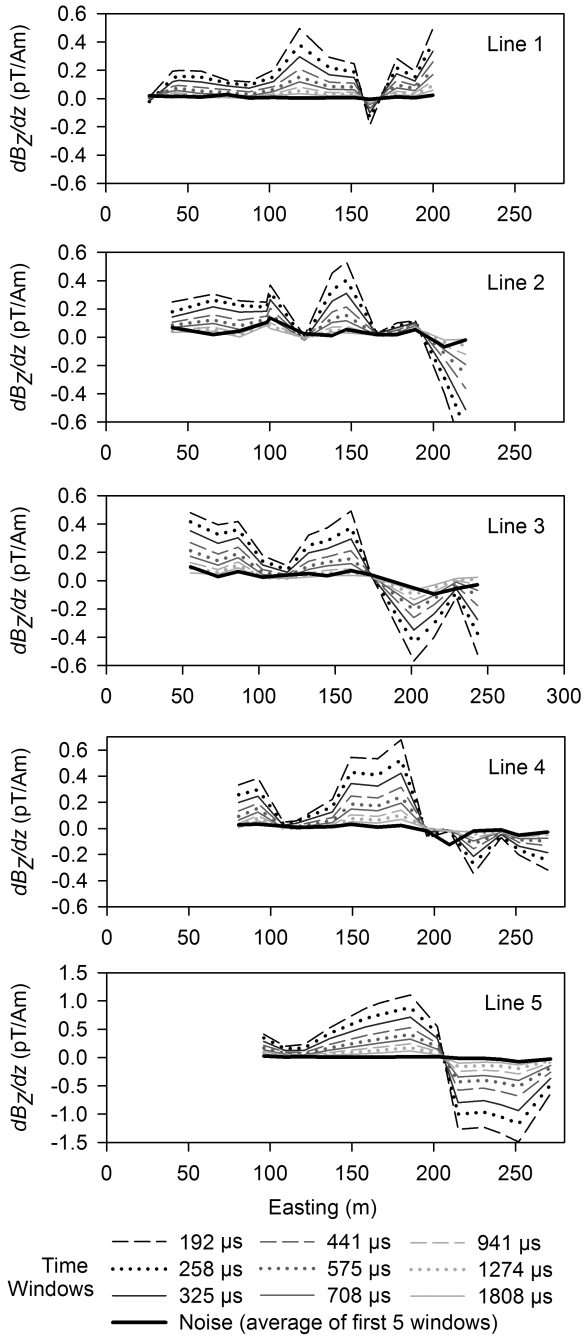

Figure 3-9: Off time, integrated, windowed and stacked vertical spatial derivative (dB_z/dz) calculated from the difference between the base and the average of the mid and upper sensors. The thick black line is used to indicate the noise levels averaged over the first 5 windows (mean of 0.03 pT/(Am)). The vertical spatial derivative is visibly above the noise levels for the early windows.

3.6 Apparent Conductance Results

Since equation (3-2) was developed to be used over a thin sheet model, any stations not located atop the sheet were removed since they violate the inherent assumptions (stations to the right of the crossover in B_z). Furthermore, all stations with a S/N ratio below 3 were also removed (Figure 10). The apparent resistance was calculated using equation (3-2) and the apparent conductance (inverse of apparent resistance) for early and intermediate time can be seen in Figure 3-11. The relative error in the apparent conductance (Figure 3-12) was on average less than 10% (larger over interpreted resistive zones and where dH_z^s/dz noise levels were increased).

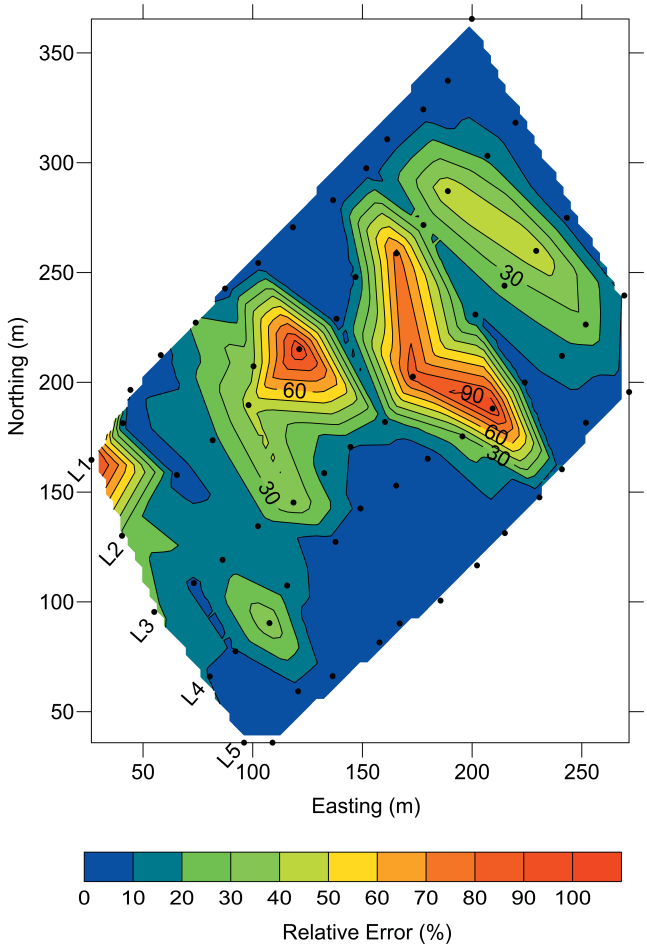

Figure 3-10: A signal-to-noise ratio map (relative error) calculated for window 1 (t = 192 μs) of Figure 3-9. Line numbers indicated and black dots represent station locations. Note that where the relative error exceeded 100 %, a value of 100 % was assigned to allow the full range of data to be seen.

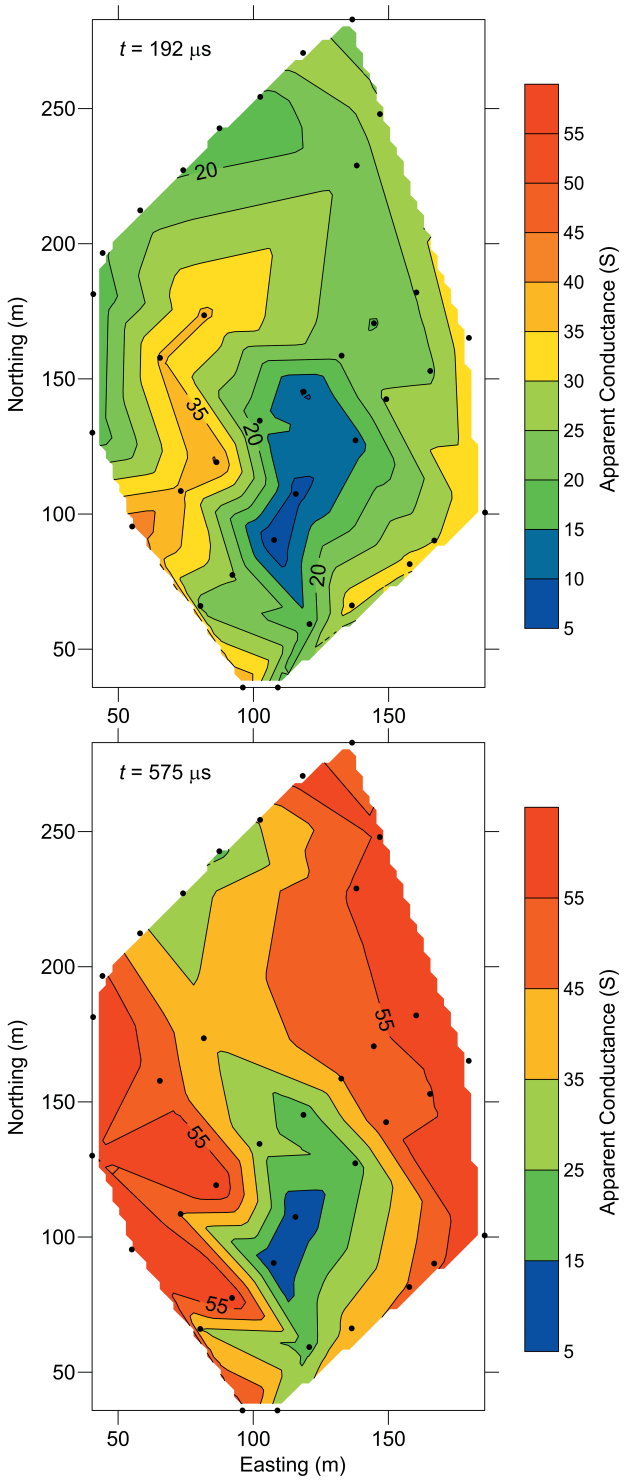

Figure 3-11: Apparent conductance over the tailings pond calculated using equation (3-2) for early time (top, window 1) and intermediate time (bottom, window 5). Black dots represent station locations.

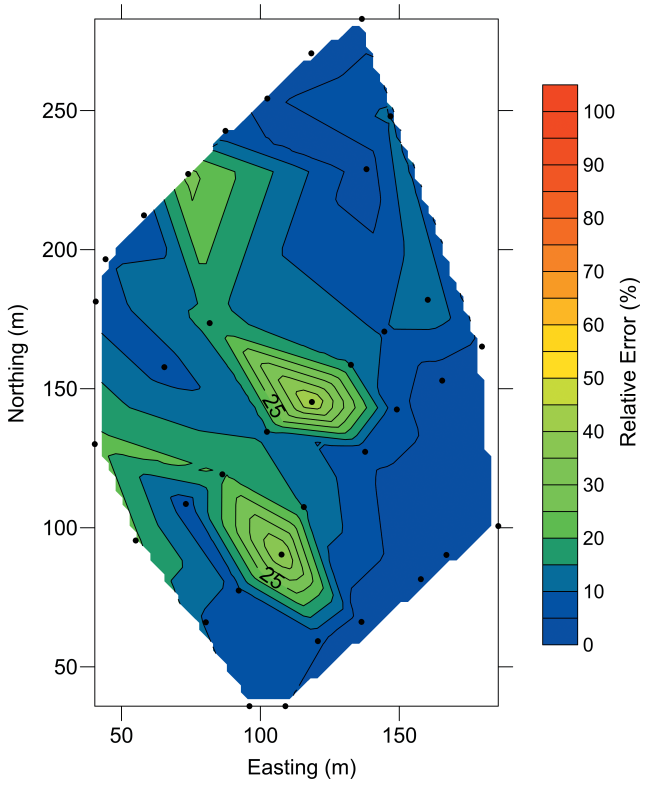

Figure 3-12: A relative error map calculated for the early-time window conductance calculation in Figure 3-11. The relative error is, on average, 10 %. Black dots represent station locations.

The general observed pattern in Figure 3-11 in the early time (t = 192 μs) is a SW-NE trending resistive zone to the south and a SW-NE trending conductive zone to the north. The intermediate time (t = 575 μs) results are roughly twice as conductive and are dominated by a S-N trending resistive zone. The increase in apparent conductance with time is also evident in the synthetic data and, as argued above, may be a result of the finite size of the tailings pond. Variations in apparent conductance (at each delay time) may be due to changes in the tailing thickness or due to conductivity variations from factors such as particle size variations, water content and/or the

presence of electrically conductive metals (Telford et al., 1990; Samouelian et al., 2005; Martinez-Pagan et al., 2009). As the resistive zone to the south roughly matches the location of a more vegetated area (Figure 3-4), there may be a link between the ability of the tailings to support vegetation and areas of low conductance (i.e. thinner waste or less conductive material). In contrast, the zones with a higher conductance may represent more conductive areas due to increased metal concentrations and/or thicker portions of tailings.

The similarity in the shape of the zones in the EM34-3 conductance and equation (3-2) conductance estimates (Figure 3-13) include an interpreted resistive zone running roughly through the middle of the area with more conductive zones on either side. The continuity of this resistive zone in the early time results may have been more intact and similar to that of the late time or EM34-3 estimate had the S/N ratio along the middle of line 2 been higher. The major difference between them is that the EM34-3 conductance estimates are significantly lower than that of what was calculated using equation (3-2). It is possible that this discrepancy is due to the two methods imaging different depths of the tailings pond. The EM34-3 had a depth of penetration of less than 20 m whereas the TDEM survey suggests a body which is much deeper based on the breadth of the anomalies (the peak-to-peak distance around the cross-over). As such, it is suggested that the EM34-3 survey imaged the near surface which appears to be more resistive and the developed methodology was more sensitive to a deeper and more conductive portion of the tailings pond. The apparent conductance estimates changing with delay time are also consistent with the hypothesis that the conductivity or conductance structure of the tailings changes with depth. Additionally, the EM34-3 conductance estimate was based on the assumption of a two layer model with the bottom layer having a conductivity of zero which may be untrue considering that the TDEM survey suggests a deeper conductor. Furthermore, the

EM34-3 apparent conductivity readings rely on a low-induction number assumption which breaks down as the conductivity is increased (J.D. McNeil, 1980, Geonics Ltd. Tech., note TN-6). For these reasons, equation (3-2) may be a more reliable and accurate mapping technique over the EM34-3. Another possible reason for the discrepancy is that our thin sheet assumption or assumption that the product of the spatial derivatives of resistance and the corresponding horizontal magnetic field is small may be incorrect. Mutual coupling effects between the sensors were also assumed to be negligible, and if present, may have introduced some error into the apparent conductance estimation.

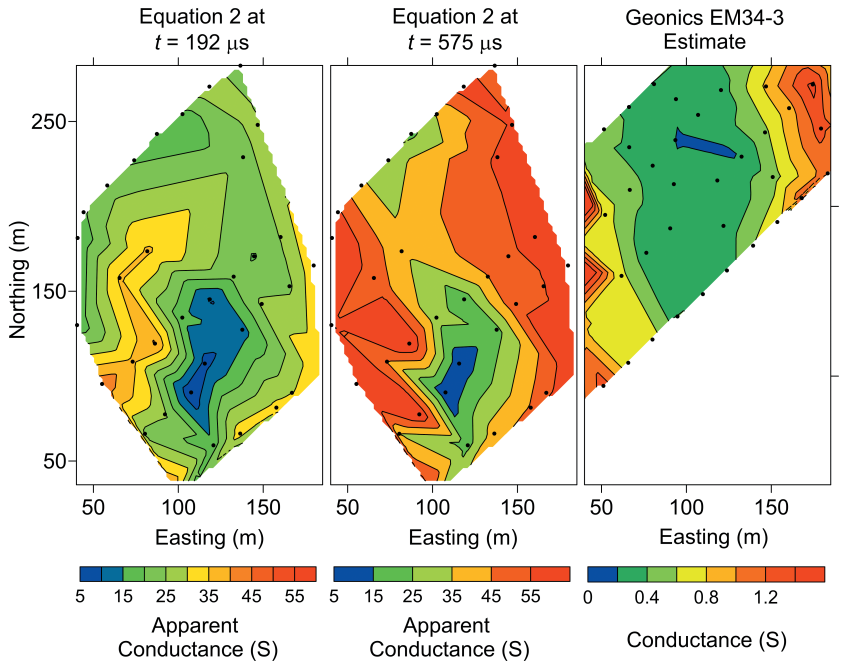

Figure 3-13: Comparison of Figure 3-11 (apparent conductance estimate using the developed method, equation (3-2)) and Figure 3-5 (conductance estimate using the Geonics EM34-3 system) scaled to the same map limits. Black dots represent station locations. A resistive zone runs through the middle of each conductance estimate.

3.7 Conclusion and Future Work

The differential equation which describes induction in a thin sheet with laterally varying resistance can be simplified to require only two measurable quantities: dH_z^s/dz, and dH_z/dt. Through forward modeling, we showed that the simplified differential equation can accurately determine an apparent resistance at specific locations above thin sheet models where the resistance is not uniform. Mapping conductance as a function of lateral position in a thin sheet model is an important step towards assessing if there is significant remaining metal content in mine waste. In real field data, collected over the top of a dry tailings pond, dH_z^s/dz is small, but above the noise levels. Apparent conductance estimates using the developed methodology revealed that the dry tailings pond has zones of varying conductance and a large resistive zone associated with surface vegetation. Further work would be required to determine whether zones where the conductance is low is correlated with thinner and/or less conductive tailing material and whether zones of greater conductance (areas where there is no vegetation) are related to zones of increased metal (or even clay) concentrations and/or thicker tailings. The geophysical data can be used to guide a sampling program that would answer these ambiguities.

Even though this field example was on a dry tailings pond, the methodology is general and could be used to estimate an apparent conductance over any thin sheet like body such as for estimating overburden conductance and for nickel laterite exploration and characterization. Hence, we believe that mapping a laterally varying conductance using the derived equation can be practically performed and of benefit.

Future work involves developing a way to transform the conductance data into conductivity versus depth, forward modeling of the response over the dry tailings pond and developing,

testing and comparing the full equation (i.e. addition of the terms involving the product of the resistance derivatives with the horizontal magnetic fields) with the simplified approach presented here.

3.8 References

Akcil, A., and S. Koldas, 2006, Acid Mine Drainage (AMD): causes, treatment and case studies: Journal of Cleaner Production, **14**, 1139-1145.

Anterrieu, O., M. Chouteau and M. Aubertin, 2010, Geophysical characterization of the large-scale composition of a waste rock pile from a hard rock mine: Bulletin of Geological Engineering and the Environment, **69**, 533-548.

Aplin, C. L., and G. O. Argall, 1973, Tailings disposal today: Proceedings of the 1st international tailing symposium. Miller Freeman Publications, Inc., San Francisco, California.

Bartel, C. L., H. D. Cress, and G. L. Stolarczyk, 1997, Evaluation of the electromagnetic gradiometer concept for detection of underground structures—theory and application: Journal of Environmental and Engineering Geophysics, **2**, no. 2, 127-136.

Brown, D. G., K. J. DeVos, G. Hall, and B. Macnamara, 1999, Characterization of slag produced at the Falconbridge Limited smelter site: Proceedings of Sudbury ’99 Mining and the Environment II, **2**, 755-764.

Chouteau, M., O. Anterrieu, M. Aubertin, C. Dubreuil-Boisclair, and J. Poisson, 2006, Geophysical characterization of an AMD-generating waste rock pile using ground and borehole techniques: SAGEEP Proceedings 2006, 128-139.

Frischknecht, F. C., V. F. Labson, B. R. Spies, and W. L. Anderson, 1991, Profiling methods using small sources, *in* M. N. Nabighian, eds., Electromagnetic methods in applied geophysics, *Applications, Part A and B: SEG, Investigations in Geophysics No. 3, Volume **2**, 105–270.*

Grant, F. S., and G. F. West, 1965, Interpretation theory in applied geophysics. McGraw-Hill.

Irvine, R. J., and G. Staltari, 1984, Case history illustrating problems in transient electromagnetic surveys: Exploration Geophysics, **15**, 155-167.

Jones, A. G., 1983, A passive natural-source twin-purpose borehole technique: vertical gradient magnetometry (VGM): Journal of Geomagnetism and Geoelectricity, **35**, 473-490.

Joshi, M. S., O. P. Gupta, and J. G. Negi, 1988, On the effects of thickness of the half-plane model in HLEM induction prospecting over sulphide dykes in a highly resistive medium: Geophysics Prospecting, **36**, 551-558.

Keating, P. B., and D. J. Crossley, 1990, The inversion of time-domain airborne electromagnetic data using the plate model: Geophysics, 55, 705-711.

Lacob, C., and R. Orza, 2008, Integrated interpretation of geophysical data on metalliferous mining waste deposits: Near Surface 2008 – 14th European meeting of environmental and engineering geophysics, B02, 5 pp.

Liu, G., and M. Asten, 1993, Conductance–depth imaging of airborne TEM data: Exploration Geophysics, **24**, 655– 662.

Macnae, J. C., and Y. Lamontagne, 1987, Imaging quasi-layered conductive structures by simple processing of transient electromagnetic data: Geophysics, **52**, 545–554.

Marcuson, W. S., and C. M. Diaz, 2007, The changing Canadian nickel smelting landscape – late 19th century to early 21st century: Canadian Metallurgical Quarterly, **46**, 33-46.

Martinez-Pagan, P., A. Faz Cano, E. Aracil, and M. A. Arocena, 2009, Electrical resistivity imaging revealed the spatial properties of mine tailing ponds in the Sierra Minera of southeast Spain: Journal of Environmental & Engineering Geophysics, 14, 63-76.

McKenna, S. P., B. S. Parkman, J. L. Perren, and R. J. McKenna, 2011, Response of an Electromagnetic Gradiometer to a Subsurface Wire: IEEE Transactions on Geoscience and Remote Sensing, 49, 4944-4953.

Nabighian, M. N., and J. C. Macnae, 1991, Time domain electromagnetic prospecting methods, *in* M. N. Nabighian, eds., Electromagnetic methods in applied geophysics, *Applications, Part A and B: SEG, Investigations in Geophysics No. 3, Volume **2**, 427–520.*

Patella, D., and A. Siniscalchi, 1994, Two-level magnetovariational measurements for the determination of underground resistivity distributions: Geophysical Prospecting, **42**, 417- 444.

Peric, M., 1981, Exploration of Burundi nickeliferous laterites by electrical Methods: Geophysical Prospecting, **29**, 274-287.

Price, A. T., *1949, The induction of electric currents in* non uniform thin sheets and shells: Quarterly Journal of Mechanics and Applied Mathematics, **2**, 283-310.

Rutherford, J., T. Munday, J. Meyers, and M. Cooper, 2001, Relationship between regolith materials, petrophysical properties, hydrologeology and mineralisation at the Cawse Ni laterite

deposits, Western Australia: Implications for exploring with airborne EM: Exploration Geophysics, **32**, 160-170.

Samouelian, A., I. Cousin, A. Tabbagh, A. Bruand, and G. Richard, 2005, Electrical resistivity survey in soil science: a review: Soil & Tillage Research, **83**, 173–193.

Sattel, D., and J. C. Macnae, 2001, The feasibility of electromagnetic gradiometer measurements: Geophysical Prospecting, **49**, 309–320.

Smith, R. S., 2000, The realizable resistive limit: A new concept for mapping geological features spanning a broad range of conductances: Geophysics, **65**, 1124–1127.

Smith, R. S. and A. P Annan, 2000, Using an induction coil sensor to indirectly measure the B-field response in the bandwidth of the transient electromagnetic method: Geophysics, **65**, 1489-1494.

Smith, R. S., and G. F. West, 1987, Electromagnetic induction in an inhomogeneous conductive thin sheet: Geophysics, **52**, 1677-1688.

Swidinsky, A., and R. N. Edwards, 2009, The transient electromagnetic response of a resistive sheet: straightforward but not trivial: Geophysical Journal International, **179**, 1488–1498.

Telford, W. M., L. P. Geldart, and R. E. Sheriff, 1990, Applied geophysics: Cambridge University Press.

Vozoff, K., 1991, The magnetotelluric method, *in* M. N. Nabighian, eds., Electromagnetic methods in applied geophysics, Applications, Part A and B: SEG, Investigations in Geophysics No. 3, Volume **2**, 427–520.

Walker, P., and Y. Lamontagne, 2006, Electromagnetic interpretation in complex geological environments: SEG Technical Program Expanded Abstracts 2006, 1288-1292.

West, G. F., J. C. Macnae, and Y. Lamontagne, 1984, A time-domain EM system measuring the step response of the ground: Geophysics, **49**, 1010–1026.

Xie, Y., Y. Xu, L. Yan, and R. Yang, 2005, Recovery of nickel, copper and cobalt from low-grade Ni-Cu sulfide tailings: Hydrometallurgy, **80**, 54-58.

Chapter 4

4 Mapping lateral changes in conductance of a thin sheet using time domain inductive electromagnetic data

4.1 Abstract

With the inductive electromagnetic geophysical method, the laterally varying conductance of thin sheet conductors can be estimated either through a direct transform of the measured data or through inversion. The direct transform (termed the 'simplified solution') does not require grid or line data and is simple enough to be performed in the field in real-time as the conductance at a location is calculated directly from the ratio of two measured magnetic fields (the vertical spatial and temporal derivative of the vertical magnetic field) at that location. However, the simplified solution assumes that the secondary horizontal magnetic fields are zero and/or that the sheet has a uniform conductance. Our non-approximate solution (termed the 'full inversion') does not make these assumptions, but requires gridded data, measurements of the secondary horizontal magnetic fields and more complicated inversion algorithms. Through forward modeling we show that the full inversion provides better results than the simplified solution when the spatial gradient of the resistance is strong and/or when the horizontal magnetic fields are large. Since the simplified solution may be preferable due to its simplicity, we introduce two unreliability parameters, which assess the unreliability of the conductance calculated using the simplified solution. A comparison of the simplified solution and full inversion in a fixed in-loop survey collected overtop a dry tailings pond in Sudbury, Ontario, Canada revealed that there were small

differences around large conductance contrasts which coincided with elevated unreliability parameters. The simplified solution is recommended if fast in-field interpretations are required, or additionally, as a first-pass survey which can be performed with sparse station spacing in order to identify areas of interest. Denser grid data can then be collected, for the more reliable full inversion, over areas of interest and/or zones where the simplified solution is expected to be unreliable as predicted by the unreliability parameters.

4.2 Introduction

The primary goal of most electromagnetic (EM) geophysical surveys is to determine the distribution of electrical properties, namely conductivity, below the surface which accurately explains the measured electromagnetic response (generally the magnetic field or its time derivative). This is often accomplished through the use of stitched one-dimensional (1D) conductivity-depth sections (either through 1D inversions and/or conductivity depth imaging/transforms; Macnae, 2007) and/or trial-and-error forward modeling whereby the interpreter adjusts synthetic models until the generated synthetic data resembles the field data (Hohmann and Raiche, 1987). Three-dimensional (3D) inversions such as those proposed by Haber et al. (2002) and/or Zhdanov (2010) are appealing because they more accurately describe the earth geometry and the physics in more complex situations. However, these full 3D inversions have been hampered by the size, ill-posedness and complexity of the problem, and as such, the faster and simpler 1D algorithms are generally used (Macnae, 2007). In parallel, the thin sheet approximation, which assumes that current is constrained to flow in a sheet that is inductively thin (Price, 1949), has been used extensively to simplify the equations used to solve for the electromagnetic fields in 3D media and has been effective in forward modeling and

inversion routines (West et al., 1984; Macnae and Lamontagne, 1987; Keating and Crossley 1990; Nabighian and Macnae, 1991; Liu and Asten, 1993; Smith, 2000; Tartaras et al., 2000; Swidinsky and Edwards, 2009; Kolaj and Smith, 2013). The success of the thin sheet assumption is due to many factors, namely the magnetic fields from a thin sheet are easy to visualize; many mineral exploration targets can be represented as thin sheets (Grant and West, 1965; Palacky 1987); sedimentary layers can, as a first approximation, be thought of as stacked thin sheets (Tartaras et al., 2000; Walker and Lamontagne, 2007) and thin sheets are described by a conductance (product of conductivity and thickness) which is, at times, more robust than the corresponding conductivity and thickness (Liu and Asten, 1993). The thin sheet approximation is relatively robust and generally valid as long as the thickness of the sheet is smaller than the skin depth or diffusion depth in the frequency and time domain, respectively (Joshi et al., 1988; Frischknecht et al., 1991). As such, while solving the full 3D inversion is sometimes preferred in terms of its accuracy, an inversion scheme based on thin sheets is an attractive shortcut in circumstances where the geology is consistent with the inherent assumptions.

A simple yet robust method for mapping a laterally varying conductance over extensive thin sheets from time-domain EM (TDEM) data was developed in Kolaj and Smith (2013) and tested in a field trial over a dry mine tailings pond. Such an algorithm is useful and is a geologically reasonable approximation in many areas such as in nickel laterite exploration where the nickel content is at times associated with areas of high conductance in the variable saprolite (Peric, 1981; Rutherford et al., 2001); in the characterization of mine, mill or smelter waste (Chouteau et al., 2006; Kolaj and Smith, 2013) and/or in the characterization or exploration over variable overburden (Seigel and Pitcher, 1978; Irvine and Staltari, 1984). The method of Kolaj and Smith (2013) involved a simplification of the electromagnetic (EM) induction formula for thin sheets

derived by Price (1949) and generalized for EM prospecting methods by Smith and West (1987). The simplification assumed a uniform resistance (inverse of conductance) and calculated an apparent resistance in sheets where the resistance varied laterally. This assumption relied on the product of the horizontal magnetic fields with the corresponding derivatives of the lateral resistance (i.e. $H_y^s dR/dy$ and $H_x^s dR/dx$) being negligible in comparison to the other two terms in the original equation (RdH_z^s/dz, and dH_z/dt). The advantages of the simplified over the non-simplified method are 1) the horizontal magnetic fields (H_y^s and H_x^s) are not required; 2) the resistance calculated at each station is independent of any other station and thus line/grid data is not required; and 3) the resistance calculation is simple enough to be performed in the field in real time. However, the benefits of the simplified method are limited by the approximations made and thus a detailed study of when the simplified, or non-simplified, solutions should be used is warranted.

We begin by briefly summarizing the solution to the problem of electromagnetic induction in thin sheets with a laterally varying conductance and how the equation may be inverted to estimate an apparent resistance (henceforth termed the "simplified solution") or the actual resistance (henceforth termed the "full inversion"). Through forward modeling, we explore the general characteristics of each method, the limitations of the simplified solution and we present a simple calculation which can determine whether the resistance calculated with the simplified solution will be valid. Lastly, we use our developed full inversion and compare it to the simplified solution on the field data collected in Kolaj and Smith (2013) overtop a dry mine tailings pond situated on Vale property in Sudbury, Ontario, Canada.

4.3 Theory

In Kolaj and Smith (2013), a simple method to estimate the apparent resistance of an inductively horizontal thin sheet embedded in a resistive medium, was derived based on the work of Price (1949) and Smith and West (1987). The formula for the apparent resistance, R, is

$$R = \frac{\mu}{2}\left(\frac{\frac{dH_z}{dt}}{\frac{dH_z^s}{dz}}\right), \tag{4-1}$$

where μ is the magnetic permeability (assumed to be that of free space), dH_z/dt and dH_z^s/dz are the time derivative of the vertical total magnetic field (secondary plus primary magnetic field) and the vertical spatial derivative of the vertical secondary magnetic field, respectively. This apparent resistance estimate assumed that there was no change in resistance in the lateral directions (i.e. $dR/dy \approx 0$ and $dR/dx \approx 0$) which allowed simplification of the full thin sheet induction boundary equation,

$$-\frac{dH_z^s}{dz}R + \frac{dR}{dy}H_y^s + \frac{dR}{dx}H_x^s = -\frac{\mu}{2}\frac{dH_z}{dt}. \tag{4-2}$$

In the off-time or when the primary magnetic field is a constant value, all terms in equation (4-1) and (4-2) are secondary magnetic fields ($\mathbf{H}^S$), and the calculated resistance becomes independent of the transmitter location and waveform (Kolaj and Smith, 2013). However, when dealing with finite sized and non-uniform conducting thin sheets, certain transmitter and receiver configurations will provide better results. For instance, the simplified solution (equation (4-1)) will work best when $H_y^s dR/dy$ and $H_x^s dR/dx$ are small in comparison to dH_z/dt and dH_z^s/dz which is achievable when the magnetic fields are measured inside of the transmitter loop where the

vertical magnetic fields dominate (Kolaj and Smith, 2013). Moreover, equations (4-1) and (4-2) are true at all delay times, so multiple resistance profiles, one for each time channel, can be calculated. The results from each time channel should be comparable unless the inductively thin sheet assumptions (and uniform resistance for equation (4-1)) are invalid or the signal-to-noise ratio in the measured fields is low. The results from each time channel can also differ if there are changes in resistivity with depth. While the simplified solution (equation (4-1)) is valid away from the sheet, equation (4-2) is valid only in the plane bounded by the sheet (i.e. immediately above or below the conductive thin sheet). However, the magnetic fields can be calculated away from the sheet by upward continuing the fields calculated at the surface of the sheet using equation (4-2) (i.e. the forward model of Smith and West, 1987). Thus, using equation (4-2) to calculate the resistance using magnetic fields measured above the sheet (i.e. the inverse problem) should provide a smoothed approximate estimate of the true resistance. As such, for near-surface applications, no knowledge of the sheet depth is required in order to solve the simplified solution for the apparent resistance (equation (4-1)) or to get an approximate resistance that satisfies equation (4-2). Furthermore, the methods will be limited to near-surface applications (where equation (4-2) is valid) as spatial derivatives (i.e. dH_z^s/dz) from deeper sources will likely be below background noise levels (Sattel and Macnae, 2001). While equation (4-1) (simplified solution) was used quite successfully in Kolaj and Smith (2013), the incorporation of the terms involving resistance derivatives (equation (4-2)) should provide a better estimate of the true resistance where these terms cannot be neglected.

4.4 Inversion Scheme

Equation (4-2) can be reformulated into a linear problem of the form

$$\mathbf{Ar} = \mathbf{b}\,, \tag{4-3}$$

where **r** is the vector of resistances (R) at different locations on the sheet, **A** is a matrix corresponding to the left-hand-side of equation (4-2) with finite difference operators used to estimate the lateral resistance derivatives, and **b** is the vector of elements corresponding to the right-hand side of equation (4-2). The matrix **A** is sparse and can be inverted allowing for equation (4-3) to be solved, but, like many other geophysical problems, it is often ill conditioned and benefits from regularization. Thus the inversion is performed by minimizing $f(\mathbf{R})$ in the over-determined system

$$f(\mathbf{R}) = \|\mathbf{W}(\mathbf{Ar} - \mathbf{b})\|^2 + \alpha^2\|\mathbf{Sr}\|^2\,, \tag{4-4}$$

where ||**…**|| represents the Euclidean norm, **W** is a weighting matrix corresponding to the inverse of the data error (assumed to be Gaussian distributed), **S** is a smoothing regularization matrix and α is the regularization coefficient which controls the relative contribution between term 1 (misfit) and term 2 (smoothness) in equation (4-4) (a high value of α would produce a smoother model). Equation (4-4) is solved in Matlab using orthogonal-triangular decomposition and 1600 station resistances can be calculated in a few seconds on a desktop computer (computation times in the examples presented in this work did not exceed 1 second). As the solution to equation (4-4) can be found quite rapidly, it can be re-run for many different values of α. The optimum α is found using a combination of an L-curve analysis (Zhdanov, 2002) and a qualitative analysis of the solutions obtained. Note that equation (4-1) can be similarly reformulated into the form of equation (4-4) in order to benefit from the error weighting and regularization. In this case, the **A** matrix becomes a diagonal matrix. However, by reformulating the problem in this manner, the

simplified solution would lose some of its advantages, namely, the independence of the calculated resistance from station to station, not requiring grid/line data and being able to calculate the resistance by taking a simple ratio of the measured fields.

The resistance derivatives (equation (4-2)) are represented using a finite difference approximation. Forward or backward differences are used along the edge of the grid while a central difference is used within the grid. When there is a large range of values in the measured fields and derivatives and/or high noise in the data, erratic/erroneous resistances are sometimes calculated along the edge of the grid which may propagate towards the center of the grid through the derivatives. An increase in the regularization coefficient tends to reduce this effect but may cause an overly smooth solution to be calculated. An alternative means of dealing with this issue is to estimate the measured fields, derivatives and the resistances beyond the survey area (we call this "data padding"). Data padding tends to move any potentially erratic resistances to be calculated in the padded zone which is subsequently removed and thus, it is not interpreted. The simplest and most effective method was to duplicate the measured components (dH_z^s/dz, H_y^s, H_x^s and dH_z/dt) along the outer edge of the grid outwards into the padded area. With the simplified solution, this would create a constant resistance envelope around the survey area.

4.5 Synthetic examples

In the following section, we discuss the accuracy and reliability of the estimates of resistance from the simplified solution (equation (4-1) and (4-4)) and full inversion (equation (4-2) and (4-4)) for three synthetic cases. As suggested in Kolaj and Smith (2013), the simplified solution is most effective when the survey is performed inside of the loop as in this configuration the vertical magnetic fields will be large relative to the horizontal magnetic fields (i.e. the ignored

terms, $H_y^s dR/dy$ and $H_x^s dR/dx$, will be minimized). As such, the first example involves this configuration while the second and third examples involve loop positions outside of the survey area where the simplified solution may fail as the size of the ignored terms will be larger. In each example a 30 Hz, two coil ground UTEM survey (with one receiver coil at 0 m and the second directly above at 2 m) with 27 lines and 27 stations per line (260 m line length, 10 m spacing between lines) was simulated in Multiloop III (Lamontagne Geophysics; Walker and Lamontagne, 2006). See Figure 4-1 for a schematic of the transmitter-loop locations and the thin sheet models used. Depths ranging from 20 m to 40 m were used for the synthetic models as these near-surface sheets would be the typical target depths/thicknesses for this method (i.e. overburden, mine waste, near surface deposits). The vertical spatial derivative (dH_z^s/dz) and the vertical-component time derivative (dH_z/dt) were calculated using finite difference operators. The identity matrix was used for the error matrix and there was no noise added to the data (apart from some numerical noise present in the forward model).

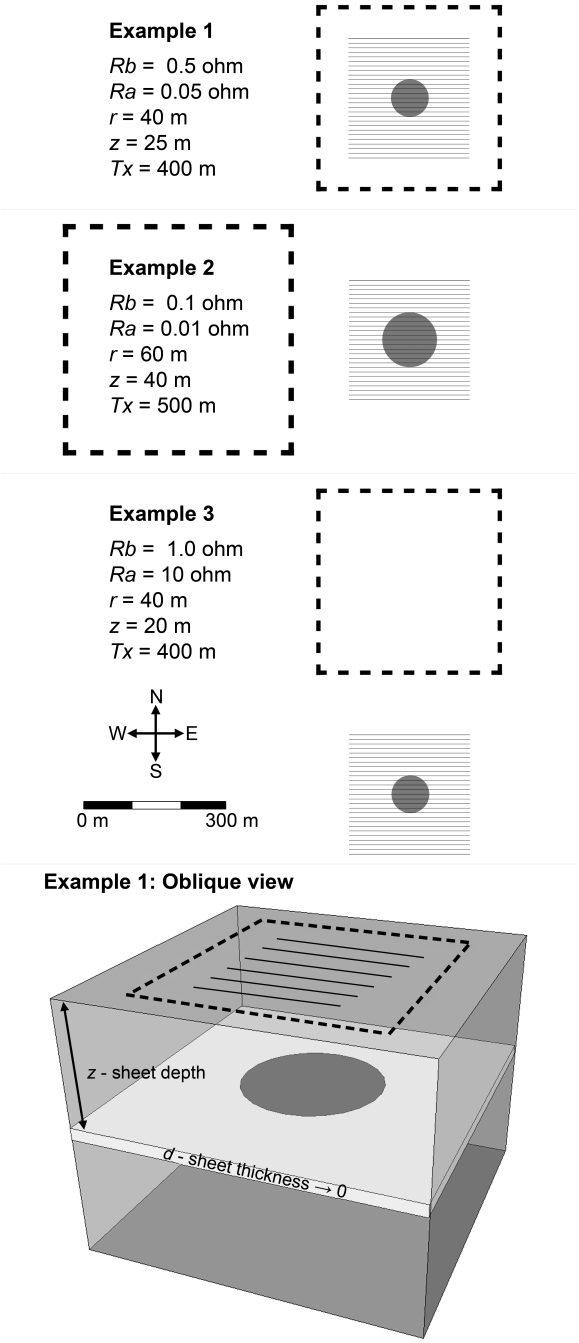

Figure 4-1: Plan view of the survey geometry used for the three synthetic examples (top, drawn to scale) used in Multiloop III and, for reference, an oblique view for example 1 (bottom, not drawn to scale, modified from Kolaj and Smith, 2013). *Tx* represents the dimensions of the square transmitter loop size and the dark grey circle (of radius, *r*) represents the zone of anomalous resistance (*Ra*) within the sheet of background resistance (*Rb*) at a depth of *z*.

4.5.1 Example 1

In the first example, a 400 m by 400 m loop is positioned around the survey area, the sheet is at a depth of 25 m and the background sheet and anomaly (r = 40 m) are 0.5 ohm and 0.05 ohm, respectively (Figure 1). The resistance results for the simplified solution and the full inversion (computed in less than a second on a laptop) gridded along the 27 lines can be seen in Figure 4-2. The regularization coefficient, α, was set to zero (i.e. the simplified solution is calculated directly for each station using equation (4-1)) and no data padding was required.

At early time in particular, the background resistance of the sheet from both the simplified solution and full inversion is estimated to be 0.5 ohm which is consistent with the input value. The background resistance is under predicted with increasing delay time with both methods (i.e. the background resistance in the later time channel is closer to 0.4 ohm than the true value of 0.5 ohm) and it was hypothesized in Kolaj and Smith (2013) that it is due to the fields at later delay time being impacted by the finite size of the sheet used in Multiloop III. The dimensions of the anomaly are not as easy to estimate as it depends on which method and time channel are used. The simplified solution appears to produce sharper anomalies but this is slightly deceiving as outside the anomalous area, the resistance overshoots the conductive anomaly (Figure 4-2). If the anomaly had been resistive, there would have been an undershoot (not shown). This overshoot and undershoot is most evident at late delay times. On the other hand, the full inversion provides smooth changes in the correct sense (i.e. broader anomalies with no over/under predictions). Nevertheless, the anomaly size can be estimated to be roughly 80 to 120 m in diameter which is consistent with the synthetic model. The resistance of the anomaly is generally under predicted (unless its dimensions are large) and in Figure 4-2, it can be estimated to be somewhere between 0.1 ohm to 0.3 ohm, with the late-time estimates being closer to the true value.

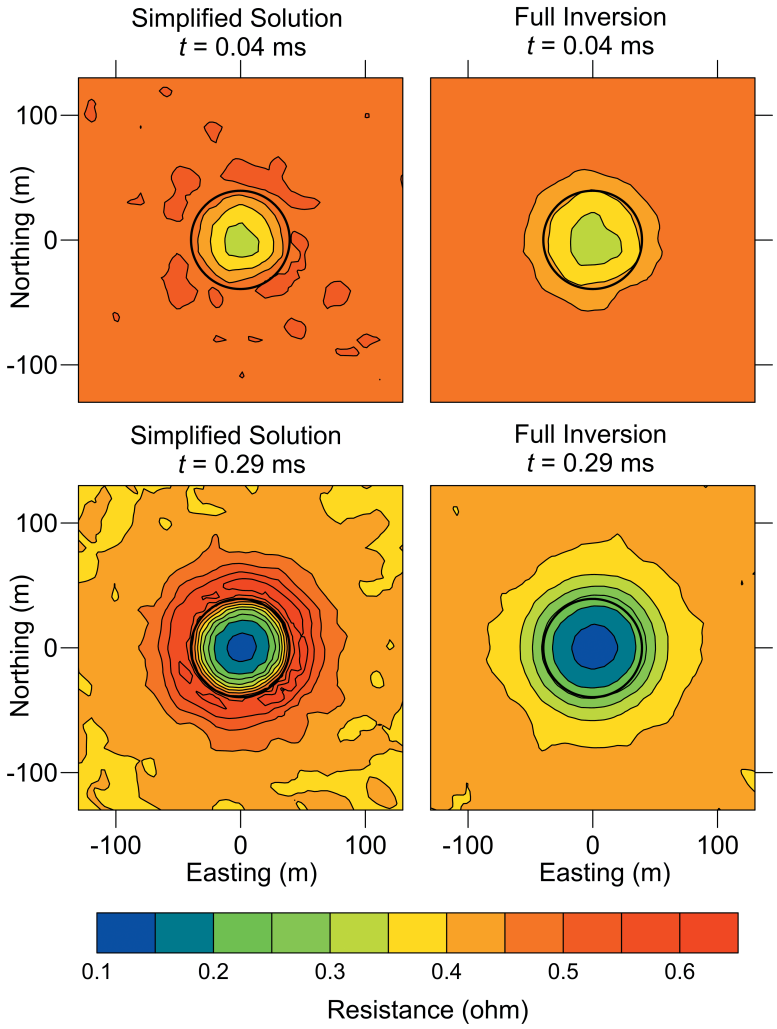

Figure 4-2: Resistance calculated using the simplified solution (equation (4-1), left panels) and the full inversion (equation (4-2) and (4-4), right panels), at t = 0.04 ms (top panels) and t = 0.29 ms (bottom panels) for synthetic example 1 (Figure 4-1). Resistances of the background sheet and anomaly (r = 40 m, black circle) are 0.5 ohm and 0.05 ohm, respectively. Gridding on this and subsequent figures uses triangulation with linear interpolation.

4.5.2 Example 2

In the second example, a 500 m by 500 m loop is located to the west of the survey grid, the sheet is at a depth of 40 m and the background sheet and anomaly (r = 60 m) resistances are 0.1 ohm and 0.01 ohm, respectively (Figure 4-1). Contrary to Example 1, in this example, the secondary horizontal magnetic fields (predominantly H_x^s) are comparable in early time channels and larger at intermediate time channels than the secondary vertical magnetic field. The regularization coefficient, α, was set to zero for the simplified solution and full inversion and data padding was used for the full inversion. The resistance results gridded along the 27 lines can be seen in Figure 4-3.

In this example, both approaches can be used to accurately estimate the background resistance (0.08 to 0.1 ohm) but the simplified solution produces both a conductive and resistive anomaly while the full inversion correctly identifies a single conductive anomaly (slightly offset from the center). If the simplified solution had been used on its own, there may have been some ambiguity as to whether the anomalies are resistive or conductive. Furthermore, uncertainties can also arise if there is a single anomaly on the edge of the grid or on a single line as the interpreter may be unsure if it is truly a single anomaly of the correct resistance or if it is only a portion of a double anomaly (either a conductive or resistive portion).

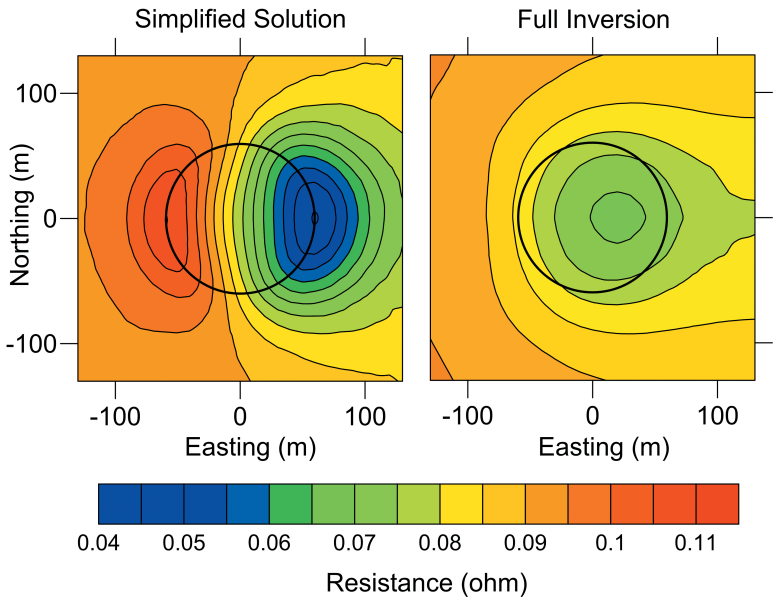

Figure 4-3: Resistance calculated using the simplified solution (equation (4-1), left panel) and the full inversion (equation (4-2) and (4-4), right panel), at t = 0.04 ms for synthetic example 2 (Figure 4-1). Resistances of the background sheet and anomaly (r = 60 m, black circle) are 0.1 ohm and 0.01 ohm, respectively.

4.5.3 Example 3

In the third example, a 400 m by 400 m loop is located to the north of the survey grid, the sheet is at a depth of 20 m and the background sheet and anomaly (r = 40 m) resistances are 1 ohm and 10 ohm, respectively (Figure 4-1). As with Example 2, the secondary horizontal magnetic fields in this survey geometry are comparable to the vertical magnetic field. However, with this model being more resistive and possessing a resistive anomaly (as opposed to a conductive anomaly), the magnetic field strengths are lower than the previous two examples, allowing for numerical noise to be more pronounced (especially in the dH_z^s/dz). The calculated resistance using no regularization can be seen in the top two panels of Figure 4-4. There is a sign reversal in the

dH_z^s/dz at the southern end of the anomaly (away from the loop) and in the simplified solution, this sign reversal causes a negative resistance to be calculated. As such, the absolute value of the resistance with the simplified solution was used. With the full inversion, taking absolute values is unnecessary, since the additional terms in the full inversion ($H_y^s dR/dy$ and $H_x^s dR/dx$) that have been ignored in the simplified solution, result in positive resistances only. Due to the lower signal value and increased noise, the matrix **A** in equation (4-4) is ill-conditioned and, in contrast to the previous two examples, requires regularization in order for a non-erratic solution to be found. A comparison of the two solutions with regularization can be seen in the bottom two panels of Figure 4-4. For the simplified solution and full inversion, the regularization coefficient, α, was selected based on an L-curve and qualitative analysis (5×10^{-5} and 1×10^{-5}, respectively). Data padding was used for both methods and the absolute resistance was used for the simplified solution.

In Figure 4-4 (bottom panels), the regularized full inversion correctly displays a resistive circular anomaly in the center of the survey grid. The size of the anomaly and background resistance is also consistent with the input model parameters. The regularization helps to remove some of the erratic resistance estimates in the simplified solution. However, overall, the regularization does not aid in its interpretation, and in fact, reduces the likelihood it would be correctly interpreted as a resistive anomaly as the conductive portion appears to dominate the map. Moreover, as previously stated, applying regularization to the simplified solution causes the method to lose its advantages over the full inversion. Thus, if regularization is to be applied then the full inversion is recommended.

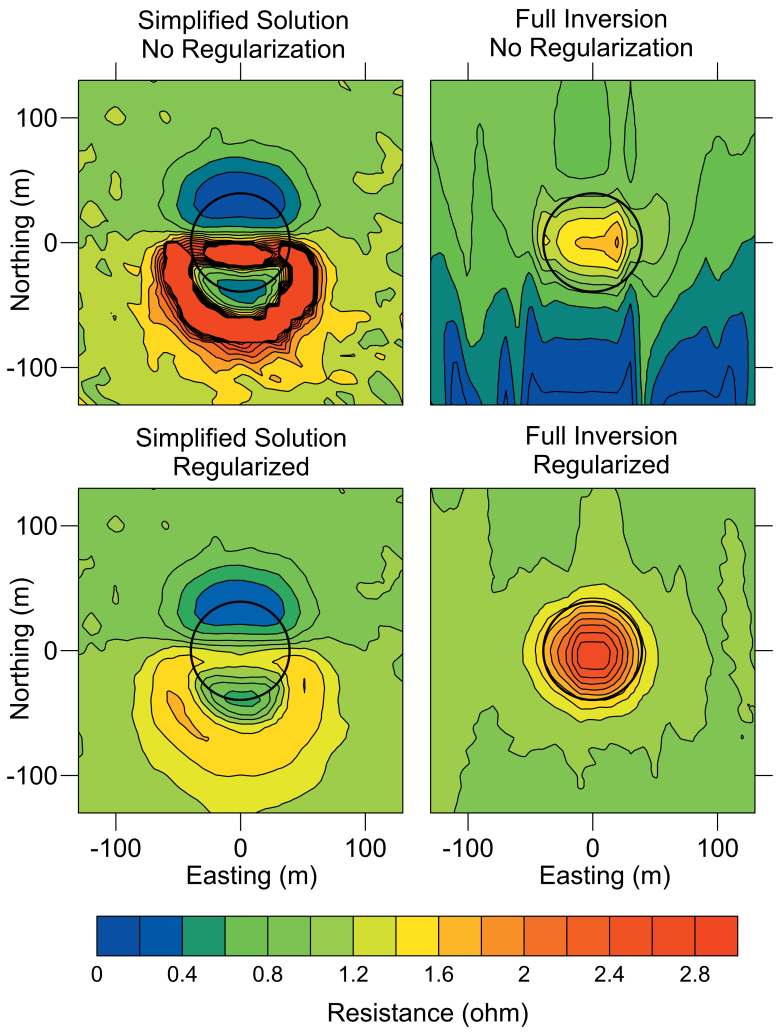

Figure 4-4: Resistance calculated using and not using regularization (bottom and top panels, respectively) for the simplified solution (equation (4-1) and (4-4), left panels) and the full inversion (equation (4-2) and (4-4), right panels) at t = 0.07 ms for synthetic example 3 (Figure 4-1). Background sheet and anomaly (r = 40 m, black circle) are 1 ohm and 10 ohm, respectively.

4.5.4 Discussion on synthetic examples

While no noise (apart from some minimal numerical noise in the forward model solution) was added to the synthetic examples shown, its effects were investigated. In short, the accuracy of the calculated resistance for both the simplified and full inversion relies on the signal-to-noise (S/N) ratio in dH_z^s/dz which is typically the smallest measured (or calculated) field. In practice, as long as the S/N ratio exceeds a factor of 2 to 3, reliable (non-erratic) resistances could be calculated.

Based on the assumptions of Kolaj and Smith (2013), it is clear that the simplified solution relies on terms 2 and 3 of equation (4-2) ($H_y^s dR/dy$ and $H_x^s dR/dx$, respectively) being negligible. This occurs when the product of the spatial resistance derivative and horizontal magnetic field component are small in comparison to the product of the resistance and vertical spatial derivative. This can be analytically investigated by calculating an unreliability parameter, the ratio, T,

$$T = 100 \frac{\left| \frac{dR}{dy} H_y^s + \frac{dR}{dx} H_x^s \right|}{\left| R \frac{dH_z^s}{dz} \right|}, \tag{4-5}$$

where R and its spatial derivatives are calculated from the results of the full inversion. A ratio close to zero would imply that terms 2 and 3 are negligible, while a ratio of 100 would imply that the sum of terms 2 and 3 is of the same size as RdH_z^s/dz. The values of T for each example can be seen in Figure 4-5. Since the resistances, resistance contrasts and survey geometries differ in each example (Figure 4-1), more attention should be paid to the overall trends (high or low, as opposed to their absolute size) in the T ratio when comparing the three examples in Figure 4-5.

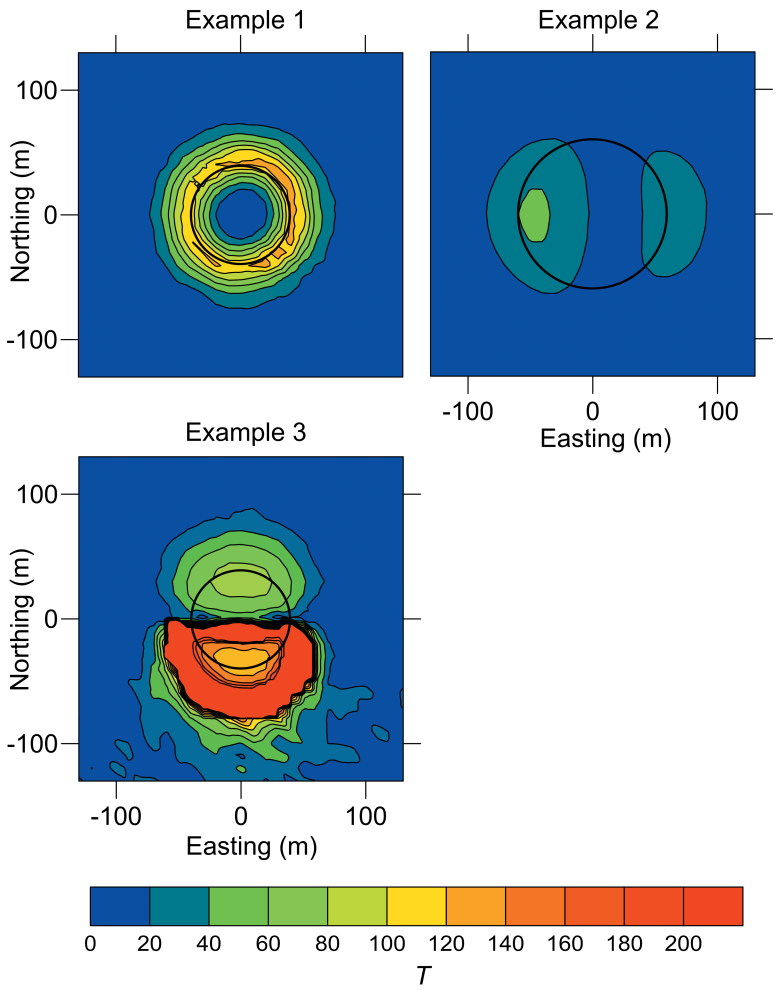

Figure 4-5: The ratio T (an unreliability parameter), calculated using equation (4-5) for examples 1 (t = 0.29 ms), 2 and 3 (regularized example). A high ratio corresponds to areas where terms 2 and 3 of equation (4-2) are too large to be deemed negligible as they are assumed to be in the simplified solution. Anomaly boundaries indicated by a black circle.

In Example 1, the only area where the simplified solution may yield erroneous resistances is directly adjacent to the conductive anomaly where the ignored spatial resistance derivative is the largest (Example 1, Figure 4-5). This is likely what is causing the overshoot/undershoot on the outside of the anomaly (Example 1, Figure 4-2). Terms 2 and 3 are negligible in the center (i.e. T

≈ 0) where the spatial resistance derivative is small due to the size of the body, which allows for the resistance of the anomaly to be determined more accurately. In Examples 2 and 3, the surveys are offset from their transmitter loops and a double anomaly appears in the *T* ratio maps. As the relative size of the horizontal magnetic field in comparison to the vertical magnetic field will be higher in this survey geometry (survey offset from the transmitter loop), there is an increased *T* ratio in both Example 2 and 3. The ratio is not as large further away from the anomaly as the spatial resistance derivatives are much smaller here. As such, the relative contribution of terms 2 and 3 in equation (4-2) are significant in close proximity to resistance contrasts (anomalies) and by ignoring them, erroneous and misleading results can be generated in the simplified solution (i.e. double anomalies, negative resistances, over/under-shoots). If the simplified solution is to be used, the survey should be organized in such a way as to minimize the horizontal magnetic fields, such as by performing the survey inside of the loop, as was done by Kolaj and Smith (2013). However, even if the survey is performed inside of the transmitter loop, it is still important to investigate the *T* ratio. In Example 1, if the conductive anomaly had been located closer to one of the transmitter loop edges (example not shown), then a non-symmetric and potentially large overshoot would have appeared on one side of the anomaly (the side closest to the loop edge where the horizontal magnetic fields are large). Calculating the *T* ratio would ensure that this overshoot is not incorrectly interpreted as an additional anomaly. Furthermore, caution should also be taken around large resistance contrasts and the absolute value of the resistance should be used if there are frequent polarity changes in the input variables.

Ideally, we would like to be able to determine where the simplified solution will give erroneous results without having to compute the full inversion. An approximation of the unreliability

parameter T is termed T', which is identical to equation (4-5) with the exception that the R and its spatial derivatives from the simplified solution, rather than full inversion, are used. The results of T' for each example can be seen in Figure 4-6. The results are generally more erratic as the simplified solution tends to produce more erratic resistances (i.e. Example 3). By comparing Figures 4-5 and 4-6, it is revealed that while the T' ratio is larger, more erratic and does not have as well defined zones as the corresponding T ratio, it is an adequate approximation of T. As such, the unreliability parameter T' can be used to determine where the simplified solution results are unreliable when the full inversion resistance is not available. Unfortunately, both ratios require that the horizontal magnetic field components, which are not required in the simplified solution calculation, are measured.

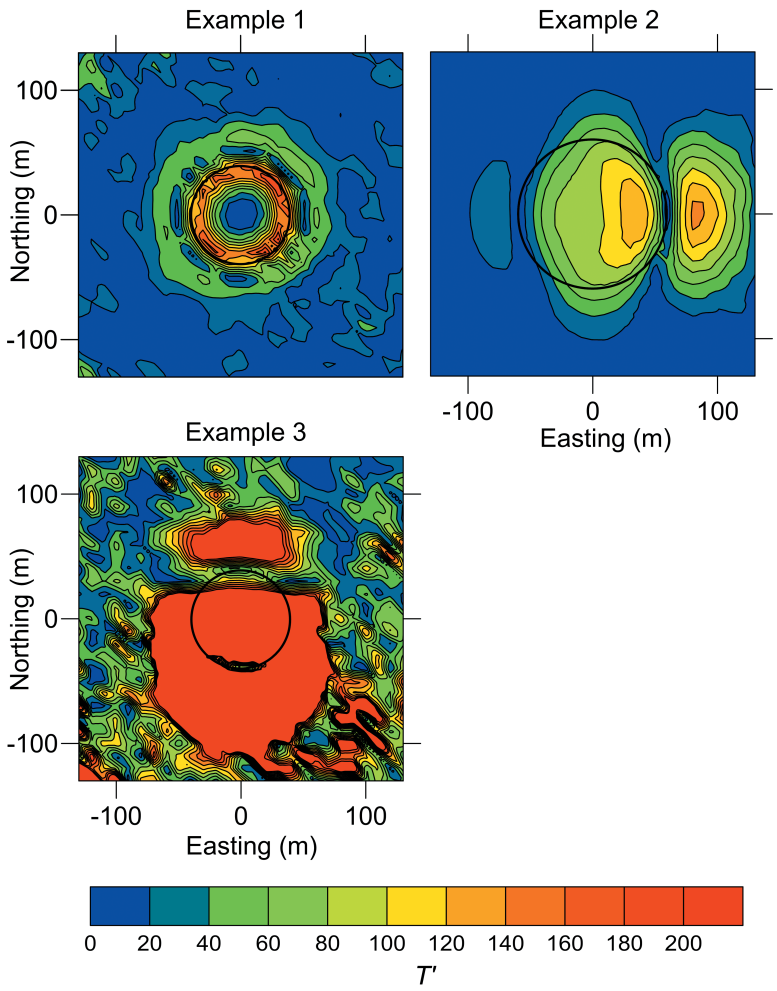

Figure 4-6: The approximate ratio *T'* (an unreliability parameter), calculated using the resistance and its spatial derivatives from the simplified solution in equation (4-5) for examples 1 (t = 0.29 ms), 2 and 3 (non-regularized example). Anomaly boundaries indicated by a black circle.

4.6 Comparison of methods on field data

The full inversion is tested on the TDEM survey data of Kolaj and Smith (2013) where the simplified solution had previously been used. A brief description of the survey details are as follows: The survey was performed with the assistance of Vale and Abitibi Geophysics on a dry

mine tailings pond situated on Vale property in Sudbury, Ontario, Canada. Three Geonics 3D-3 sensor coils each measuring three components (x, y and z) spaced 1.1 m vertically apart were used with a SMARTem 24 receiver (120 kHz sampling rate). A Geonics TEM-57 generated a 30 Hz 50 % duty cycle pulse with an exponential turn on and a linear ramp switch off in a loop approximately 700 m by 350 m (Kolaj and Smith, 2013). The survey was performed inside of the loop with a station spacing of 20 m on 5 lines spaced 40 m apart (line length of approximately 200 m, Figure 4-7). As the survey was inside the loop, we expect the horizontal components to be small and the simplified solution to work well.

Each station was occupied for 2.5 minutes (5 readings of 756 stacks) and the sensor coil output was integrated to give the magnetic field (B_x, B_y, B_z) using the full waveform data (Smith and Annan, 2000). Note that the **B** rather than **H** magnetic fields are used because **B** units (nT) are more commonly used in practice ($\mathbf{B}=\mu_0\mathbf{H}$ where μ_0 is the magnetic permeability of free space). The dB_z/dz was calculated using the difference between the base and the average of the mid and upper sensors (Kolaj and Smith, 2013). Finally, each line was trimmed to only include those stations that were interpreted to be above the thin sheet (Kolaj and Smith, 2013). An example of dB_z/dt, B_x, B_y, and dB_z/dz for the trimmed line 4 can be seen in Figure 4-8.

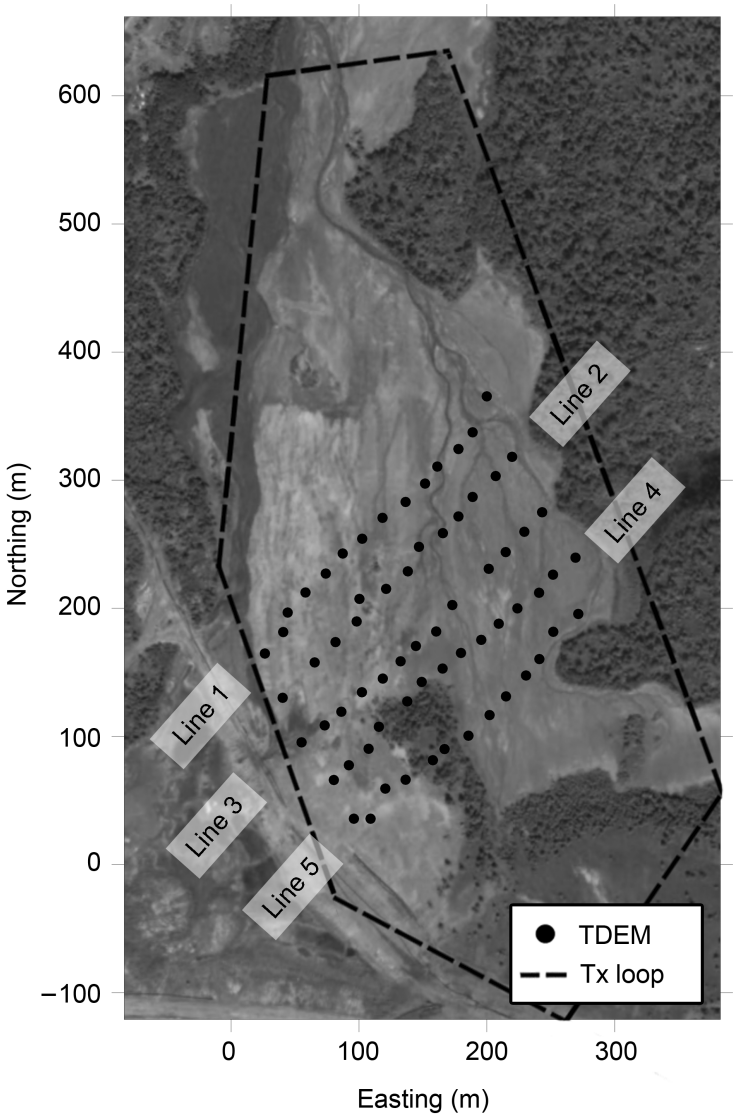

Figure 4-7: Station locations and loop location for the vertical spatial derivative TDEM survey of Kolaj and Smith (2013) superimposed atop an aerial image of the dry tailings pond on Vale property located in Sudbury, Ontario, Canada (modified from Kolaj and Smith, 2013).

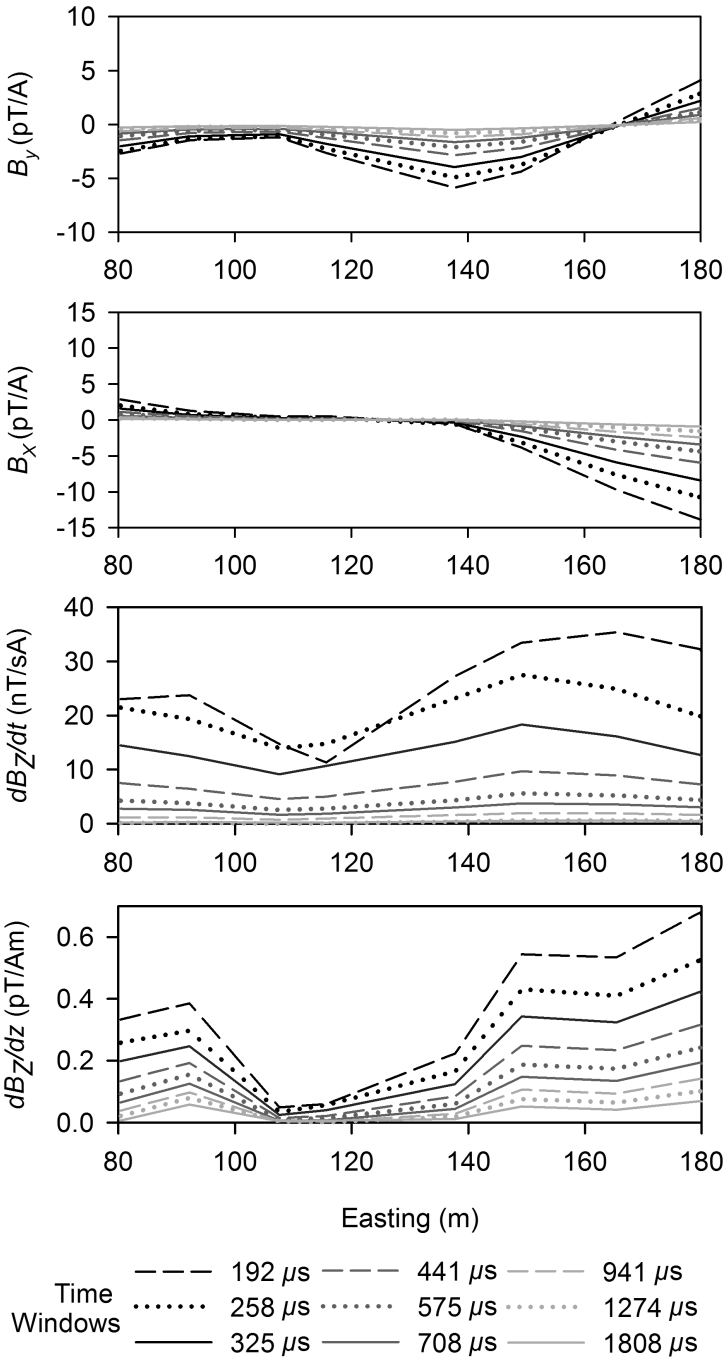

Figure 4-8: Off time, windowed and stacked B_y, B_x, dB_z/dt and dB_z/dz for trimmed line 4 of the TDEM survey of Kolaj and Smith (2013).

The weighting matrix (error matrix, **W** in equation (4-4)) for the full inversion was composed of the standard deviation of the 5 readings of dB_z/dz at each station, and several stations that were thought to be unreliable due to a poor S/N ratio (S/N < 3 for early time and S/N < 2 for intermediate time) were removed entirely (Kolaj and Smith, 2013). Finally, the data was gridded into roughly 5 m by 5 m cells and the full inversion and simplified solution were calculated for early and intermediate times (Figure 4-9). The L-curve analysis (inversion computation times generally less than 0.5 s per α) suggested that no regularization was required but it was found that using minor regularization helped to remove some small artifacts in the resistance. As such, the regularization coefficient, α, was equal to 1.0×10^{-5} for the full inversion and no data padding was used. Note that no regularization was used for the simplified solution as suggested above. Apart from the data trimming, the results of the simplified solution (Figure 4-9) could have been generated in real time in the field. At first glance, both the simplified solution and full inversion have the same overall trend of a resistive zone trending roughly from N-S in the middle of the grid. The increase in the calculated conductance from 192 μs to 575 μs is consistent with the results found in Kolaj and Smith (2013) where it was attributed to either the finite size of the sheet and/or that the conductivity of the tailings continuing or increasing with depth.

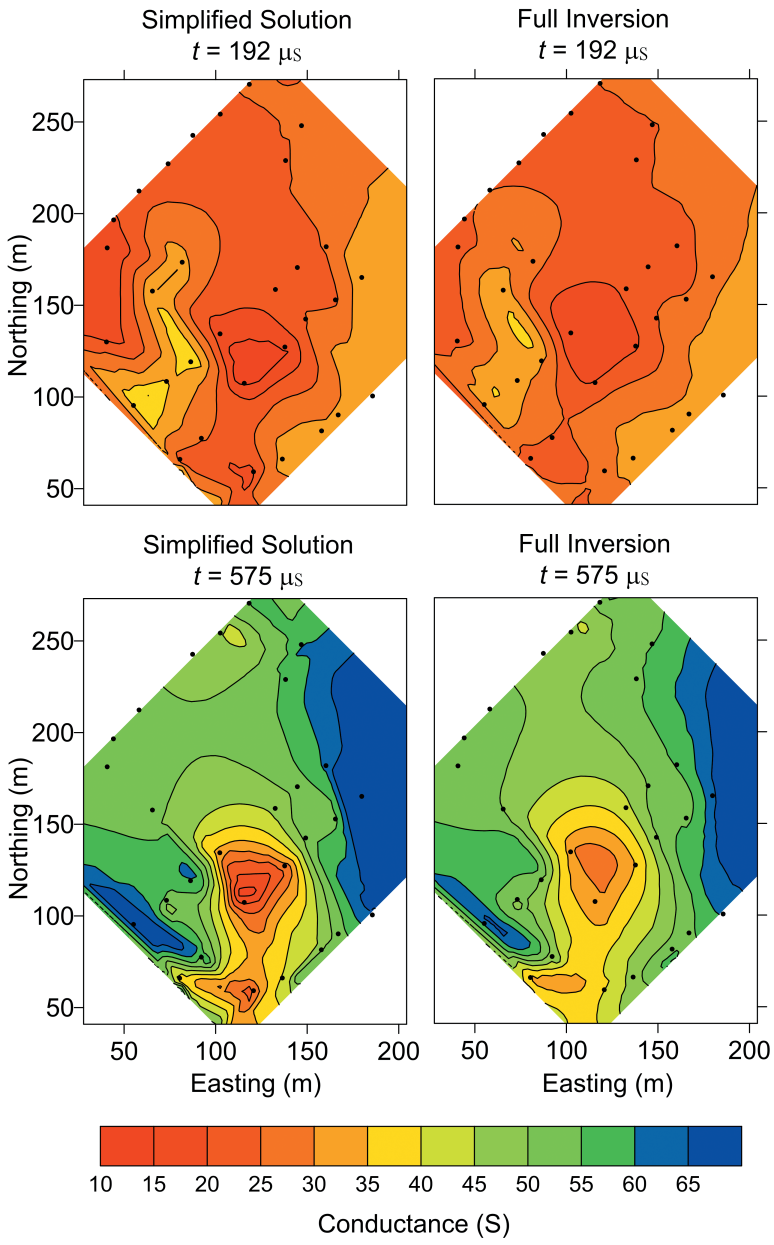

Figure 4-9: Conductance over the dry tailings pond calculated using the simplified solution (left panels) and the full inversion (right panels) for early time (top panels) and intermediate time (bottom panels). Survey data from Kolaj and Smith (2013). Black dots represent the station locations with reliable data.

The differences between the two methods and the validity of the simplified solution can be investigated in more detail in the same manner as in the modeling section (i.e. by calculating the unreliability parameters, the ratio *T*, and/or the approximate ratio, *T'*, from equation (4-5)). These results can be seen in Figure 4-10. While *T'* is only an approximation, it defines the same general locations as *T* in Figure 4-10. The largest ratio occurs overtop the resistive anomalies and somewhat overtop the conductive band seen in the top panels of Figure 4-9 (not shown well in Figure 4-10 due to the scale of the color bar). Three profiles have been placed on Figure 4-10, positioned so that profile 1 is in an area where the ratio, *T*, is smallest, while profile 3 has the largest ratio. Based on the forward modeling we do not expect large differences between the simplified solution and the full inversion when the survey is inside the loop. Where there are discrepancies between the methods, it is likely to be an overshoot or undershoot due mainly to lateral changes in resistance (i.e. large values of the resistance derivatives). However, as seen in Figure 4-8, the horizontal magnetic fields are more significant in certain areas, especially along the eastern end of the survey lines, which may also cause some differences between the conductances calculated with the two methods. In profile 1, the resistance varies gradually and as such, the resistance gradient is small and there are only minor differences between the two methods and the *T* and *T'* ratios are small (Figure 4-11). In profiles 2 and 3, there are more sudden resistance changes which cause small overshoots and undershoots on the simplified solution results prior to the resistive and conductive anomalies, respectively. For the large resistive anomaly in profile 3, the full inversion suggests an anomaly which is less resistive than the simplified solution implies. In both profiles, the increased *T* and *T'* ratio zones coincide well with areas where the conductances differ.

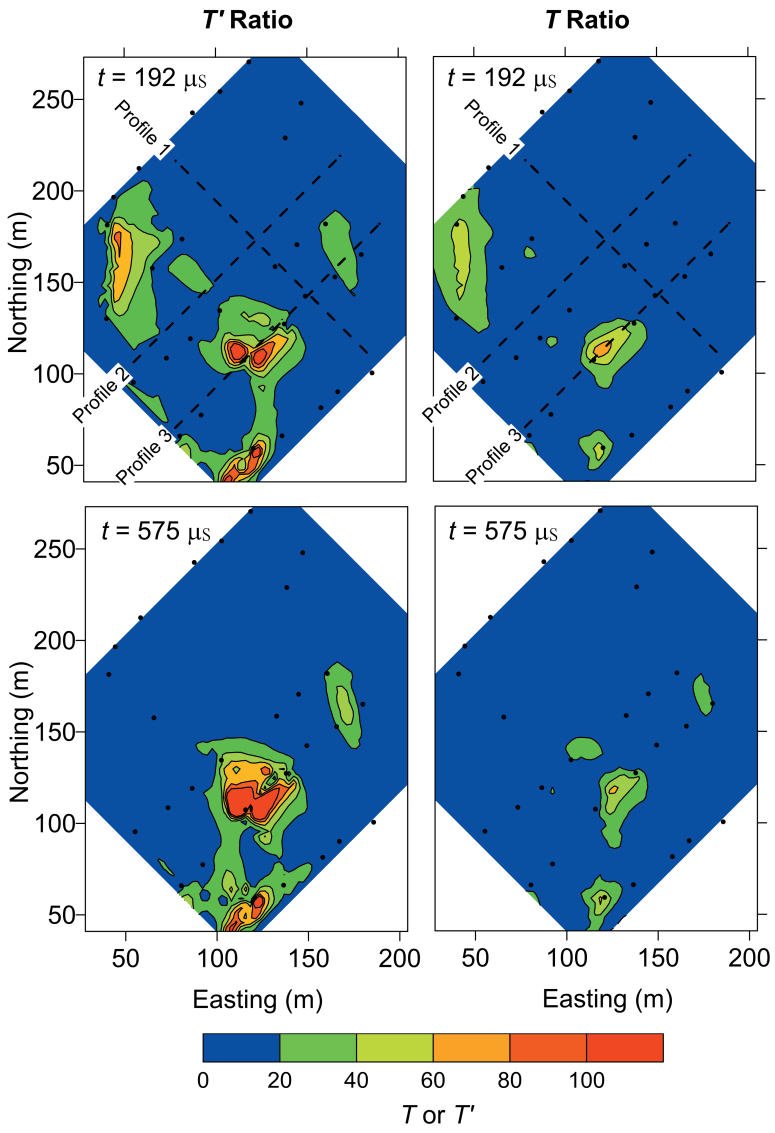

Figure 4-10: The approximate ratio, *T'*, and the ratio, *T*, (left and right panels, respectively) calculated using equation (4-5) for Figure 4-9 at both early and intermediate times (top and bottom panels, respectively). Black dots represent the station locations with reliable data. Dashed lines represent location of the profiles used for Figure 4-11.

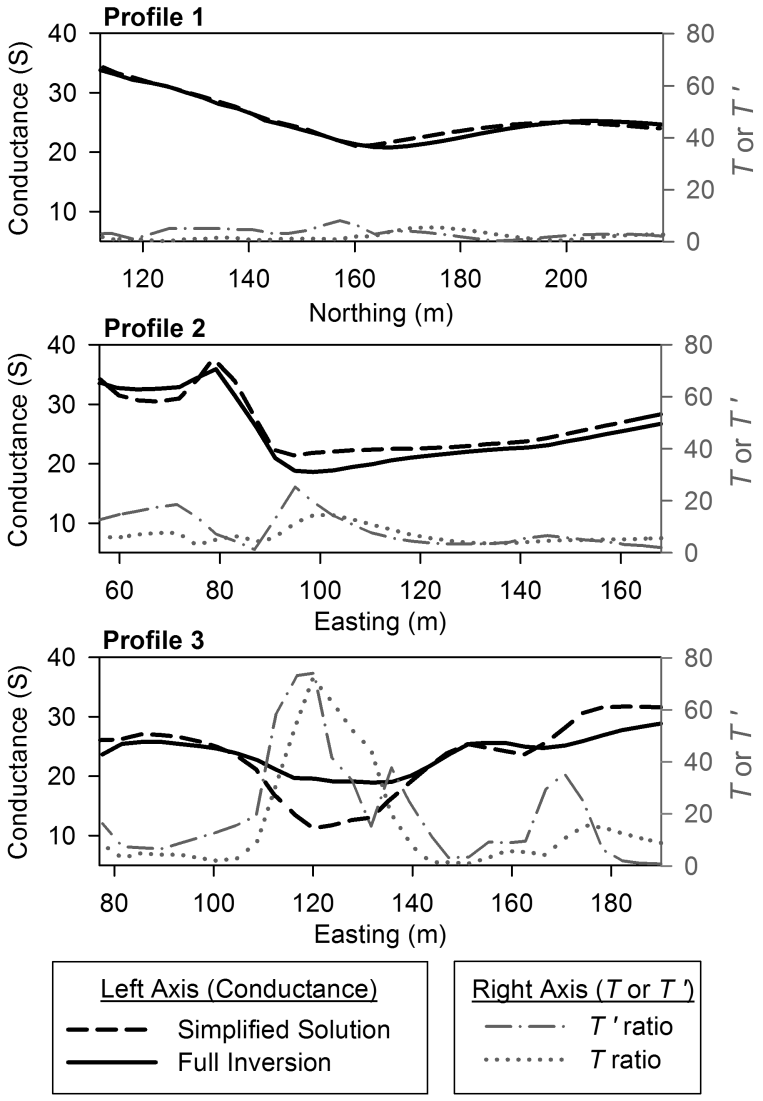

Figure 4-11: The left axis corresponds to the conductance as calculated using the simplified solution (dashed black line) and full inversion (solid black line) at early time (t = 192 μs) for the profile locations shown in Figure 4-10. The right axis corresponds to the corresponding T' (dash-dot grey line) and T (dotted grey line) ratios.

In this field example, while the full inversion does correct some erroneous values found with the simplified solution, the simplified solution does appear to be an adequate approximation. Furthermore, the *T'* ratio (which can be computed without the full inversion and potentially in real-time along with the simplified solution) accurately indicated the zones where the simplified solution may be unreliable. Unfortunately, the unreliability parameters (*T* or *T'*) do not indicate in what sense the simplified solution may be erroneous. As such, had only the simplified solution and *T'* ratio been available and had the resistive anomaly been a target of interest, then a follow up of the full inversion may have been sought. If the simplified solution was done in the field, then the surveyors may have opted to collect more dense data in and around the resistive anomaly to improve the results of the full inversion. If an out-of-loop survey was collected instead, then the synthetic models show that artifacts such as low/high resistance doubles and overshoot and undershoot would have been more prevalent. In this case, it would be more important to look critically at the *T* or *T'* values.

4.7 Conclusion and Future Work

The differential equation which describes the electromagnetic induction in a laterally extensive thin sheet with a varying resistance can be inverted for resistance using the simplified solution of Kolaj and Smith (2013) or the full inversion approach derived here. The full inversion approach (equation (4-2)) is derived for magnetic fields measured directly at the surface of a conductive thin sheet, but, with synthetic models we showed that reliable resistances can also be calculated using equation (4-2) above shallow thin sheets. The simplified solution relies on the assumption that $H_y^s dR/dy$ and $H_x^s dR/dx$ are negligible in comparison to RdH_z^s/dz which we have shown through synthetic modeling is generally only valid when the survey is performed inside of the

loop and where there are minimal resistance contrasts. If the assumptions are invalid, the simplified solution can generate erroneous and misleading results in the form of dipolar (conductive and resistive) anomalies in place of single anomalies. Other erroneous artifacts include negative resistances and estimates that overshoot and/or undershoot near resistance contrasts. By identifying where the ratio T (an unreliability parameter) is large (or the approximate ratio, T', if the full inversion is not available) the areas where the simplified solution will give erroneous results can be identified. Comparison of the two methods using real field data collected overtop a dry tailings pond in Sudbury, Ontario, Canada with a fixed in-loop survey geometry showed small differences between the resistances calculated using the two methods, the majority of which correlated with sudden resistance changes or areas where the horizontal magnetic fields were more significant. The good agreement between the simplified solution and full inversion is consistent with the unreliability parameters T and T' being generally less than 100 in the survey area (i.e. the neglected terms in the simplified solution are small in comparison to the terms included).

In the simplified solution of Kolaj and Smith (2013), each station is independent of the other and as such, the simplified solution could be performed with a single station. However, the full inversion involves spatial resistance derivatives that are calculated using finite difference operators and as such, the inversion requires line/grid data (and interpolation if the grid is not adequately dense). The simplified solution also does not require the collection of horizontal magnetic fields which may save time depending on the equipment used. Furthermore, the simplified solution could be quickly calculated in the field in real time as it only requires simple arithmetic (assuming that both the vertical magnetic field and its time derivative are measured or can be calculated from the data) whereas the full inversion is a more complex algorithm which

requires some user input (selecting a suitable regularization coefficient and padding the data). As such, the simplified solution is a good candidate as a first pass and/or field interpretation provided that the survey is designed in a way to minimize the horizontal magnetic fields and caution is taken around resistance contrasts. Furthermore, if horizontal magnetic fields are recorded, the ratio *T'* can potentially be calculated alongside the simplified solution in the field (or trivially post data collection) which will indicate zones where the simplified solution may be providing unreliable conductance estimates. For example, the simplified solution could be performed in the field, possibly with large station spacing, to identify areas of interest and zones where the *T'* ratio is acceptable. If necessary, more finely spaced and/or grid data could then be acquired for the more reliable/accurate full inversion over any areas of interest or zones where the *T'* ratio is found to be above some threshold. While the synthetic tests and the field trial focused on fixed loop TDEM systems, the simplified solution and full inversion can also be used with frequency domain and/or moving (airborne) EM systems.

In this paper we solved for resistance at each delay time rather than for a single resistance which is consistent with all delay times. This was done to potentially track for variations in resistance with time that may be associated with changes in the resistivity with depth. In our future work we aim to use this information to generate resistivity depth sections.

4.8 References

Chouteau, M., O. Anterrieu, M. Aubertin, C. Dubreuil-Boisclair, and J. Poisson, 2006, Geophysical characterization of an AMD-generating waste rock pile using ground and borehole techniques: SAGEEP Proceedings 2006, 128-139.

Frischknecht, F. C., V. F. Labson, B. R. Spies, and W. L. Anderson, 1991, Profiling methods using small sources, *in* M. N. Nabighian, ed., Electromagnetic methods in applied geophysics, Applications, Part A and B: SEG, Investigations in Geophysics No. 3, Volume **2**, 105–270.

Grant, F. S., and G. F. West, 1965, Interpretation theory in applied geophysics. McGraw-Hill.

Haber, E., D. W. Oldenburg, and R. Shekhtman, 2007, Inversion of time domain three-dimensional electromagnetic data: Geophysical Journal International, **171**, 550–564.

Hohmann, G. W., and A. P. Raiche 1987, Inversion of controlled-source electromagnetic data, *in* M. N. Nabighian, ed., Electromagnetic methods in applied geophysics, Theory, Investigations in Geophysics Volume **1**, 469-503.

Irvine, R. J., and G. Staltari, 1984, Case history illustrating problems in transient electromagnetic surveys: Exploration Geophysics, **15**, 155-167.

Joshi, M. S., O. P. Gupta, and J. G. Negi, 1988, On the effects of thickness of the half-plane model in HLEM induction prospecting over sulphide dykes in a highly resistive medium: Geophysical Prospecting, **36**, 551– 558.

Keating, P. B., and D. J. Crossley, 1990, The inversion of time-domain airborne electromagnetic data using the plate model: Geophysics, **55**, 705-711.

Kolaj, M, and R. S. Smith, 2013, Using spatial derivatives of electromagnetic data to map lateral conductance variations in thin sheet models: applications over mine tailings ponds: Geophysics, **78**, E225-E235.

Liu, G., and M. Asten, 1993, Conductance–depth imaging of airborne TEM data: Exploration Geophysics, **24**, 655– 662.

Macnae, J. C., and Y. Lamontagne, 1987, Imaging quasi-layered conductive structures by simple processing of transient electromagnetic data: Geophysics, **52**, 545–554.

Macnae, J., 2007, Developments in broadband airborne electromagnetics in the past decade, *in* B. Milkereit, ed., Proceedings of Exploration 07: Fifth Decennial International Conference on Mineral Exploration, 387–398.

Nabighian, M. N., and J. C. Macnae, 1991, Time domain electromagnetic prospecting methods, *in* M. N. Nabighian, ed., Electromagnetic methods in applied geophysics, Applications, Part A and B: SEG, Investigations in Geophysics No. 3, Volume **2**, 427–520.

Palacky, G. J., 1987, Resistivity characteristics of geological targets, *in* M. N. Nabighian, ed., Electromagnetic methods in applied geophysics, Theory, Investigations in Geophysics Volume **1**, 53-125.

Peric, M., 1981, Exploration of Burundi nickeliferous laterites by electrical methods: Geophysical Prospecting, **29**, 274-287.

Price, A. T., 1949, The induction of electric currents in non uniform thin sheets and shells: Quarterly Journal of Mechanics and Applied Mathematics, **2**, 283-310.

Rutherford, J., T. Munday, J. Meyers, and M. Cooper, 2001, Relationship between regolith materials, petrophysical properties, hydrologeology and mineralisation at the Cawse Ni laterite

deposits, Western Australia: Implications for exploring with airborne EM: Exploration Geophysics, **32**, 160-170.

Sattel, D., and *J*. C. Macnae, 2001, The feasibility of electromagnetic gradiometer measurements: Geophysical Prospecting, **49**, 309–320.

Seigel, H. O., and D. H. Pitcher, 1978, Mapping earth conductivities using a multifrequency airborne electromagnetic system: Geophysics, **43**, 563-575.

Smith, R. S., 2000, The realizable resistive limit: A new concept for mapping geological features spanning a broad range of conductances: Geophysics, **65**, 1124–1127.

Smith, R. S. and A. P Annan, 2000, Using an induction coil sensor to indirectly measure the B-field response in the bandwidth of the transient electromagnetic method: Geophysics, **65**, 1489-1494.

Smith, R. S., and G. F. West, 1987, Electromagnetic induction in an inhomogeneous conductive thin sheet: Geophysics, **52**, 1677-1688.

Swidinsky, A., and R. N. Edwards, 2009, The transient electromagnetic response of a resistive sheet: straightforward but not trivial: Geophysical Journal International, **179**, 1488–1498.

Tartaras, E., M. S. Zhdanov, K. Wada, A. Saito, and T. Hara, 2000, Fast imaging of TDEM data based on S-inversion: Journal of Applied Geophysics, **43**, 15–32.

Telford, W. M., L. P. Geldart, and R. E. Sheriff, 1990, Applied geophysics: Cambridge University Press.

Walker, P., and Y. Lamontagne, 2006, Electromagnetic interpretation in complex geological environments: SEG Technical Program Expanded Abstracts 2006, 1288-1292.

Walker, P., and Y. Lamontagne, 2007, Electromagnetic modeling of the Cree Lake Extension Millenium Deposit, with MultiLoop III, *in* B. Milkereit, ed., Proceedings of Exploration 07: Fifth Decennial International Conference on Mineral Exploration, 1077–1080.

West, G. F., J. C. Macnae, and Y. Lamontagne, 1984, A time-domain EM system measuring the step response of the ground: Geophysics, **49**, 1010–1026.

Zhdanov, M. S., 2002, Geophysical inverse theory and regularization problems: Elsevier Science.

Zhdanov, M. S., 2010, Electromagnetic geophysics: Notes from the past and the road ahead: Geophysics, **75**, No. 5, 75A49-75A66.

Chapter 5

5 Robust conductance estimates from spatial and temporal derivatives of borehole electromagnetic data

5.1 Abstract

The conductance of an infinite uniformly conductive thin sheet can be calculated using the ratio of the temporal gradient and the spatial gradient in the normal direction of any component (or combination of components) of the secondary magnetic field. With standard borehole electromagnetic (BHEM) systems, the temporal gradient can either be measured or readily calculated from transient magnetic field data and the spatial gradient in the normal direction can be estimated using adjacent stations. Synthetic modeling demonstrates that for a finite thin sheet the magnitude of the field provided a robust and reliable apparent conductance in typical 3-component BHEM survey configurations. The accuracy in which the apparent conductance can be calculated is hindered by low spatial gradient signal values and can only be reliably estimated where the fields are large (i.e. in close proximity to the target). In a field example of BHEM data collected over a massive sulfide deposit in Sudbury, Ontario, Canada, the spatial gradient could be calculated over a roughly 100 m wide zone and a consistent apparent conductance could be calculated at each delay time using the magnitude of the field. Increases in the apparent conductance with increasing delay time are likely due to currents migrating into more conductive parts of the body. The apparent conductance values are also consistent with Maxwell models and time constant derived conductance estimates. This simple and robust apparent conductance is

ideal as a first pass estimate for target discrimination, grade estimation and starting values for forward and/or inversion modeling.

5.2 Introduction

The success of inductive borehole electromagnetic (BHEM) methods in the exploration for base metals can be attributed to the methods' ability to detect conductive mineralization (which is often the deposit itself) and other conductive geological features of interest (Dyck, 1991). These conductive features can be identified some distance from the hole (Dyck, 1991). In massive sulfide exploration, the contrast in conductivity between crystalline basement rock and massive sulfides can be as high as 10^9 and with exploration in mature districts such as Sudbury, Ontario, Canada often exceeding depths of 1 km, BHEM is often the primary tool for geophysical exploration and characterization (King, 2007). BHEM interpretation generally involves identifying if there is a conductor proximal to the hole by the existence of an anomalous response. If there is an anomaly, the interpreter will determine the distance to the target (if not intersected) and the orientation of the target. The interpretation exercise is generally undertaken through forward and inversion modeling of the measured data (Dyck 1991; Polzer, 2000).

The quantitative forward and inversion modeling approach in mineral exploration BHEM varies from manual methods (the interpreter generates synthetic models, using software such as MultiLoop, until the synthetic data resembles the field data; Lamontagne, 2007) to semi-automated methods (the interpreter generates a model which somewhat resembles the field data and then automated inversion fine-tunes the model to provide a better match) to the less common but nearly fully automated methods (inversion algorithms such as the one found in Zhang and Xiao, 2001). In mineral exploration, the targets (especially massive sulfides) can often be well

represented as thin sheets and many BHEM interpretation procedures take advantage of this (Grant and West, 1965; Palacky 1987; Polzer 2000; King 2007). Like the majority of quantitative geophysical techniques, many of these routines are complicated, suffer from non-uniqueness and the output model may depend strongly on having reliable starting information (Li and Oldenburg, 2000; Oldenburg and Pratt, 2007; Lamontagne 2007; Lelievre et al., 2009). It is more convenient to have a simple method to calculate the conductance directly from BHEM data but typical methods often rely on using circuit theory and/or fitting exponential decays. Historically, (and still in practice today) the conductance can be estimated from the decay rate of the body at late time (Nabighian and Macnae, 1991). For a thin sheet, the conductance is proportional to $10\tau/\mu L$, where τ is the time constant of the body and L is typically the smallest dimension of the sheet (either the strike or down-dip length). The time constant is generally estimated by fitting an exponential decay to the late time measured response. This method is often only reliable far from the source or at late time where the high frequency information has decayed as the method effectively assumes that only the lowest order decay mode (large and smooth current system) is being observed (B. Polzer, personal communication, 2013).

Three benefits of having reliable estimates of conductivity or conductance (product of conductivity and thickness) are 1) to have better starting models for forward and inversion modeling; 2) for improved target discrimination (King, 2007); and 3) an ability to estimate grade variation within the target (McDowell et al., 2007).

An independent way of obtaining a conductivity/conductance estimate is to use a galvanic or inductive borehole probe or laboratory equipment (e.g. handheld conductivity meter on the core; Smith et al., 2012). In addition to having to collect additional data, different borehole probes and laboratory techniques measure the conductivity over a different scale length and typically often

provide drastically different values. Other difficulties with these measurements include the availability of equipment, the additional cost and the fact that the samples may not be available (i.e. no recovered core; Smith et al., 2012). As such, the use of a simple and robust method to calculate the target conductance directly from BHEM data is justified.

The method presented in this paper uses the formulation of Kolaj and Smith (2013), whom developed a methodology to estimate the conductance of a thin sheet from time-domain EM data using the ratio of the temporal gradient and the gradient in the vertical direction of the vertical secondary magnetic field. This work was done assuming that the buried sheet was horizontal and that the receivers were on the surface. We show that for an infinite uniform sheet, any magnetic field component (or combination of components) can be used to estimate the conductance. Through synthetic studies we show that reliable results can be obtained when using the magnitude of the magnetic field to calculate an apparent conductance for finite sized sheets. This apparent conductance is robust as it is relatively insensitive to varying transmitter positions, the borehole location within the target and the borehole/sheet orientation. Lastly, we show results from a field example, where the apparent conductance is calculated from two typical 3-component BHEM surveys collected over a massive sulfide target in Sudbury, Ontario, Canada.

5.3 Theory

The thin sheet assumption allows for substantial simplification of the EM induction problem due to the ability to define a surface current which is constrained to flow only in the plane of the sheet (Price, 1949). Furthermore, simple relationships between the magnetic field components directly above and below the sheet can be derived (Grant and West, 1965). Following Price

(1949), Smith and West (1987), and Kolaj and Smith (2013), these simplifications allow for a simple differential equation for a flat-lying thin sheet in a resistive medium to be derived as,

$$-\frac{dH_z^s}{dz}R + \frac{dR}{dy}H_y^s + \frac{dR}{dx}H_x^s = -\frac{\mu}{2}\frac{dH_z}{dt}, \tag{5-1}$$

where $R(x,y)$ is the resistance of the sheet, μ is the magnetic permeability (generally assumed to be that of free space), and the variables dH_z^s/dz, H_y^s, H_x^s and dH_z/dt are measured directly above (or below) the sheet, where the vector field $\mathbf{H}^S=(H_x^s, H_y^s, H_z^s)$ represents the secondary field emanating from the sheet and **H** represents the vector of the total field (secondary field plus the primary field from the transmitter, $\mathbf{H} = \mathbf{H}^S + \mathbf{H}^P$). In equation (5-1), the sheet is assumed to be in the horizontal plane which, if untrue, the 3-component magnetic field (H_z, H_x, H_y) would need to be rotated so that the H_z component was normal to the sheet. As discussed in Kolaj and Smith (2013), by assuming that the sheet is infinite in extent and that the sheet is of uniform resistance so the dR/dx and dR/dy terms can be ignored, a conductance can be estimated from

$$C = \frac{2}{\mu}\left(\frac{\frac{dH_n^s}{dn}}{\frac{dH_n}{dt}}\right), \tag{5-2}$$

where C is the conductance (inverse of the resistance, R), and n represents the normal component to the thin sheet such that the restriction that the sheet is in the horizontal plane is no longer necessary. Furthermore, in the off-time or when the primary field is constant, the temporal derivative will be solely a secondary field (i.e. $dH_n^P/dt = 0$). This ratio can therefore be independent of the transmitter (location and current waveform) which adds to the simplicity of the method. If the sheet is not uniform or infinite, then equation (5-2) will not yield a conductance, but an apparent conductance.

Equation (5-2) can be investigated in more detail using image theory in cylindrical coordinates (Grant and West, 1965). If the transmitting source is a vertical dipole situated at (0, h) with moment m which disappears at time zero and the infinite sheet of conductance, C, is located in the plane $z = 0$ then the secondary magnetic fields can be shown to be equal to,

$$\mathbf{H}^S(\rho, z, t) = \frac{m}{4\pi}\left[\frac{3\rho a}{(\rho^2 + a^2)^{\frac{5}{2}}}\mathbf{i}_\rho + \frac{2a^2 - \rho^2}{(\rho^2 + a^2)^{\frac{5}{2}}}\mathbf{i}_z\right], \tag{5-3}$$

where $a = z + h + (2t/\mu C)$ and $\mathbf{i}_\rho$ and $\mathbf{i}_z$ are the unit vectors along the ρ and z axes, respectively (there is no field in the φ direction as the primary field has no component in this direction, Telford et al., 1990). This is known as Maxwell's receding image solution (Grant and West, 1965) as the secondary magnetic fields are equal to the image of the source receding downwards with a velocity of $(2t/\mu C)$. Differentiating $\mathbf{H}^S$ with respect to z and t yields,

$$\frac{d\mathbf{H}^S}{dz}(\rho, z, t) = \frac{3m}{4\pi}\left[\frac{\rho(\rho^2 - 4a^2)}{(\rho^2 + a^2)^{\frac{7}{2}}}\mathbf{i}_\rho + \frac{a(3\rho^2 - 2a^2)}{(\rho + a^2)^{\frac{7}{2}}}\mathbf{i}_z\right], \tag{5-4}$$

and

$$\frac{d\mathbf{H}^S}{dt}(\rho, z, t) = \frac{3m}{2\pi C\mu}\left[\frac{\rho(\rho^2 - 4a^2)}{(\rho^2 + a^2)^{\frac{7}{2}}}\mathbf{i}_\rho + \frac{a(3\rho^2 - 2a^2)}{(\rho^2 + a^2)^{\frac{7}{2}}}\mathbf{i}_z\right], \tag{5-5}$$

respectively. Notice that the terms on the right-hand-side in square brackets are identical. Thus, by dividing the vertical components of equation (5-4) and (5-5), a factor of $(\mu C/2)$ remains which is the expected result based upon equation (5-2). However, as evident in equations (5-4) and (5-5), this relationship is also true for other components of the vector, specifically H_ρ. This same conclusion can also be deduced by the observation that H_ρ and H_z are of the same form (equation (5-3)) and the difference between the t and z derivative is controlled by the term, a,

where $da/dz = 0$ and $da/dt = 2/\mu C$. As all the components result in the same answer, any linear combination of the components, including the magnitude, $H_m = (H_\rho^2 + H_z^2)^{0.5}$, can be used in the calculation of the conductance. Furthermore, while equation (5-1) is valid only directly above or below the sheet, equation (5-2) (with any component) is valid for measurements made at any distance away from the sheet.

Equation (5-2) requires measurements of both the magnetic field and its time derivative, which can be obtained by using a magnetic field sensor and then estimating its time derivative using adjacent delay times, i.e., a finite forward difference scheme such as

$$\frac{d\mathbf{H}^s(k, t_j + 0.5\Delta t)}{dt} = \frac{\mathbf{H}^s(k, t_{j+1}) - \mathbf{H}^s(k, t_j)}{\Delta t}, \tag{5-6}$$

where k represents the station, j represents the channel number and Δt is the difference in time between the two adjacent time channels. Alternatively, if using an induction coil (time derivative) sensor, then the full-waveform time derivative measurements can be integrated to give a magnetic field (Smith and Annan, 2000). The derivative in the normal direction of the magnetic field for a flat lying sheet and a vertical borehole can be approximated using the difference between stations, i.e., a finite central difference scheme such as

$$\frac{d\mathbf{H}^s(k, t_j)}{dz} = \frac{\mathbf{H}^s(k+1, t_j) - \mathbf{H}^s(k-1, t_j)}{\Delta z}, \tag{5-7}$$

where z is the depth and Δz is the change in depth between the station directly below and above the station, k. A comparison of the spatial and temporal derivatives (calculated using equations (5-6) and (5-7), respectively) and the calculated conductance (equation (5-2)) using different components for an analytical solution of a 1000 S infinite horizontal sheet at a depth of 300 m

can be seen in Figure 5-1. As opposed to equations (5-3), (5-4) and (5-5), the transmitter is a 400 m by 200 m rectangular loop and is located 100 m to the east of the borehole. Note that the calculated conductance differs slightly in close proximity to the sheet as the derivatives have been estimated using a finite difference approach (equations (5-6) and (5-7)).

While it is now clear that any component that is not null-coupled to the secondary field can be used to calculate the conductance of an infinite sheet, it is not as easy to prove how effective the different components will be at calculating an apparent conductance of finite non-uniform thin sheets. Furthermore, $d\mathbf{H}^s/dz = d\mathbf{H}^s/dn$ only when the borehole axis is normal to the sheet, and as such, erratic/erroneous conductance estimates may occur when $d\mathbf{H}^s/dz$ (equation (5-7)) is used instead of $d\mathbf{H}^s/dn$ to calculate the conductance (equation (5-2)) for different survey/model geometries. These issues will be further investigated through forward modeling of finite and dipping thin sheets in the following section.

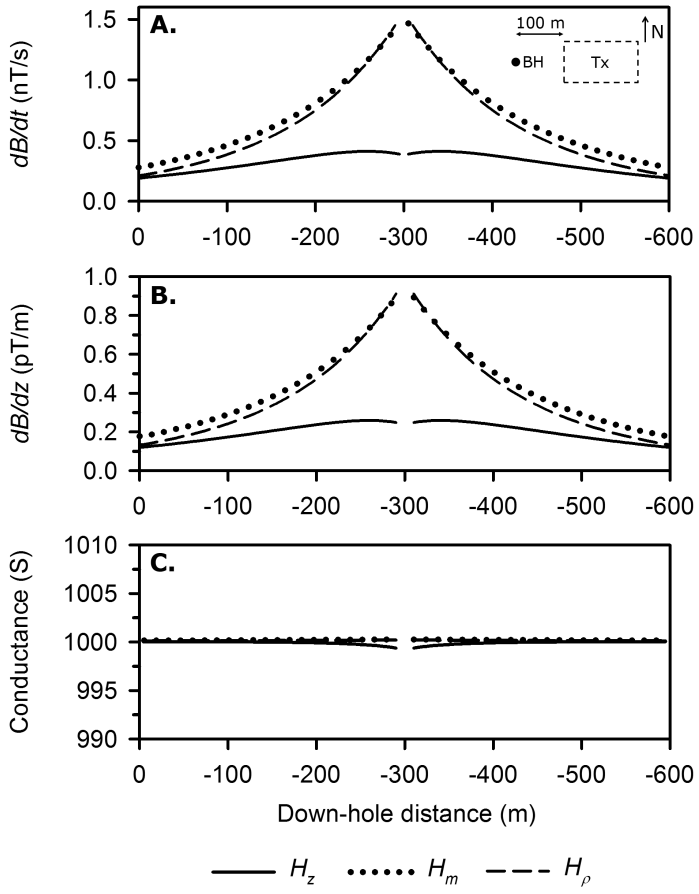

Figure 5-1: Comparison of equation (5-2) using H_z (solid line), H_m (dotted line) and H_ρ (dashed line) for a step response at t = 1.1 ms intersecting a horizontal 1000 S infinite sheet located at a depth of -300 m. The station spacing is 5 m and several stations in close proximity to the sheet have been removed. A 400 m by 200 m transmitter is located 300 m east of the borehole (geometry depicted in top right corner). A. Absolute magnitude of the time derivative of the vertical component (dB_z/dt), the magnitude (dB_m/dt) and the horizontal component (dB_ρ/dt). B. Absolute magnitude of the spatial derivative of the vertical component (dB^S_z/dn), the magnitude (dB^S_m/dz_m) and the horizontal component (dB^S_ρ/dz_m). C. Conductance calculated from the ratio of the fields in A and B. Note that **B** magnetic fields are shown in this and subsequent figures, as **B**-field units (nT) are more commonly used in practice (conversion $\mathbf{B}=\mu\mathbf{H}$).

5.4 Forward Modeling

In each example, a 1 Hz BHEM UTEM survey (West et al., 1984) with station spacing of 10 m was simulated in MultiLoop III (Lamontagne Geophysics, Walker and Lamontagne, 2006). A general schematic of the synthetic model can be seen in Figure 5-2. Since a UTEM survey measures the magnetic field at each station, the spatial derivative was calculated using a central difference between stations (equation (5-7)) and the time derivative was calculated using the forward difference between adjacent delay times (equation (5-6)). Since the time derivative is calculated using adjacent delay times, the spatial derivative is also averaged over adjacent delay times. Additional survey parameters are stated before each example. Note that no noise (apart from some numerical noise) was added to the data.

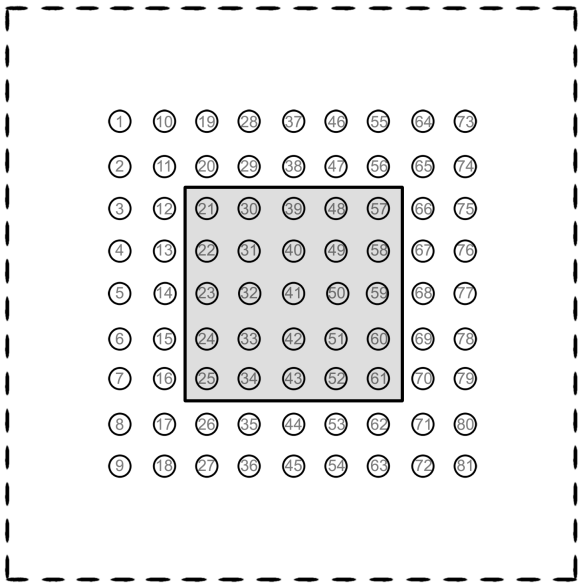

Figure 5-2: Plan view of the generalized survey geometry for the synthetic models used in MultiLoop III. Dashed black line represents the transmitter loop, circles represent the boreholes (numbered 1-81, spaced 50 m apart) and the central grey square represents the surface projection of the thin sheet.

5.4.1 Synthetic Example 1- zero dip

In the first example, a 600 m by 600 m loop was positioned around the survey area (Figure 5-2) containing a 250 m by 250 m sheet at a depth of 200 m having a conductance of 10000 S with boreholes (BH) oriented normal to the sheet (i.e. no dip; $d\mathbf{H}^s/dz = d\mathbf{H}^s/dn$). The results of equation (5-2) for early and late time using the vertical ($H_n = H_z$), horizontal (H_ρ) and magnitude (H_m) components for borehole #41 (central hole) and borehole #21 (corner of sheet) can be seen in Figure 5-3 (there is no horizontal component for the central borehole as these fields are essentially null coupled to the body).

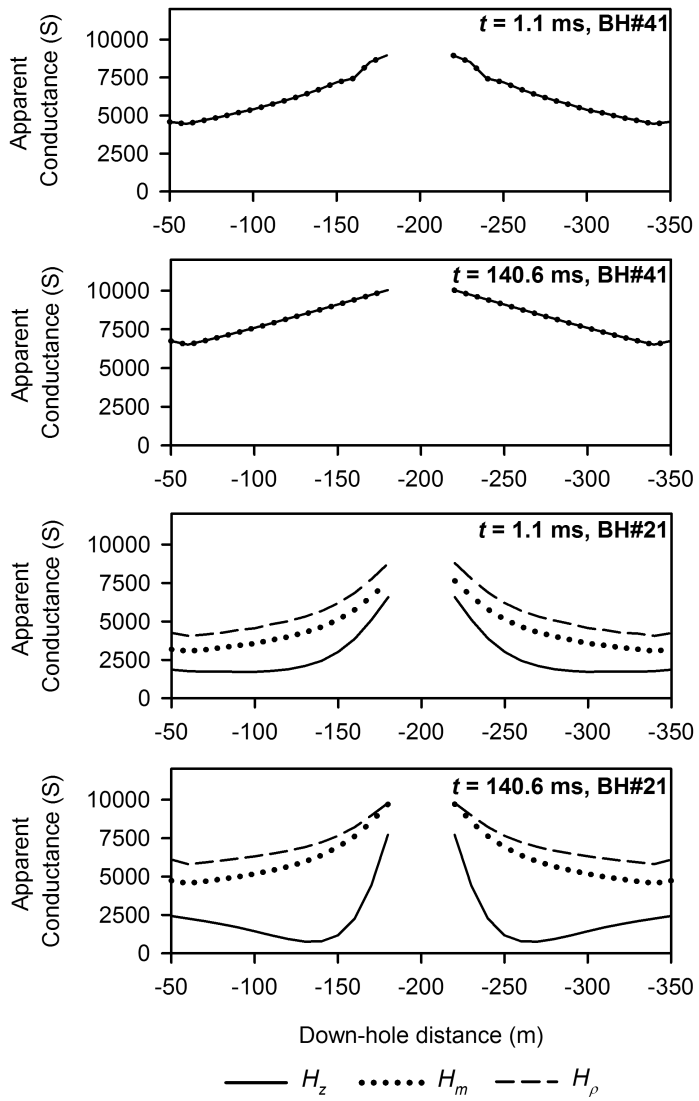

Figure 5-3: Apparent conductance calculated using equation (5-2) using H_z (solid line), H_m (dotted line) and H_ρ (dashed line) at early and late time for the synthetic model shown in Figure 5-2. The sheet is located at -200 m, the conductance of the sheet is 10000 S and BH#41 and BH#21 are the boreholes going through the center and top left corner of the sheet, respectively (Figure 5-2). Time 0 corresponds to the moment of slope change in the UTEM, 100 % duty cycle triangle current waveform. The time windows correspond to the mean middle time of the time windows used. Stations 190 m to 210 m down-hole have been removed due to the high numerical noise close to the sheet.

For the central borehole (BH#41, top two panels, Figure 5-3), the apparent conductance calculated using both the vertical and magnitude components are the same since the magnitude of the field is equal to the vertical field ($H_z >> H_\rho$ thus $H_m \approx H_z$) in this symmetric central-loop configuration (Figure 5-2). In both cases, close to the sheet (-180 m or -220 m), an apparent conductance of 9000 S to 10000 S could be estimated depending on which delay time is used. For the borehole intersecting the top left of the sheet (BH#21, bottom two panels, Figure 5-2), the apparent conductance using different components differs. The vertical component produces erroneous results at the late delay time where the conductance drops off quite rapidly away from the sheet. Nevertheless, an apparent conductance of 6500 S to 7500 S could be estimated. Overall, the apparent conductance from H_ρ is larger and both the apparent conductance calculated using H_ρ and H_m drops off steadily away from the sheet. A reliable apparent conductance of 7500 S to 10000 S could be estimated from either of the two methods. If the methods' assumptions are true (infinite uniform sheet) then all time channels should produce the same calculated conductance and the apparent conductance will be equal to the actual target conductance. However, since the sheet is finite in size and as each time channel corresponds to a current system with a different shape, discrepancies in the calculated apparent conductance can arise because the methods assumptions are violated to a varying extent. Furthermore, differences can also arise from errors in the finite difference approximation used to calculate the temporal and spatial derivatives. In this example, the later delay times produced higher conductance values.

The later delay times produced results closer to the actual conductance, with channel 2 (t = 140.6 ms) providing a good estimate. A gridded map of the apparent conductance from all boreholes at channel 2 at a depth of 180 m can be seen in Figure 5-4. For the vertical component (H_z), there seemed to be an edge effect for stations in close proximity to the sheet edge at a depth of 180 m,

so for these holes, the estimate from a depth of 190 m was used. Similarly, for the horizontal component (H_ρ) there were erroneously high apparent conductance values for the boreholes that did not intersect the sheet and a depth of 160 m for these holes resulted in improved results. These issues were not seen in the estimates obtained using the magnitude (H_m), suggesting this may be a more robust method. In Figure 5-4, H_z produces a relatively diffuse anomaly and the apparent conductance drops off steadily away from the sheet center. The image from H_ρ is less diffuse but it over-estimates the actual conductance over the majority of the sheet and contains some edge effects for the non-intersecting boreholes. The H_m image has all of the sought characteristics: high resolution, minimal boundary effects and a consistent apparent conductance estimate over the majority of the sheet. While each method would likely provide an apparent conductance estimate of about the same order of magnitude, H_m appears to be superior.

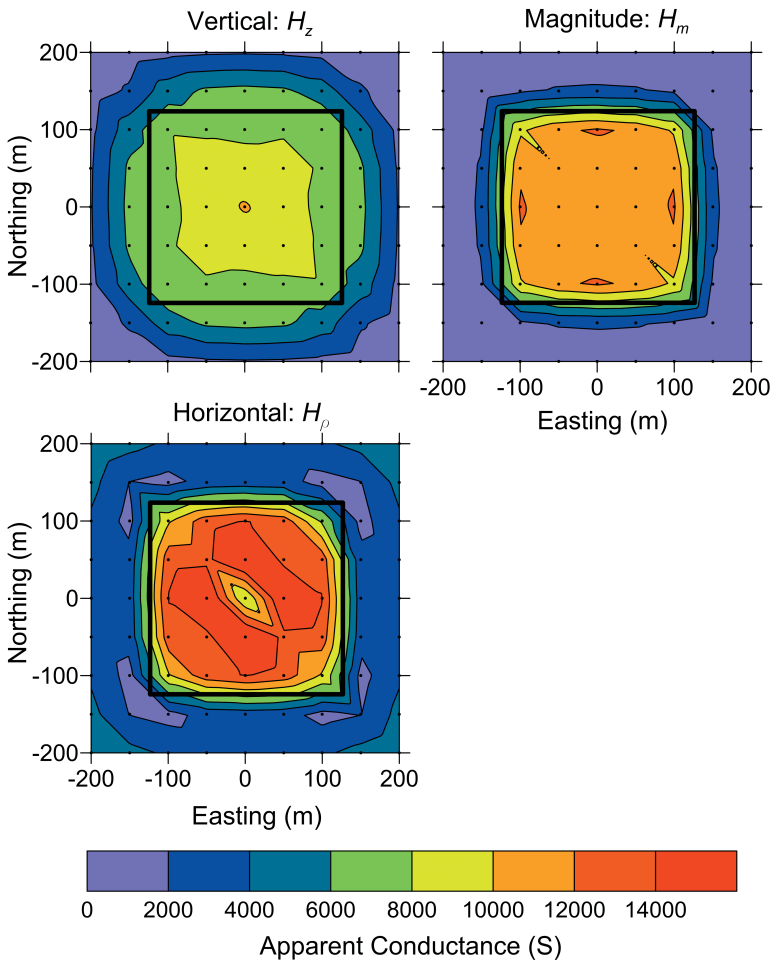

Figure 5-4: Gridded apparent conductance at late time (t = 140.6 ms) using H_z (top left), H_m (top right) and H_ρ (bottom left) corresponding to the survey layout seen in Figure 5-2. Black dots represent borehole locations and the thick black line is the outline of the 10000 S sheet. The image is generated from estimates at a depth of approximately 180 m (see text).

5.4.2 Synthetic Example 2 & 3 – dip of 45°

In the second and third example, the 10000 S sheet is given a dip of 45° (i.e. the boreholes are no longer normal to the sheet). The sheet's dimensions were changed to 350 m by 250 m so that the number of boreholes intersecting the sheet remains the same as in example 1. In example 3, the effect of the transmitter location is investigated by offsetting the transmitter loop 700 m to the east such that none of the boreholes are inside of the loop. Since the boreholes are not normal to the sheet in either example 2 or 3, the spatial gradient (equation (5-7)) is no longer calculated along the normal direction but rather along the borehole axes (vertical in this case; $d\mathbf{H}^s/dz$ is now only an approximation of $d\mathbf{H}^s/dn$). This approximation should hold as long as the distance between stations is small and the secondary magnetic fields are not rapidly varying over that small distance. As the magnitude was the most successful component in the previous example, the calculated apparent conductance using the magnitude on examples 2 and 3 for boreholes #41 and #21 (central and corner hole, respectively) can be seen in Figure 5-5.

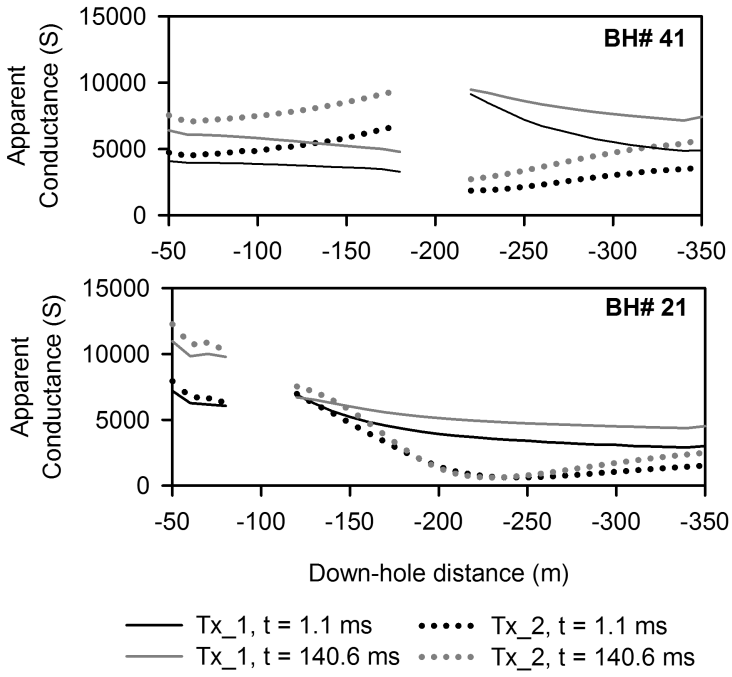

Figure 5-5: Apparent conductance calculated using equation (5-2) using H_m at early and late time for the synthetic model shown in Figure 5-2 (sheet dipping at 45°). In contrast to example 1, the 10000 S sheet has dimensions of 350 m by 250 m, and has a dip of 45°. Tx_1 (example 2) represents the survey being performed inside of the transmitter loop (Figure 5-2) while the transmitter for Tx_2 (example 3) has been offset 700 m to the east. Stations in close proximity to the sheet have been removed.

In contrast to the first example, the magnetic field down the borehole is no longer symmetric about the plane of the sheet due to the non-zero dip. As such, the calculated apparent conductance is also often not symmetric about the sheet and, in some cases, the apparent conductance values and range is smaller on one side of the sheet. Large asymmetry in the apparent conductance generally results from discontinuities in either gradient and/or from

differences in decay rates above and below the sheet. As such, there is some ambiguity as to which apparent conductance values to use, but since they tend to be the same order of magnitude, an average of both sides tended to produce reasonable estimates. As before, the later delay times produce higher apparent conductance estimates. While equation (5-2) for the infinite sheet is independent of the transmitter properties, it is evident that there is some effect on the apparent conductance when the transmitter is offset from a finite sheet (i.e. compare Tx_1 and Tx_2 in Figure 5-5). This difference is more pronounced in BH# 41 but if again the average is taken above and below the sheet, both transmitters produce roughly the same apparent conductance. Using the average above and below, an apparent conductance of roughly 6000 S – 9000 S could be estimated which is close to the actual conductance of 10000 S. As before, all boreholes can be used to produce a contour map of the apparent conductance. A gridded apparent conductance map (channel 2, t = 140.6 ms) was calculated using the average apparent conductance of the station 20 m above and the station 20 m below the maximum H_m value (Figure 5-6). The maximum H_m value was used as this was generally proximal to the location of the sheet (where reliable estimates can be made).

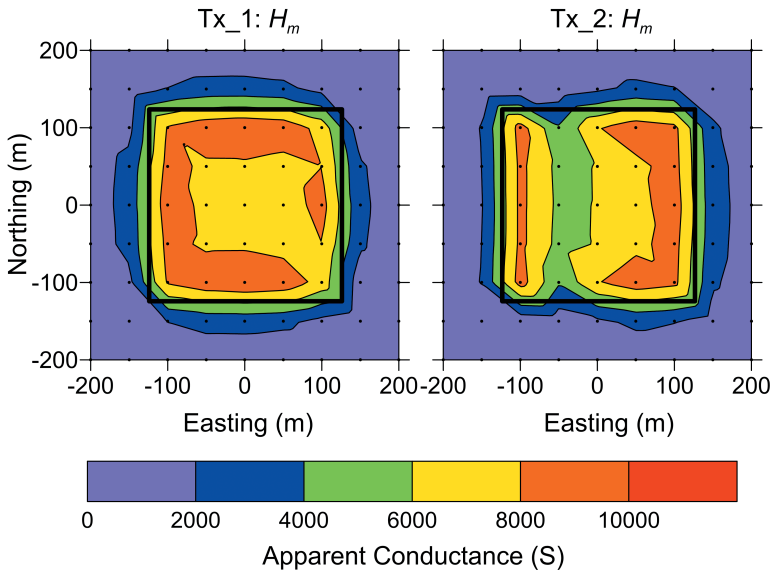

Figure 5-6: Gridded apparent conductance at late time (t = 140.6 ms) using the magnitude (H_m) for a 10000 S sheet with a dip of 45°. For Tx_1 (left panel), the transmitter encompasses the survey area (Figure 5-2) and for Tx_2 (right panel), the transmitter has been offset by 700 m to the east. The conductance values are the average of the conductance estimate 20 m above and below where the magnetic field is the largest.

The results from Figure 5-6 are very similar to that of the apparent conductance calculated using H_m in Figure 5-4. There is a well-defined sheet edge, minimal edge effects and a relatively consistent apparent conductance over the sheet itself. Both transmitter positions essentially produce the same interpreted conductance showing that for a finite sheet the apparent conductance is only weakly dependent of the transmitter position. The apparent conductance (5000 S – 10000 S) is close to the true conductance (10000 S) but is overall a poorer estimate than when the sheet had a zero dip (Figure 5-4). This is likely due to the fact that the derivative is not the derivative in the normal direction, but a derivative in a direction at 45 degrees (i.e.

$dH_m^s/dz \neq dH_m^s/dn$). A reduction by a factor of $\mathbf{1/\sqrt{2}}$ would be expected. The apparent conductance was also calculated using other components (H_z, H_ρ, rotated H_n) and the results were considerably erratic (not shown). Some boreholes would produce apparent conductances close to the true value while others were considerably high or low. Overall, none of them produced results as reliable as using H_m.

5.4.3 Summary and discussion of synthetic modeling

From the three synthetic examples, it is clear that while the theory is developed over infinite uniform sheets, the apparent conductance calculated over finite sized sheets is quite reliable and close to the true conductance when the magnitude (H_m) is used. Using H_m provides the most robust solution as the apparent conductance is reliable regardless of the transmitter position, the location of the borehole within the target and the orientation of the borehole and/or the sheet (i.e. even when $dH_m^s/dz \neq dH_m^s/dn$). Other components produce reliable results intermittently. It should also be mentioned that with real survey data it would likely not be possible to calculate the apparent conductance down the entire hole as depicted in Figures 5-3 and 5-5 due to low signal levels in the spatial gradient ($d\mathbf{H}/dz$). In reality, an adequate signal-to-noise ratio and thus calculated apparent conductance may only be possible where the fields are large (as would be the case in close proximity to the target). Therefore, using the magnitude component has the added benefit that the magnitude of the field will be the largest possible combination of the components and will thus produce the best possible signal-to-noise ratio

5.5 Field Example

The presented methodology for estimating the target conductance can be readily applied on existing borehole data since the method only requires 3-component data which is generally the standard in modern BHEM. As such, two previously surveyed boreholes (4 Hz UTEM survey with a station spacing ranging from 10 m to 15 m, Figure 5-7) in Sudbury, Ontario, Canada are used in this study. The massive sulfide deposits in Sudbury were chosen as ideal targets as they can generally be well approximated by one or more thin sheets/plates which is consistent with the assumptions of the method. The results of equation (5-2) using H_m can be seen in Figures 5-8 and 5-9.

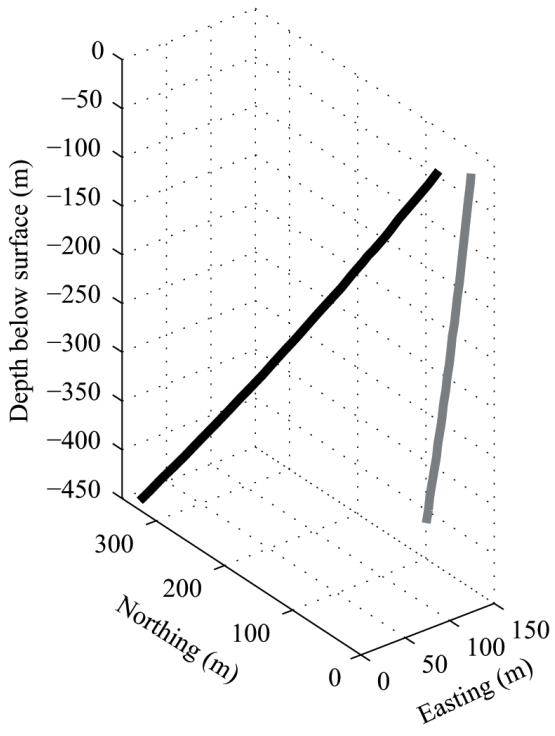

Figure 5-7: Relative location of two UTEM surveyed boreholes intersecting a conductor in Sudbury, Ontario, Canada. Black line: BH# 1. Grey line: BH# 2. The roughly 800 m by 800 m transmitter loop is centered at approximately 900 m N, 50 m E.

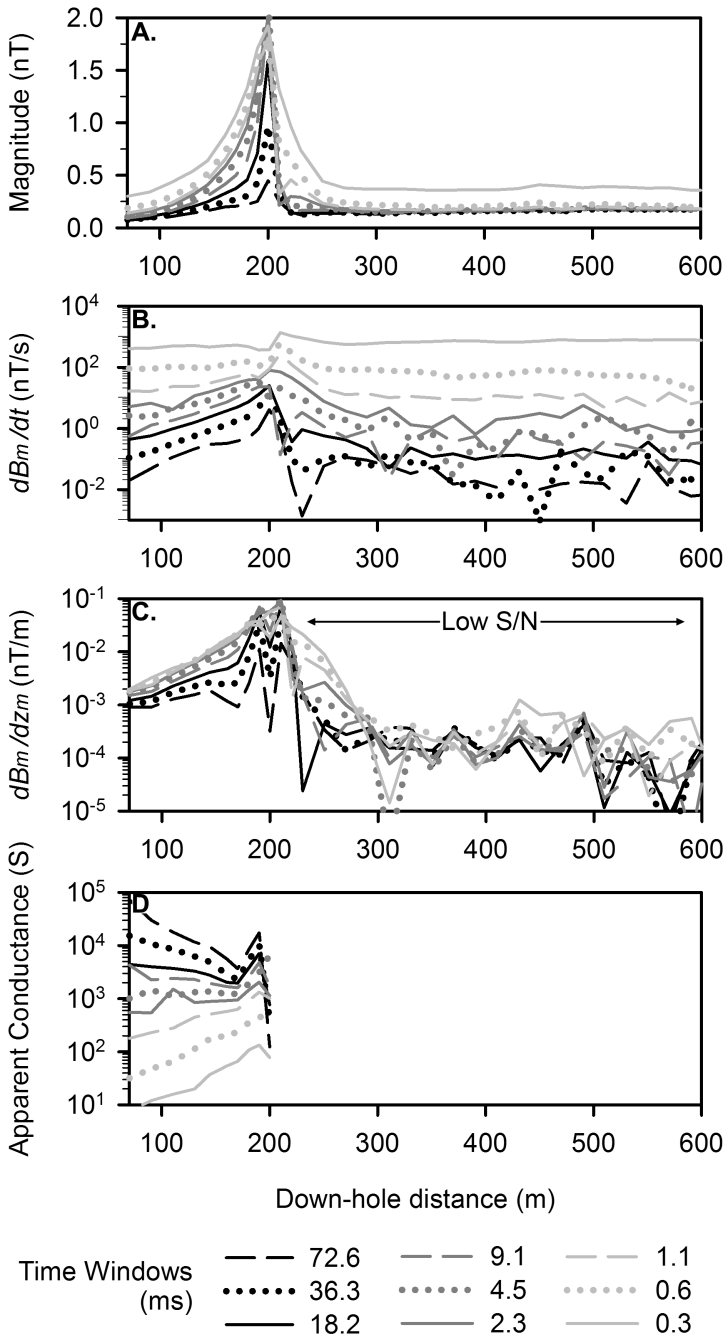

Figure 5-8: Results from a 4 Hz UTEM survey conducted down BH# 1 (Figure 5-7). A. Magnitude of the secondary magnetic field (B_m, theoretical primary removed). B. Absolute magnitude of the temporal derivative (dB_m/dt). C. Absolute magnitude of the spatial gradient (dB_m/dz_m), with area of low signal-to-noise (S/N) ratio indicated. D. Apparent conductance as calculated using equation (5-2) over the acceptable S/N ratio region.

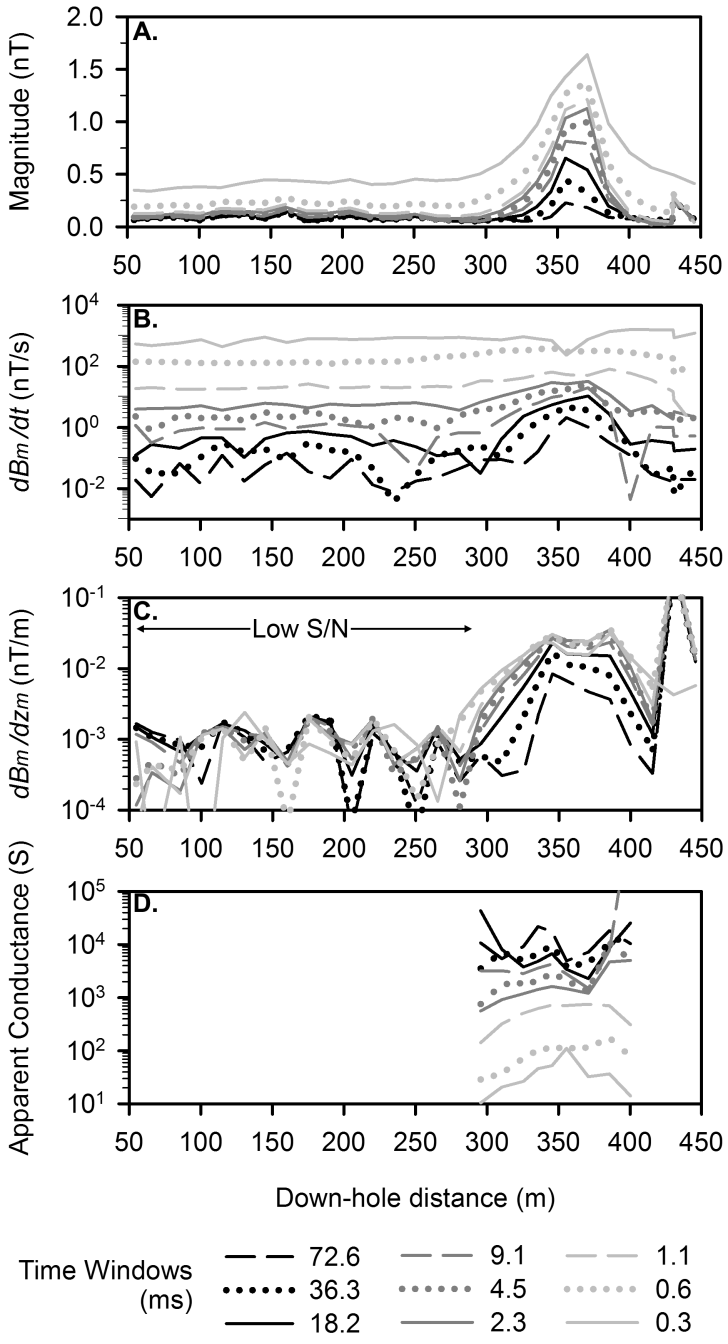

Figure 5-9: Results from a 4 Hz UTEM survey conducted down BH#2 (Figure 5-7). A. Magnitude of the magnetic field (B_m). B. Absolute magnitude of the temporal derivative (dB_m/dt). C. Absolute magnitude of the spatial gradient (dB_m/dz_m), area of low signal-to-noise (S/N) ratio indicated. D. Apparent conductance as calculated using equation (5-2) over the acceptable S/N ratio region.

As before, the magnitude of the field (Figures 5-8A and 5-9A) was calculated from the 3-component data and it is clear that, apart from a roughly 100 m wide zone, the fields are very small over the majority of the hole. The spatial gradient (equation (5-7)) was calculated using the distance down-hole (z_m) rather than the change in depth (z). BH# 2 is essentially vertical and as such, the difference is negligible, while for BH# 1, using the down-hole distance will result in conductance values roughly 10 % - 20 % smaller than using the change in depth. Without knowledge of the strike and dip of the target, it is uncertain which strategy will give a derivative closest to the derivative normal to the plate. The derivatives (dB_m/dz_m and dB_m/dt, Figures 5-8B and 5-9B and Figures 5-9B and 5-9C, respectively) were calculated using the same finite difference scheme as in the synthetic study. Since spatial gradients have very low signal values, dB_m/dz_m is erratic over the majority of the hole due to the low signal-to-noise ratio. As such, the apparent conductance could only be calculated over a small section of the hole where the fields were large (Figures 5-8D and 5-9D, where dB_m/dz_m is above a few pT). This is not much of an issue as the fields are expected to be the largest in the areas of closest proximity to the target and that is also where the apparent conductance (equation (5-2)) is the most reliable. If there were multiple drill holes intersecting the target, then it would be possible to image the apparent conductance variation over the targets in a similar way to the synthetic examples.

For both BH# 1 and BH# 2, most apparent conductance values fall between 1000 S to 10000 S. While the apparent conductance values do span a large range (e.g. 100 S – 8500 S at 180 m for BH#1), the apparent conductance is relatively constant over the depth range at each delay time. For instance, in BH# 2, the field values show large variations from 300 to 400 m depth across the peak in Figure 5-9AC but the apparent conductance values for each delay time are more or less similar across the same depth range. Since the results are consistent, this supports the hypothesis

that the apparent conductance estimates are reliable. The increase in apparent conductance with delay time is consistent with the synthetic data but the range is larger than what was seen in the synthetic study where the apparent conductance generally only varied within the same order of magnitude. It is possible that this discrepancy is due to the invalidation of the methods assumptions (thin sheet, uniform conductivity distribution). Furthermore, with highly conductive bodies, the early time data represents currents which are mainly confined to the surface of the conductor and are only weakly dependent on the conductivity structure (Grant and West, 1965). With increasing delay time, the established currents diffuse into the body and the behavior of the magnetic field will reflect the more conductive parts of the body. This is likely the reason why there is a large change in the apparent conductance from early to late time. For BH# 2, the logarithmic mean apparent conductance over 310 m to 390 m for channels 2 to 4 (36.3 ms to 9.1 ms) ranges from roughly 3400 S to 6400 S. For BH# 1, the range is slightly larger from approximately 2500 S to 6300 S for channels 2 to 4 from 70 m to 190 m. The data from BH# 1 and BH# 2 was also modeled in Maxwell (software by ElectroMagnetic Imaging Technology Pty Ltd) using conductance values of 5400 S and 3000 S, respectively (S. Dickie, personal communication, 2013) which is consistent with our results.

The conductance can also be estimated using the time constant, τ, of the body. The time constant was calculated analytically along the borehole (Nabighian and Macnae, 1991) using

$$\tau = \frac{t_2 - t_1}{\ln[B_m(t_1)/B_m(t_2)]}, \tag{5-8}$$

where t_2 and t_1 are adjacent time channels. The conductance of the target can then be estimated using $C \approx 10\tau/\mu L$ where a value of 50 m was used for L (smallest sheet dimension). The estimate of L was made by visual inspection of the narrow anomaly widths in B_m in Figures 5-8 and 5-9.

Since the time constant can be calculated at all stations and using any adjacent time channels the conductance can be estimated along the entire hole and for each time channel pair as is done with our apparent conductance methodology (equation (5-2)). Overall, the time constant calculated conductance (τ conductance) produced larger conductance values at late delay times but they were generally within the same order of magnitude as our apparent conductance. The logarithmic mean τ conductance ranged from approximately 5000 S to 15000 S for BH#1 and from 3800 S to 9300 S to BH#2 using the same delay times and stations as our apparent conductance estimate. A time constant of roughly 50 ms was calculated using the latest delay time at the peak amplitude in B_m for both holes which results in a τ conductance of roughly 8000 S. These results are consistent with our apparent conductance estimate. However, it should be noted that estimating the conductance using the time constant can be problematic at times. The estimated time constant is only valid once the magnetic field time dependence follows an exponential decay. This occurs at late delay times or far from the source where only the lowest order (smooth, large scale) current system dominates the measured response. At this point, the amplitudes are often small and can be greatly affected by noise. For BH#1 and BH#2, the estimated time constant varied substantially (10 to 100 ms) between adjacent stations and delay times and was likely only valid at the peak B_m position where it ranged from 30 ms to 60 ms at the latest delay times. Furthermore, the estimate of the dimension (L) is often highly dependent on the interpreter skill level and without forward modeling of the response the estimates can vary substantially. While the value for L is typically taken as the smallest sheet dimension, this is not always the ideal dimension. However, perhaps the two methods can be used in conjunction. For instance, if the time constant is taken as 50 ms and the apparent conductance is 5000 S (the average apparent

conductance calculated using equation (5-2)) then the dimension, L, is calculated to be roughly 80 m.

5.6 Conclusion

The conductance of an infinite uniform thin sheet can be calculated from any magnetic field component (or combination of components) by taking the ratio of the spatial derivative in the normal direction with the temporal derivative. Through synthetic modeling we show that by using the magnitude of the magnetic field, reliable estimates of finite sized sheets can also be obtained. This methodology is ideal for BHEM data which typically uses conductance estimation through the laborious process of forward modeling the data or through approximate conductances derived through time constant estimates. In real field data, a limiting factor is the accuracy in which the spatial gradient can be calculated with a finite difference approach between adjacent stations as spatial gradient signals are quite low. However, we show from BHEM data acquired in a massive sulfide example in Sudbury, Ontario, Canada that the spatial gradient is large enough in proximity to the sheet (up to 100 m in this example) and an apparent conductance estimate could be obtained. The estimated value is smaller at early delay times, but as large as 10000 S at later delay times. The apparent conductance values are also consistent with Maxwell models. Calculating the target's apparent conductance from a simple ratio derived from BHEM data is an attractive complement to i) logging the hole with a conductivity probe, ii) traditional inversions, forward modeling and time constant derived conductance values and iii) using handheld instruments or laboratory techniques on the recovered core. Furthermore, the field data suggests that the apparent conductance can be used in conjunction with a calculated

time constant in order to estimate the dimensions of the target. Future research will investigate this possibility further.

5.7 References

Dyck, A. V., 1991, *in* M. N. Nabighian, eds., Electromagnetic methods in applied geophysics, Applications, Part A and B: SEG, Investigations in Geophysics No. 3, Volume **2**, 881–930.

Grant, F. S., and G. F. West, 1965, Interpretation theory in applied geophysics. McGraw-Hill.

King, A., 2007, Review of geophysical technology for Ni-Cu-PGE deposits, *in* B. Milkereit, eds., Proceedings of Exploration 07: Fifth Decennial International Conference on Mineral Exploration, 647-665.

Kolaj, M, and R. S. Smith, 2013, Using spatial derivatives of electromagnetic data to map lateral conductance variations in thin sheet models: Applications over mine tailings ponds: Geophysics, 78, E225-E235.

Lamontagne, Y., 2007, Deep exploration with EM in boreholes, *in* B. Milkereit, eds., Proceedings of Exploration 07: Fifth Decennial International Conference on Mineral Exploration, 401-415.

Lelièvre, P. G., D. W. Oldenburg and N. C. Williams, 2009, Integrating geological and geophysical data through advanced constrained inversions: Exploration Geophysics, **40**, 334–341.

Li, Y. and D. W. Oldenburg, 2000, Incorporating geological dip information into geophysical inversions: Geophysics, **65**, 148-157.

McDowell, G., A. Mackie, and M. Palkovits, 2007, Grade estimation at CVRD Inco's Canadian Sulphide Mines: Symposium on the Application of Geophysics to Engineering and Environmental Problems, 1103-1112.

Nabighian, M. N., and J. C. Macnae, 1991, Time domain electromagnetic prospecting methods, *in* M. N. Nabighian, ed., Electromagnetic methods in applied geophysics, Applications, Part A and B: SEG, Investigations in Geophysics No. 3, Volume **2**, 427–520.

Oldenburg, D. W., and D. A. Pratt, 2007, Deep exploration with EM in boreholes, *in* B. Milkereit, eds., Proceedings of Exploration 07: Fifth Decennial International Conference on Mineral Exploration, 61-95.

Palacky, G. J., 1987, Resistivity characteristics of geological targets, *in* M. N. Nabighian, eds., Electromagnetic methods in applied geophysics, Theory, Investigations in Geophysics Volume **1**, 53-125.

Polzer, B., 2000, The role of BHEM in the Discovery and Definition of the Kelly Lake Ni-Cu Deposit, Sudbury, Canada, 56th Annual International Meeting, SEG, Expanded Abstracts, 1063-1066.

Price, A. T., 1949, The induction of electric currents in non uniform thin sheets and shells: Quarterly Journal of Mechanics and Applied Mathematics, **2**, 283-310.

Smith, R., Shore, M., and D. Rainsford, 2012, How to make better use of physical properties in mineral exploration: The exploration site measurement: The Leading Edge, **31**, 330-337.

Smith, R. S. and A. P. Annan, 2000, Using an induction coil sensor to indirectly measure the B-field response in the bandwidth of the transient electromagnetic method: Geophysics, **65**, 1489-1494.

Telford, W. M., L. P. Geldart, and R. E. Sheriff, 1990, Applied geophysics: Cambridge University Press.

Walker, P., and Y. Lamontagne, 2006, Electromagnetic interpretation in complex geological environments: SEG Technical Program Expanded Abstracts 2006, 1288-1292.

West, G. F., J. C. Macnae, and Y. Lamontagne, 1984, A time-domain EM system measuring the step response of the ground: Geophysics, **49**, 1010–1026.

Zhang, Z., and J. Xiao, 2001, Inversions of surface and borehole data from large-loop transient electromagnetic system over a 1-D earth: Geophysics, **66**, 1090–1096.

Chapter 6

6 A multiple transmitter and receiver electromagnetic system for improved target detection

6.1 Abstract

The work presented here provides an alternative strategy for high-finesse surveys in complex conductor environments where many transmitter-to-target coupling angles are required and for deep focused exploration which will be required where deeper targets are being sought. This strategy involves repeating measurement stations using many smaller sized loops. The multiple transmitter data is then weighted and summed into a single high signal-to-noise (S/N) ratio composite transmitter. The composite transmitter can be thought of as a post-processing method which uses the collected multi-transmitter data to construct/simulate a transmitter which maximizes the coupling to a particular target. The appropriate transmitter weights to use will depend on the target location and geometry and, as such, different weighting schemes allow for the construction of different composite transmitters, each of which will maximally highlight different targets. In this work, we assume no prior knowledge of the location and orientation of the exploration targets and construct composite transmitters for each possible location of a discretized subsurface and 324 possible target orientations (dipole embedded within a fully resistive medium). A modified difference of squares and a dipole table look-up is used to assess the fit between each composite transmitter and the suggested target location and orientation. Synthetic studies using conductive plate target(s) embedded within a fully resistive medium

show that the target locations and orientations could be accurately determined and that the S/N ratio of the composite transmitter was significantly higher than that of a standard fixed-loop ground and airborne survey. In a ground time-domain EM field test, 23 transmitter positions were used and a shallow target (conductive dyke) could be identified using the developed methodology. The composite transmitter data we produced was considerably easier to interpret and had a larger amplitude than that of any one single transmitter.

6.2 Introduction

With the continual depletion of mineral resources, exploration for deeper ore bodies will be essential in sustaining current mine production levels and future demand for resources. The electromagnetic (EM) geophysical prospecting technique is widely used in the exploration for mineral resources as the exploration targets (i.e. the deposit itself, and/or the host structures) are often moderately to highly conductive relative to the background medium. However, from an EM geophysical exploration point of view, deeper ore bodies present technical challenges as the measured responses from these deep ore bodies are small and often below background noise levels (poor signal-to-noise, S/N, ratio). The main strategy to overcome this issue has been to use large high powered transmitters with large magnetic moments (Zhdanov, 2010). These high moment transmitters increase the S/N ratio of deeper ore bodies by producing larger magnetic fields at greater depths (Nabighian and Macnae, 1991). However, the logistical issues associated with using transmitter wire loops several kilometers in length and transmitter current generators that are very large and cumbersome are often costly and impractical (Zhdanov, 2010). Furthermore, since the drop-off rate of the magnetic field amplitude of a large transmitter loop approaches an inverse cube relation far from the loop (the distance at which this occurs is

proportional to the transmitter size), the transmitter moment has to be increased tremendously to have a noticeable impact on the depth of exploration. As an example, increasing the transmitter moment by a factor of two by either doubling the transmitter loop area or the transmitted current would only increase the depth of exploration by roughly 25%.

Moreover, if the transmitter loop is not positioned properly such that the magnetic field generated by the transmitter (termed the primary magnetic field, $\mathbf{H}^P$) does not couple well with the target (i.e. does not crosscut the target), then the amount of induced current within that body will be greatly reduced (Faraday's Law) and the resultant magnetic field (termed the secondary magnetic field, $\mathbf{H}^S$) generated by those induced currents (via Ampere's Law) may be small enough to be undetectable (i.e. low S/N ratio). It is thus common practice to move the transmitter loop to one or more other locations in an attempt to vary the transmitter-to-target coupling. Moving large transmitter loops is logistically challenging (Nabighian and Macnae, 1991), and, without prior knowledge of the target position, choosing the optimal transmitter location is difficult. In airborne EM, the coupling issue is less prevalent due to the moving transmitter loop but the size of the transmitter, and thus the depth of penetration of the system, is limited as the transmitter moment is restricted by the size and power of the aircraft (Palacky and West, 1991). In both the ground and airborne situation, longer recording times are preferable as the waveform stacking process increases the S/N ratio. However, a longer stacking time results in decreased production in ground surveys (Zhdanov, 2010) and is limited by the speed of the aircraft in airborne surveys.

An alternative strategy, presented in Lymburner and Smith (2015), which aims to address the issues of depth of penetration and coupling for the exploration of deeper ore bodies, is to repeat the profile or grid with many, potentially smaller, transmitters. In fact, the response of any

traditional large transmitter could be represented by a sum of smaller moment dipole transmitters. A comparison between the primary magnetic field of a large 2 km by 2 km loop and that of a sum of equally spaced dipole transmitters can be seen in Figure 6-1. While many dipole transmitters were required to fit the small offset data, the number required is greatly reduced for offsets larger than a few hundred meters (typical loop-station or loop-target offets).

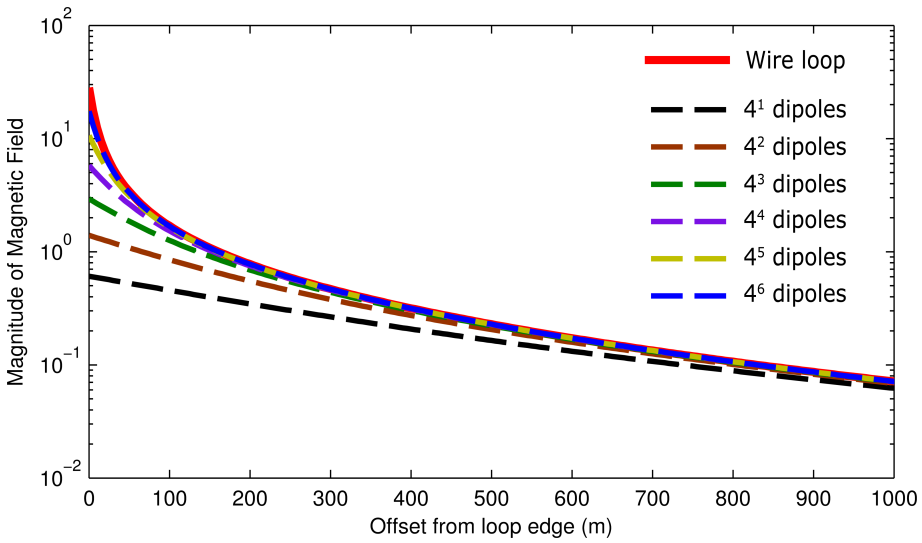

Figure 6-1: Magnitude of the magnetic field from a 2 km by 2 km wire loop (unit current) and that of equally spaced dipoles within the loop. The profile begins 5 m from the center of the eastern side of the wire loop. The dipole moment of each dipole transmitter is equal to the moment of the large loop divided by the total number of dipole transmitters.

In typical EM data processing when multiple transmitter locations are used, the responses are generally not combined as in Figure 6-1. Each transmitter will couple differently to the target(s), may possess different information and will have a different S/N ratio. As such, the multiple

transmitter data are generally interpreted semi-independently with the goal in mind of producing one model which fits all available data. However, when a large number of transmitters are used (tens to hundreds) interpreting each transmitter is not efficient and/or feasible in a reasonable amount of time. Since the EM problem is linear with respect to the source excitation, we can combine the measurements from each transmitter into a single measurement which represents the EM response to a large moment "composite transmitter" (as in Figure 6-1). If many transmitters are used then many composite transmitters can be constructed which provide a superior variety of transmitter-to-target coupling than a few of the traditional large loops. Further, if enough small high-powered transmitters can be combined to give a larger total moment than the traditional loops, then there is potential for deeper exploration. As many small transmitters may be required to produce equivalent large-loop magnetic fields at typical exploration depths, the optimum way (logistically speaking) to collect multi-transmitter data may be with a hybrid ground/airborne system. In the hybrid configuration, an array of ground receivers can be laid out and then an airborne transmitter is flown over-top.

After data collection, the ideal manner in which the multiple transmitter data is combined into one large composite transmitter will depend on the location and orientation of the target(s) as each single transmitter will couple to the target(s) differently. Thus, the multiple transmitter data can be summed into different composite transmitters, each of which highlights different targets by maximizing the coupling between the composite transmitter and the target. Similar processing techniques and multi-fold transmitter-receiver arrays for deep multi-conductor exploration have been discussed in Polzer et al. (1989), Powell (1990) and Powell et al., (2007). The critical difference between the previous methods and the one discussed in this paper is the move from roughly 3 transmitter positions to 10s or even 100s of positions. Multiple transmitter and receiver

systems have also been used in the detection and characterization of unexplained ordinances whereby an array of multi-axis transmitters and receivers was found to provide superior location and property information (Snyder and Oden, 2002). These systems typically include one or several single axis (typically *z*-directed) or 3-orthogonal component transmitters and an array of receivers (single *z*–axis or 3-orthogonal component) mounted on a small rigid moveable platform.

We begin by discussing the multiple transmitter data summation process and how it can increase the S/N ratio, by ensuring adequate coupling, compared with traditional methods. With synthetic studies, we present a simple imaging procedure which can identify the depth and orientation of the target(s) and the appropriate composite transmitter(s) which maximizes the S/N ratio for the identified target(s). The first synthetic example showcases the potential of the hybrid airborne/ground surveying method to efficiently collect multiple transmitter data (256 transmitter positions) while the second example shows a downscaled ground surveying example with 81 transmitter positions. Lastly, the presented method is also successfully tested on the multiple transmitter EM data of Lymburner and Smith (2015) which was collected over a shallow conductor on Wallbridge Mining property in the East range of the Sudbury Basin in Ontario, Canada.

6.3 Methodology

The goal of the method presented here is to sum the different transmitter responses in such a way so as to maximally enhance the response from a certain target. One way of summing the transmitters it to apply weights that are proportional to how well the transmitters coupled to the

target (Lymburner and Smith, 2015). In order to efficiently calculate the coupling between the transmitter and the target, we use a dipole approximation for both the transmitter and the target,

$$C(\mathbf{r}_t, \mathbf{r}_d, \mathbf{m}_\theta) = \frac{M_t}{4\pi|\mathbf{r}_t - \mathbf{r}_d|^3}\left[\frac{3\mathbf{m}_\theta \cdot (\mathbf{r}_t - \mathbf{r}_d)}{|(\mathbf{r}_t - \mathbf{r}_d)|^2}(r_t - r_d) - m_\theta\right], \quad (6\text{-}1)$$

where C is the coupling coefficient between a transmitter located at $\mathbf{r}_t$ of dipole moment M_t (effective area multiplied by the transmitted current) and a dipole target of orientation $\mathbf{m}_\theta$ (unit vector normal to the planar target) located at $\mathbf{r}_d$. The symbol $|\,|$ represents the magnitude of the enclosed vector. Since the dipole formula (equation (6-1)) is typically expressed as a vector equation, we set the variables, r_t, r_d and m_θ, to represent the component of $\mathbf{r}_t$, $\mathbf{r}_d$ and $\mathbf{m}_\theta$, respectively, parallel to the axis of the transmitter such that equation (6-1) results in a scalar value (i.e. the coupling coefficient between the dipole transmitter and target). When multiple transmitters are present, C is generally divided by the maximum value (maximum coupled transmitter) in order to be a dimensionless scalar ranging from ± 1 (termed the normalized coupling coefficient). As the method approximates the target with that of an equivalent dipole, it is only valid for discrete targets. Non-dipole transmitters could also be used whereby equation (6-1) would need to be replaced with the appropriate formula for the particular transmitter geometry (i.e. for an arbitrary transmitter wire loop, the coupling coefficient could be calculated by using the Biot-Savart Law to calculate the component of the magnetic field normal to the target at the targets location).

Figure 6-2 displays the normalized coupling coefficient, C, for vertical dipole transmitters (spaced 50 m apart) and a target with varying dip located in the center of the profile at a depth of 500 m. The normalized coefficients seen on the y-axes are the weighting factors applied to the

corresponding data associated with the transmitter at that location. This ensures that the data associated with transmitters that coupled well to the target (high S/N ratio) are enhanced and those that did not couple well (low S/N ratio) are reduced. However, the weights vary for different target locations and orientations, and as such, the target orientation and location must be known, estimated, or assumed in order to apply the appropriate weights so as to enhance the response. For example, for a vertical target (Figure 6-2, solid line), the transmitters located at -250 m and 250 m would be weighted the highest (weights of -1 and +1, respectively). However, if the dip of the target was 30 degrees then those same transmitter positions should have weights of 0.24 and 0.71 (Figure 6-2, dash-dot line). Throughout this work, the convention for orientation (strike and dip) is on a [0°, 180°) interval, whereby a 0° or 90° strike would imply a north-south or east-west trending feature, respectively. The dip angle is measured from the east facing side of the target (with the exception of a 90° strike whereby it is measured from the south).

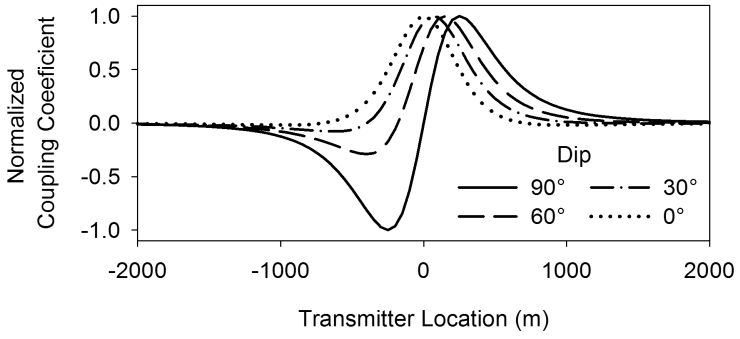

Figure 6-2: Normalized coupling coefficient as calculated using equation (6-1) between a vertical dipole transmitter and a dipole target of varying dip located in the center of the profile at a depth of 500 m.

The proposed method is to *assume* every possible target location (r_d) and orientation (m_θ), and to sum the multiple transmitter data for each assumed location/orientation using the appropriate dipole coupling coefficients (C, equation (6-1)). When the assumed location and orientation matches the actual location and orientation of the target, the summed data will maximally reinforce the signal from that particular target. The weighted sum of the transmitters will form an equivalent composite transmitter which will be the optimal summed multiple transmitter (enhanced S/N ratio) for that particular target. This can be assessed quantitatively by a comparison of the shape of the profile with the shape from a theoretical body at that location (dipole table look-up). In this paper, the fit is determined using a modification of the difference of squares method from Smith and Salem (2007),

$$I_{(\mathrm{r}_{\boldsymbol{d}},\mathrm{m}_{\boldsymbol{\theta}})} = \left\{1 - \frac{\sum\left[\left(\mathbf{H}^S\mathbf{C}_{(\mathrm{r}_d,\mathrm{m}_\theta)}\right) - \mathbf{L}_{(\mathrm{r}_d,\mathrm{m}_\theta)}\right]^2}{\sum\left[\mathbf{L}_{(\mathrm{r}_d,\mathrm{m}_\theta)}\right]^2}\right\}^2, \tag{6-2}$$

where I is the degree of fit, $\mathbf{H}^S$ is a matrix of the survey data (time derivative or magnetic field measurements) where each row represents a different station location (at a particular frequency or time channel) and each column represents a different transmitter location, $\mathbf{C}$ is the vector of coupling coefficients calculated for each transmitter position, and $\mathbf{L}$ is the corresponding look-up data for a dipole of orientation $\mathbf{m}_\theta$ located at $\mathbf{r}_d$ for the same station locations as $\mathbf{H}^S$. The dipole look-up data ($\mathbf{L}$) is calculated using the dipole equation (Telford et al., 1995) for a fixed number of subsurface locations and dipole orientations. In this work, the orientation (strike and dip of the dipole) varied from 0° to 170° in 10° intervals (324 possible dipole orientations) and the discretized subsurface cell size (i.e. location of the dipoles) varied from example to example. As

the discretization (for both the orientation and subsurface) is made finer, the data fit is generally improved but there is an increase in computation time. Note that each column of $\mathbf{H}^S$, and $\mathbf{C}$ and $\mathbf{L}$ are normalized to unit amplitudes. I is set to zero when negative and when multiple EM component data are available, I is the product of the fit for each of the measured components (i.e. for 3-component EM data, $I = I_x I_y I_z$). When the fit, I, is close to unity, there is a high likelihood that there is a target at that $\mathbf{r}_d$ with orientation $\mathbf{m}_\theta$. Equation (6-2) is solved by finding the maximum I values over a discretized subsurface ($\mathbf{r}_d$) with dipoles of varying orientations ($\mathbf{m}_\theta$). From this, an image section (or volume) of the most likely dipole locations and orientations ($\mathbf{r}_d$ and $\mathbf{m}_\theta$ values) which fits the data can be produced. Alternatively, equation (6-2) could be inverted to find the location and orientation that give maximum I values.

In practice, I is calculated over a variable window size so as to not degrade the fit value due to areas distant from the target which will likely have low S/N ratios. A variable window size is also necessary when multiple targets are present so as to fit multiple dipoles in lieu of a single dipole for the entire survey area. The window size is the distance from the peak amplitude of the look-up table data to the minimum distance which encompasses a user defined percentage (relative term, α) of the total sum of the look-up table data (the magnitude of the look-up data is used when multiple components are being used to calculate equation (6-2)). The window size is calculated for each look-up table target/dipole. Since the footprint (lateral extent of the fields emanating from the target) increases as the target becomes deeper, the window size would similarly increase.

Once the target locations and orientations are known, the appropriate coupling coefficient vector, $\mathbf{C}$, can be selected. The multi-transmitter data can then be summed (via $\mathbf{H}^S\mathbf{C}$) to form the optimal composite transmitter which provides the maximum S/N ratio for the identified target(s). Note

that when multiple targets are present, there will be an optimal composite transmitter for each target (different **C**).

6.4 Synthetic Examples

Since the imaging and transmitter summation algorithm (equation (6-2)) is general and includes no time/frequency variable, frequency domain surveys were simulated for computational simplicity and only the quadrature component was considered. The synthetic examples were generated in GeoTutor (PeTros EiKon) using the VHPlate algorithm (Walker and West, 1991) for conductive plates embedded in a completely resistive host.

6.4.1 Example 1 – Hybrid Ground/Air Survey

The described survey methodology and logistics (i.e. repeating profiles with multiple transmitter positions) is best exploited with a hybrid airborne/ground EM system. With a typical airborne EM transmitter and a distributed ground receiver array system the survey time is drastically reduced as compared to performing the survey using many ground loop positions and a single roving receiver. A single frequency domain (100 Hz), 2 million Am^2 dipole moment airborne transmitter at a height of 120 m with ground receiver stations (3-component) spaced every 100 m along a 3 km by 3 km grid is simulated. Dipole moments of 2 million Am^2 are typical for airborne systems, e.g. MEGATEM 2,100,000 Am^2 (Smith et al., 2003), HELITEM 2,000,000 Am^2, and VTEM 2,500,000 Am^2 (Smith and Volkovitsky, 2014). Due to computational limits, the transmitter locations are spaced every 200 m, resulting in a net total of 256 transmitters each with 961 3-component magnetic field recordings. The top center of a 100 S plate is located at (0, 0, -500 m). The plate has a strike and dip of 40° and 30°, respectively, and has a strike length and

down dip length of 300 m and 150 m, respectively. In addition to the hybrid airborne/ground survey, two other single frequency domain surveys (100 Hz) were simulated for comparison purposes: a large horizontal 20 A, 3 km by 1.5 km fixed-loop ground survey (100 million Am^2 equivalent dipole moment transmitter and a roving 3-component receiver) and an airborne survey (3-compoonent receiver is towed 130 m behind and 50 m below the 2 million Am^2 airborne transmitter). An aerial view of the survey geometry can be seen in Figure 6-3. Gaussian noise was added to the synthetic survey data but since multiple acquisition systems were simulated (ground, airborne, semi-airborne) different noise values were used. Following the results of Smith et al. (2001), we assigned the highest noise level (0.1 pT) for the airborne system. A noise level 40 % of the airborne system was assigned for the fixed-loop ground survey (0.04 pT) and since the hybrid air-ground system is a mixture of both survey types (ground and air), we assigned it a noise value in between the other two systems (0.07 pT). The window size for the dipole table look-up is the same size as the survey area (i.e. α = 100 %; the dipole look-up table comparison in equation (6-2) is performed over the entire survey area).

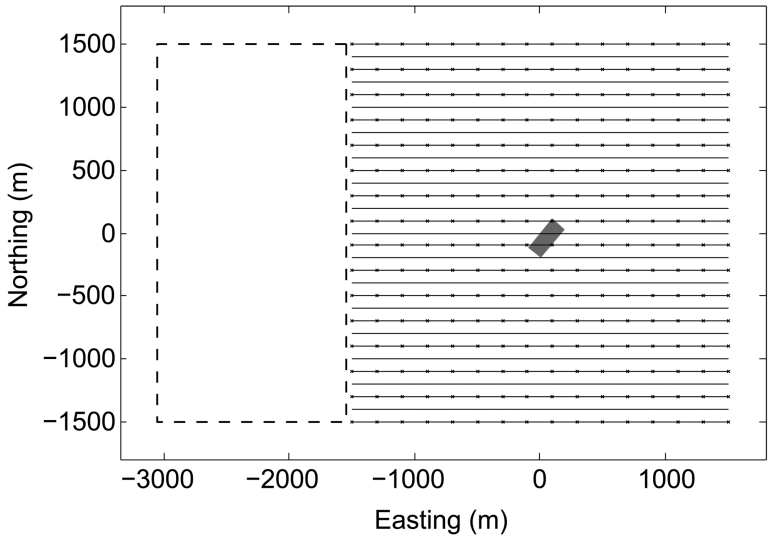

Figure 6-3: Plan view of the survey geometry used in the first synthetic example. Black solid lines indicate the locations of the 3-component receivers (spaced 100 m apart) on a 3 km by 3 km grid. An 'x' indicates the locations of the airborne transmitter and the dashed black line indicates the location of the ground transmitter loop. The 300 m by 150 m plate, shown in grey, is buried 500 m below surface.

For computational efficiency, the imaging algorithm (equation (6-2)) was first run at a coarse discretization over the entire survey area and for a large depth range. Once the general location of the suspected target was found, it was re-run at a finer discretization to produce Figure 6-4 (25 m by 25 m by 50 m cell size). In Figure 6-4, the locations correspond to $\mathbf{r}_d$, the color saturation corresponds to the fit value, I, scaled to be between 0 and 1, and the hue corresponds to the most likely dip (left panels) or strike (right panels) of the target (derived from $\mathbf{m}_\theta$). When I was less than 0.5, the color was set to white. The strike and dip were both discretized from 0° to 170° in 10° intervals. A strike of 0° corresponds to a north-south target, while a strike of 90° would

correspond to an east-west striking target. A dip less than 90° implies the structure is dipping towards the east, while a dip greater than 90° implies a dip towards the west.

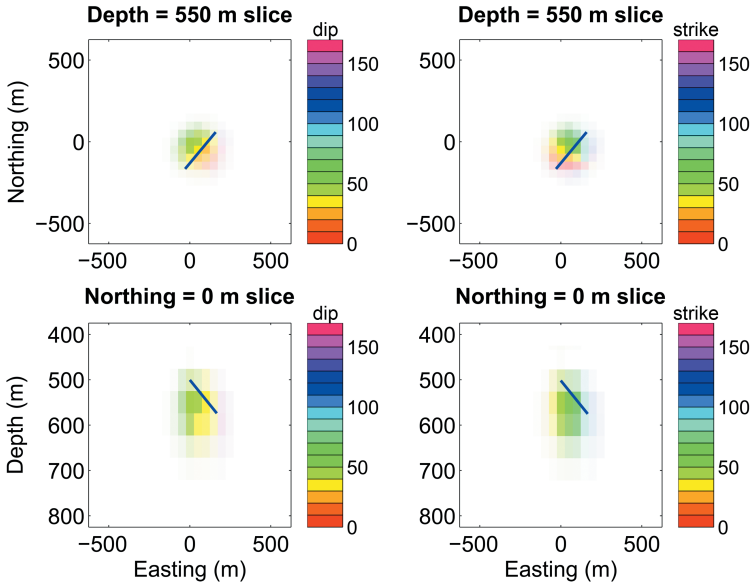

Figure 6-4: Horizontal slice plan view at depth = 550 m (top row) and vertical slice section view at northing = 0 m (bottom row) with the dip (left column) and strike (right column) calculated using equation (6-2). The dark blue line corresponds to the location of the plate target (intersection of the plate and the slice plane). The cell size is 25 m by 25 m by 50 m.

As can be seen in Figure 6-4, the estimated location of the plate matches the actual location. The majority of the *I* values greater than 0.5 ranged from 20° to 60° for the strike, and, from 30° to 60° for the dip. The fit which produced the maximum *I* value corresponded to a dipole located at (50 m, -50 m, 550 m) with a strike and dip of 40° and 30°, respectively. For reference, the center point of the actual plate was located at (50 m, -42 m, 538 m). The excellent degree of fit can be

explained via Figure 6-5 which depicts the response of the large plate and that of the best-fitting dipole. It is clear that the dipole model is an adequate approximation for this plate target and that equation (6-2) can recover a dipole model which explains the measured data.

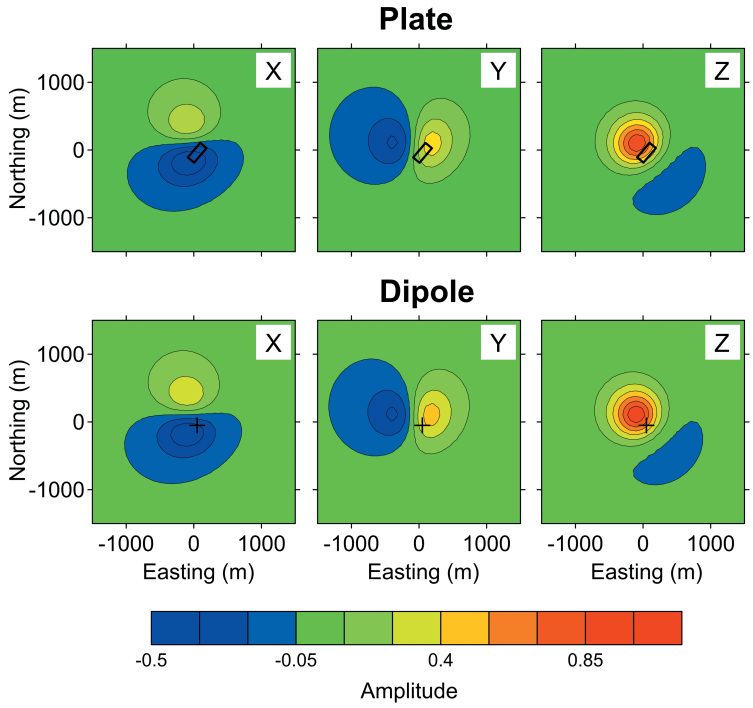

Figure 6-5: Plan view comparison of the 3-component magnetic field ($\mathbf{H}^s$) synthetic plate data (well coupled transmitter, no noise is present, plate location shown with a black rectangle) and best fitting dipole model for the same transmitter (dipole location shown with a '+'). Data from both models was normalized by the maximum value.

As the location and orientation of the target can now be estimated (maximum *I* value), the multiple transmitter data can be summed ($\mathbf{H}^S\mathbf{C}$, equation (6-2)) to form a composite transmitter. By summing the single transmitter data using weights calculated based on the coupling between the target and the transmitters, the response from that target will be maximally enhanced. This

particular composite transmitter will be considered optimal for the target located at (50 m, -50 m, 550 m) with a strike and dip of 40° and 30°, respectively. A comparison of the data from the optimal composite transmitter, the fixed-loop ground and the airborne survey data using the survey geometry from Figure 6-3 can be seen in Figure 6-6. Note the amplitude of the composite transmitter is roughly thirteen times larger than that of the fixed-loop ground and the airborne surveys (Figure 6-6, top panel). The S/N ratios for the composite transmitter, fixed-loop ground survey and airborne survey are 64, 24 and 11, respectively. Furthermore, with typical aircraft speeds, the equivalent transmitter spacing could be as low as roughly 15 m (as opposed to 200 m which is used in this example) which would have resulted in 24 times the number of transmitter locations. Even by using a higher estimate for noise (airborne survey noise level of 0.1 pT) this would have resulted in a S/N ratio of approximately 220 for the composite transmitter of the hybrid survey.

The relative comparison between the S/N ratios of the different systems is not only dependent on the selected transmitter moments and target-to-transmitter coupling but also on the pre-selected post-stack noise values. An important factor is the consideration of stacking time (i.e. how long each station is occupied). In this example, it was assumed that for the ground loop example, a typical stacking time was used (i.e. on the order of 30 seconds to a few minutes) whereas for the airborne cases, the stacking time is controlled by the aircraft speed. Moreover, in the fixed-loop ground system, if the loop is moved to a different location, the coupling between the transmitter and the target will change and this may either increase or decrease the amplitude of the response and the resulting S/N ratio. As a direct result, the survey will be biased towards targets/features which coupled well to the transmitter. With a multi-transmitter survey, the potential combinations in which the composite transmitter can be constructed significantly removes this

bias as no features/targets will be in a null-coupled geometry. As such, even if the S/N ratio of the hybrid survey's composite transmitter was not superior to that of the ground fixed-loop survey (i.e. ideal loop-placement and long stacking time for the ground survey), it may still be preferable to use hybrid surveying so as to ensure adequate coupling to all possible target locations. Moreover, if multiple complex conductors were present, the ground fixed-loop survey will be biased towards the conductor with which it had the highest coupling. In some cases, other conductors may be not be distinguishable at all due to poor coupling and/or due to being shielded by better coupled conductors. By collecting multiple-transmitter data, many different transmitter-to-target coupling values are available and the probability of missing a conductor (or being able to discern its attributes) is reduced.

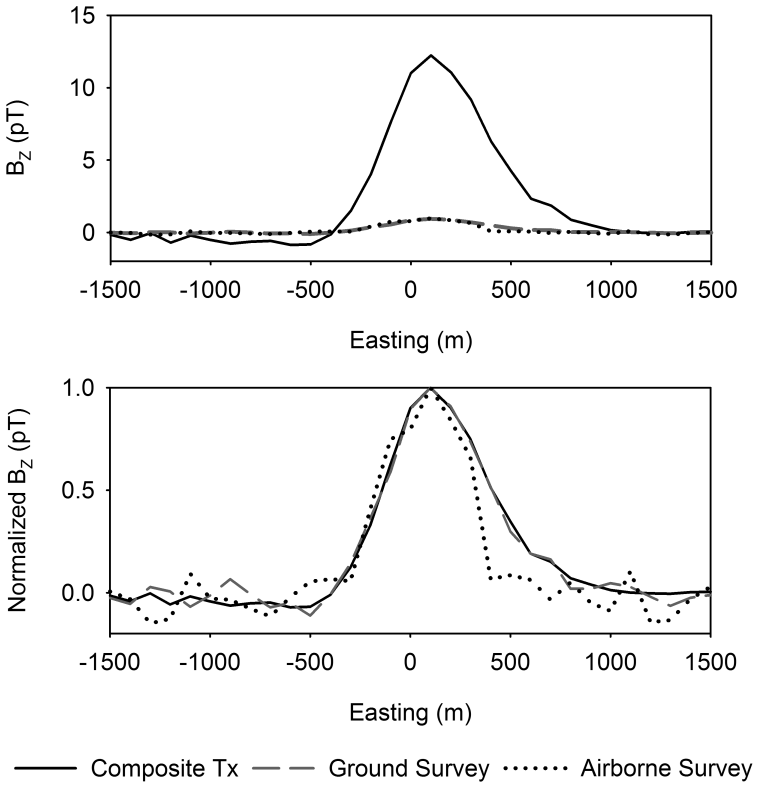

Figure 6-6: Comparison of the center line (Northing = 0 m) of the summed composite transmitter (solid black line), fixed-loop ground survey (dashed grey line) and the airborne survey (dotted black line). Top panel: Comparison of the amplitudes of the responses. Bottom panel: Data from each system normalized to a maximum signal of 1 so that the relative noise can be seen in the background.

6.4.2 Example 2 – Multiple Target Ground Survey

In the second example, a single line survey with 81 ground stations and transmitters (100 Hz operating frequency and 10^6 Am^2 moment dipole transmitters) on a 4 km line was simulated. Two 300 m (strike length) by 150 m (dip length) plate targets were used. Plate 1 was centered at (-700 m, 0 m -175 m) with a strike and dip of 45° and 90°, respectively, and plate 2 was centered

at (746 m, 46 m, -188 m) with a strike and dip of 135° and 30°, respectively. A view of the survey geometry can be seen in Figure 6-7.

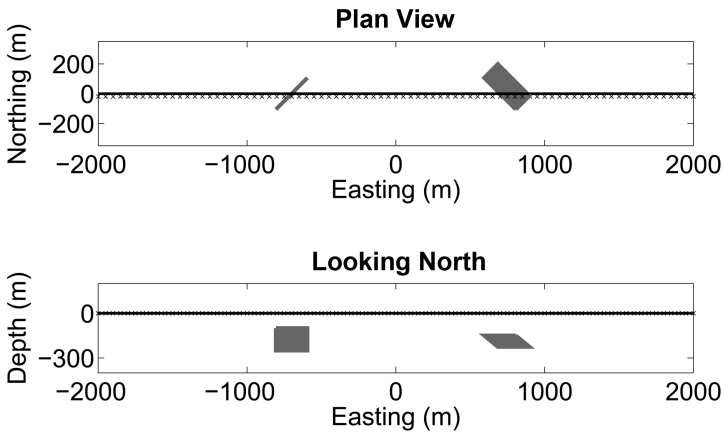

Figure 6-7: Plan view of the survey geometry (top) and side view (bottom) used in the second synthetic example. The black solid line indicates the surveyed profile of the 3-component receivers (spaced 50 m apart, 4 km line). An 'x' indicates the location of the ground dipole transmitter (spaced 50 m apart, 20 m south of the receiver line). The two 300 m by 150 m plates projected onto the plan and section are shown in grey

Figure 6-8 was generated using equation (6-2) with a 25m by 25 m by 25 m cell size. An α of 80 % was used in order to avoid cross contamination of the signals from the two targets when performing the dipole table look-up comparison. Recall that an α value below 100% implies that the dipole table look-up is not performed using all receiver/station locations but rather using only stations which encompass the majority of signal (80% in this case) of the particular look-up dipole. The two resolved targets are best fit with dipoles located at (-700 m, 0 m, 175 m) with a

strike and dip of 40° and 90°, respectively, and at (750 m, 0 m, -200 m) with a strike and dip of 140° and 40°, respectively. The best fitting dipoles match well with the actual locations and orientations of the plates. As in Example 1, once the location and orientation of the target is known, the optimal composite transmitter can be constructed via $\mathbf{H}^{S}\mathbf{C}$ where **C** contains the transmitter-to-target coupling factors for the identified targets. Since there were two targets identified in this example, there will be two different coupling vectors (i.e. two composite transmitters). Many of the transmitter positions coupled well to both targets and, as such, the measured magnetic field data detects both deposits (Figure 6-9, top panel). However, by using the optimal composite transmitters both targets can be separated into their individual responses (Figure 6-9, middle and bottom panels). Two of the most strongly coupling single transmitter response profiles that couple weakly to the other conductor were manually selected for comparison and are shown in Figure 6-9 (dashed lines). Note that the composite transmitters provide significantly larger response amplitudes than the strongly coupled single transmitters. Furthermore, the likelihood of manually positioning the single transmitters in the ideal locations is unrealistic unless the targets are already well understood.

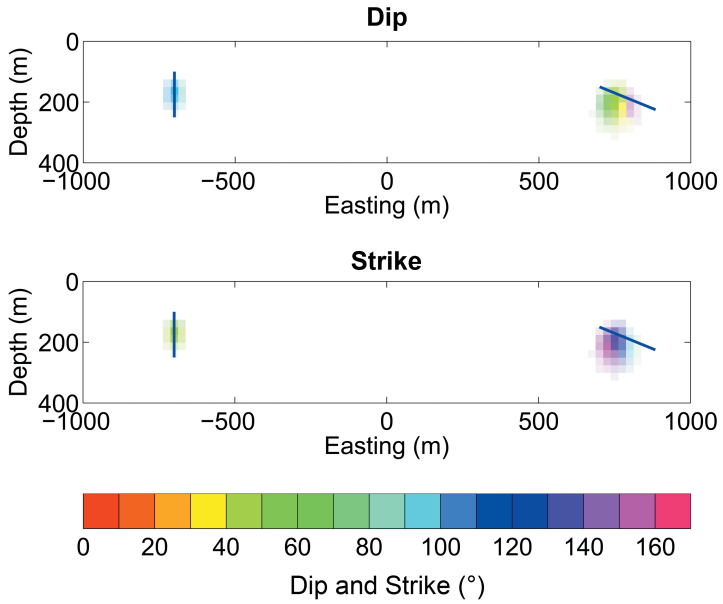

Figure 6-8: Equation (6-2) calculated for the two-plate synthetic survey depicted in Figure 6-7. The northing is equal to 0 m across the profiles. The dark blue lines correspond to the intersection of the two plate targets and the section. The cell size is 25 m by 25 m.

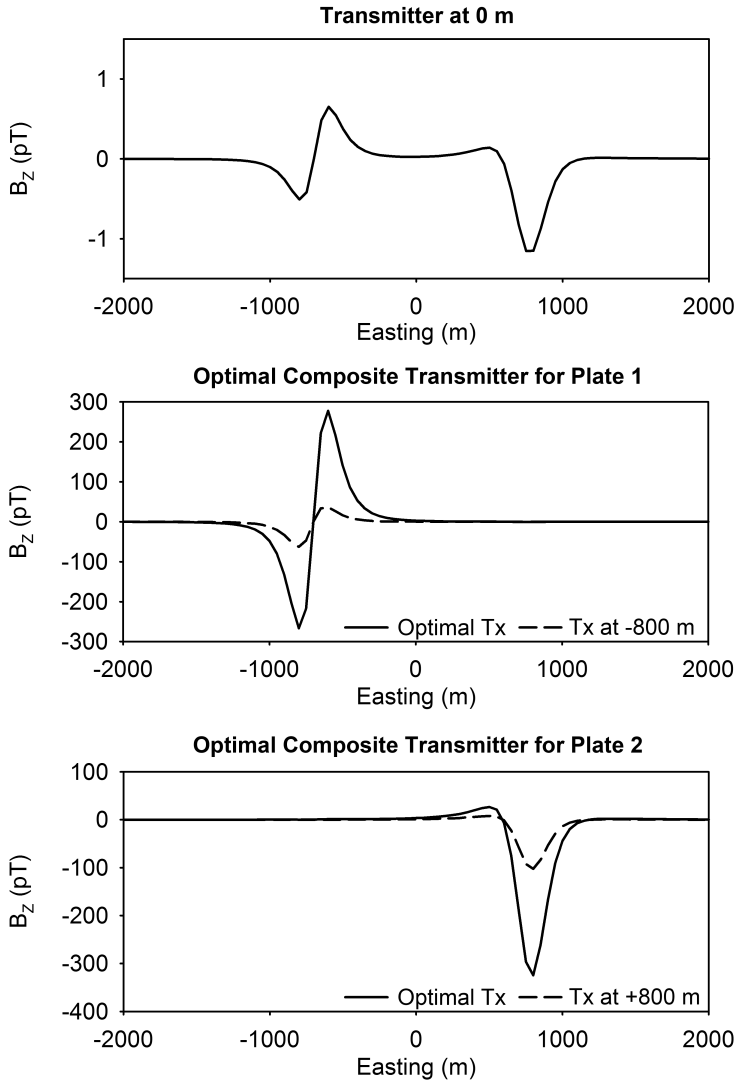

Figure 6-9: Comparison of single transmitter (Tx) profiles (top panel and dashed line in the middle and bottom panels) with that of the optimal composite transmitters (solid line, one for each target identified in Figure 6-8) for the survey depicted in Figure 6-7.

6.5 Field Example

A test time-domain EM survey was conducted over a small, thin dyke in the north-east range of the Sudbury Basin and is discussed in more detail in Lymburner and Smith (2015). Based on previous geophysical work, drilling and geological information, the near-surface target is believed to be at a depth of approximately 60 m to 120 m, trending at an azimuth of 33° and is vertical to sub-vertical. While this is a relatively shallow target, it was easily accessible and could act as a relatively easy target to validate the methodology. The test survey was conducted over a 1 km line with a station spacing of 25 m (3-component receiver coils). The 30 Hz transmitters (440 μs ramp turn-off, 20 000 Am^2 moment, 10 m by 10 m loop with 10 turns at 20 A), spaced every 25 m, occupied the inner 550 m of the line for a total of 23 transmitter positions. Stations in close proximity to the transmitter (± 50 m from the transmitter) contained no discernable signal. This is thought to be due to saturation of the receiver (analogue to digital converter) causing the readings to be corrupted (Lymburner and Smith, 2015). As such, these stations were removed during the data editing stage. The data from the *z*-component for a poorly coupled transmitter and a well coupled transmitter can be seen in Figure 6-10. Note that the well coupled transmitter (-150 m) has larger amplitudes, but a significant portion of the profile had to be removed due to corruption.

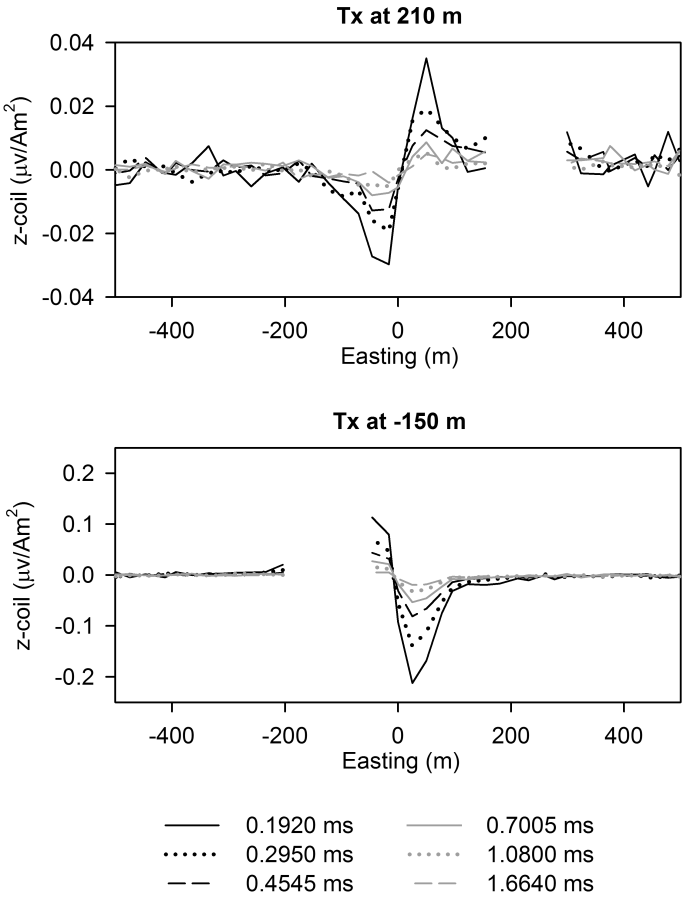

Figure 6-10: Off-time data collected overtop a shallow conductive dyke for two transmitter positions where the corrupted data (± 50 m from the transmitter position) has been removed. Top panel: poorly coupled, low S/N ratio, transmitter which shows the full anomalous response. Bottom panel: well coupled, high S/N ratio, transmitter where the western portion of the anomalous response is missing.

As the peak-to-peak distance in the *z* component of the anomalous response was only roughly 75 m (Figure 6-10), the majority of well coupled transmitters had a large portion of the anomalous/target response removed. Apart from the very low S/N ratio data from transmitters on

either ends of the line (Figure 6-10), no single transmitter contained the full response of the target. However, equation (6-2) will still produce a meaningful result as the sum of all of the transmitter positions contains the full response of the target (Lymburner and Smith, 2015). The look-up table in equation (6-2) (**L**) was modified to include the effect of having missing portions of the data in proximity to the transmitter positions. It was found that by removing many of the station positions, the solution had a bias towards shallow dipping near-surface targets. This effect was avoided by fitting only steeply dipping dipoles (± 30 ° from vertical) and decreasing the contribution from the *y* component which had the lowest S/N ratio. As the existing geological information and distal transmitters (where the data corruption does not coincide with the anomalous response; top panel in Figure 6-10) suggest a steeply dipping body, this restriction was justified. The estimate of the target location and orientation at an intermediate time channel can be seen in Figure 6-11.

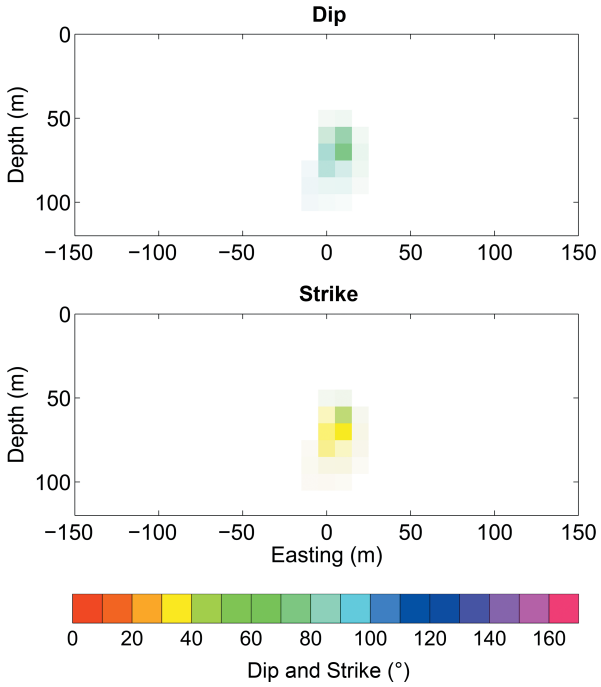

Figure 6-11: Equation (6-2) (α = 100%) calculated at an intermediate time channel over the field target (suspected to be at depth of approximately 60 m to 120 m, trending at an azimuth of 33° and is vertical to sub-vertical). The northing is equal to 10 m across the profile (i.e. the best fitting target is 10 m north of the surveyed profile). Each cell size is 10 m by 10 m.

The maximum *I* value in Figure 6-11 is at (10 m, 10 m, 70 m) at a strike and dip of 30° and 70°, respectively, which matches the suspected location and orientation of the body. Repeating the algorithm on progressively later time channels revealed that the peak *I* value deepened slightly (from 60 m to 90 m) and the dip became slightly steeper (from 70° to 90°). This may represent the migration of currents with time into a more conductive portion of the body. As the location and orientation of the target can now be estimated, the optimal composite transmitter can be constructed to form the high S/N ratio data (Figure 6-12, solid black line, top panel). For comparison, the look-up table (**L**) response is also shown (Figure 6-12, dashed grey line, top

panel). Note that while the composite transmitter response appears irregular (especially towards the east in both the *z* and *x* component), the irregularity is in fact expected as it is also seen in the look-up table profile. This irregularity is due to the data removed due to corruption (missing data adjacent to the transmitter locations) and the good fit between the composite transmitter and the look-up data supports the validity of our method which incorporates the corrupted data into our dipole look-up table model.

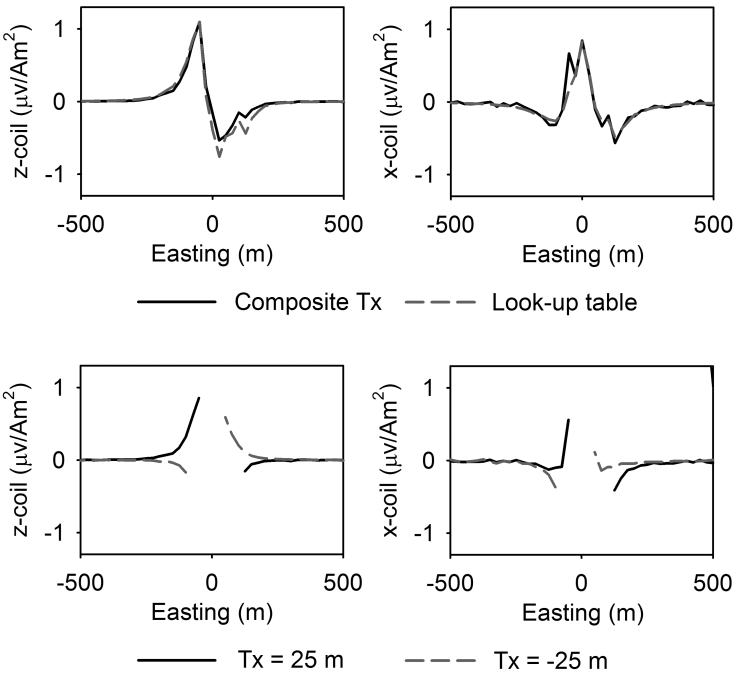

Figure 6-12: Top panel: comparison of the composite transmitter (Tx) response and that of the look-up table for the z (left) and x (right) components. Bottom panel: two well coupled single transmitter profiles showing extent of data corruption for the z (left) and x (right) components.

Since the body is relatively shallow, only the transmitters in close proximity to the center of the profile contributed significantly to the composite transmitter. As such, the relative increase in the signal amplitude using the composite transmitter is not as high as it was in the synthetic examples. However, in this example, interpreting the composite transmitter signal (Figure 6-12, top panel) is significantly easier than that of any single transmitter location (bottom panel of Figure 6-12 or Figure 6-10). The single transmitter locations only show half of the expected anomalous response due to the removal of the corrupted data. Any attempt to interpret the corrupted single transmitter data would have presented significant ambiguity as to the location and orientation of the target.

6.6 Discussion

Multi-transmitter data ensures adequate coupling and allows for the construction of a high S/N ratio, composite transmitter. The construction of the composite transmitter requires specifying the coupling between the transmitters and target, and as such, knowledge of the target location and orientation is essential. In this work, we solve this issue by assuming that the target response can be approximated with a dipole embedded within a fully resistive medium and that the coupling between the transmitter and the target can be approximated using the coupling between two dipoles. The dipole approximation has been used frequently in many areas of electromagnetic geophysics (e.g. Pasion and Oldenburg 2001; Sattel and Reid, 2006; Smith and Salem, 2007). The dipole approximation will be valid for discrete targets so long as the survey dimensions are large relative to the size and depth of the body. The dipole assumption will break down for large and shallow targets and apart from forward modeling it is difficult to predict when the approximation will fail. In general, the approximation breaks down gradually and

begins by fitting a dipole deeper than the actual position of the target. Moreover, equation (6-2) attempts to fit a single dipole to the data (or a section if windowing is used). If multiple close bodies are present, there will be an interaction between the two bodies and a superposition of their respective fields. Equation (6-2) minimizes this effect as the data are effectively stacked to reinforce the signal from a specific target, however, it is not always possible to separate the signals. Another potential complication arises if the background conductivity is high as the coupling between the transmitter and the target will be different than the free-space scenario (completely resistive background) and may also change as a function of delay time. However, a completely resistive background is a valid model in many areas of the world where deep exploration is ongoing and/or inevitable such as in the Canadian Shield and in Sudbury, Canada.

The overall multiple transmitter concepts discussed in this paper are not reliant on the limitations of the dipole model discussed above. More sophisticated models (e.g. non-dipole targets, conductive layered earth) could be used to derive coupling coefficients and to model the data in order to derive the optimal composite transmitter. Alternatively, the multi-transmitter data could be input into a large 3D inversion. The potential advantage of using a general 3D inversion is high as it can be used to characterize the entire subsurface, not just for target detection/characterization. However, in their current state, large 3D inversions are not easily used due to their associated cost, turnaround time and their general lack of availability.

Logistically speaking, the optimum way to collect multi-transmitter data would be with a hybrid ground/airborne system; the ground receivers can be laid out and then an airborne transmitter is flown. If an airborne transmitter is not possible or feasible, then using small, multi-turn, easily moveable, ground loops would be recommended. To reduce surveying time and cost it would be beneficial to lay many or all of the receivers at the same time so as to reduce the amount of times

the transmitter needs to be re-flown in the airborne case or moved in the ground case. This could be achieved with a distributed array ground receiver system such as the one developed in Golden et al., 2006. There are no commercial distributed array EM systems currently available, but this deficiency should be rectified soon. One further manner in which the logistics can be improved is by reducing the amount of data collected through the use of reciprocity. In Lymburner and Smith (2015), it was shown that in the field example presented here, the data density (and thus collection time) could be reduced by roughly 30% by applying the principles of reciprocity. Alternatively, the reciprocal data could be included in the summation process (i.e. forming the composite transmitter) to increase the signal-to-noise ratio of the data as was done in this study.

One missing piece of information not discussed in this work is the conductivity of the target. This can be determined through decay rate analysis in the time domain (inphase/quadrature ratio in the frequency domain) or through the use of conductivity-depth-imaging algorithms. The benefit of the method presented here, is that once the high S/N ratio composite transmitter data is created, it can be used in standard EM data processing and interpretation schemes.

6.7 Conclusion

Using multiple transmitter locations has the advantage of ensuring strong coupling between the transmitter and the target(s). Furthermore, if many independent high-powered transmitters are summed into a single composite transmitter, the S/N ratio can be drastically increased. Moreover, if enough transmitters are used they can be summed in different ways to highlight different targets which essentially allows for the systematic ‘probing’ of the subsurface for exploration targets. Deploying many large transmitters is logistically challenging and, as such, we suggest using many small high powered transmitters. The number of transmitters and their

respective dipole moments will control the maximum depth of exploration. The optimum manner to collect multiple transmitter data is using hybrid surveying methods where an airborne transmitter is flown overtop a distributed array of ground receivers.

The optimal manner in which the multiple transmitter data is summed depends on the location and orientation of the target(s). By discretizing the subsurface and possible target orientations, the approximate location and orientation can be found by comparing the measured response with the synthetic look-up table response of a target with a known location and orientation. Using synthetic examples, we show that this methodology is robust and can accurately determine the location and orientation of discrete target(s) embedded within a resistive medium. Once this is known, the multiple transmitter data can be summed into a single large S/N ratio composite transmitter. In a ground time-domain EM field test, 23 transmitter positions were used and a shallow target could be identified using the developed methodology. The produced composite transmitter data was considerably easier to interpret and had a higher signal amplitude than the data from any one single transmitter.

The work presented here provides an alternative strategy for high-finesse surveys in complex conductor environments where many transmitter-to-target coupling angles are required and for deep focused exploration which will be required where deeper targets are being sought. Future work aims to test and modify the methodology to work on targets embedded within a conductive half-space and/or layered earth.

6.8 References

Golden, H., T. Herbert, and A. Duncan, 2006, GEOFERRET: a new distributed system for deep-probing TEM survey: Presented at the 76th Annual International Meeting in the Workshop on Uranium Exploration, SEG.

Lymburner, J., and R. Smith, 2015, A procedure for collecting electromagnetic data using multiple transmitters and receivers capable of deep and focussed exploration: Geophysics,80(1), E1–E10. doi: 10.1190/GEO2014-0251.1.

Nabighian, M. N., and J. C. Macnae, 1991, Time domain electromagnetic prospecting methods, *in* M. N. Nabighian, ed., Electromagnetic methods in applied geophysics, Applications, Part A and B: SEG, Investigations in Geophysics No. 3, Volume **2**, 427–520.

Palacky, G. J., and G. F. West, 1991, Airborne electromagnetic methods, *in* M. N. Nabighian, ed., Electromagnetic methods in applied geophysics, Applications, Part A and B: SEG, Investigations in Geophysics No. 3, Volume **2**, 811–879.

Pasion, L., and D. Oldenburg, 2001, A Discrimination Algorithm for UXO Using Time Domain Electromagnetics: Journal of Environmental and Engineering Geophysics, **6**, 2, 91-102.

Polzer, B., J. Macnae, Y. Lamontagne, and R. Koch, 1989, Lateral resolution enhancement of TEM data by correlation processing. SEG Technical Program Expanded Abstracts, 182-184. doi: 10.1190/1.1889600

Powell, B., G. Wood, and L. Bzdel, 2007, Advances in geophysical exploration for uranium deposits in the Athabasca Basin, *in* B. Milkereit ed. Proceedings of Exploration 07: Fifth Decennial International Conference on Mineral Exploration, 771-790.

Powell, B., 1990, Large loop EM surveys in the Athabasca Basin, *in* L. S. Beck, and C.T. Harper, eds., Modern Exploration Techniques, Saskatchewan Geological Society, 74 - 93.

Sattel, D., and J. Reid, 2006, Modelling of airborne EM anomalies with magnetic and electric dipoles buried in a layered earth: Exploration Geophysics, **37**, 3, 254-260.

Smith, R. S., and A. S. Salem, 2007, A discrete conductor transformation of airborne electromagnetic data: Near Surface Geophysics, **5**, 87-95.

Smith, R., and A. Volkovitsky, 2014, Airborne electromagnetic prospecting systems, *in* A. A. Kaufman and M. Oristaglio, eds., Principles of electromagnetic methods in surface and borehole geophysics: Methods in Geochemistry and Geophysics, Volume 45. ISSN 0076-6895. Elsevier B.V., in press.

Smith, R., D. Fountain and M. Allard, 2003, The MEGATEM fixed-wing transient EM system applied to mineral exploration: a discovery case history: First Break, **21**(7), 73-77.

Snyder, D. D., and C. P. Oden, 2012, Optimizing the MetalMapper for static “cued ID” measurements over UXO: Symposium on the Application of Geophysics to Engineering and Environmental Problems 2012, 333-347.

Telford, W. M., L. P. Geldart, and R. E. Sheriff, 1990, Applied geophysics: Cambridge University Press.

Walker, P., and G. F. West, 1991, A robust integral equation solution for electromagnetic scattering by a thin plate in conductive media: Geophysics, **56**, 8, 1140-1152.

Zhdanov, M. S., 2010, Electromagnetic geophysics: Notes from the past and the road ahead: Geophysics, **75**, 5, 75A49-75A66.

Chapter 7

7 Inductive electromagnetic data interpretation using a three-dimensional distribution of three-dimensional magnetic or electric dipoles

7.1 Abstract

In inductive electromagnetics, the magnetic field measured in the air at any instant is a potential field. As such, we can invert measured magnetic fields (at a fixed time or frequency) for the causative subsurface current system. In this paper, we approximate these currents with a 3D subsurface grid of 3D magnetic (closed loop current) or electric (line current) dipoles and we solve for the location and orientation of the dipole using a potential field-style smooth-model inversion. Since the problem is linear, both inversions can be solved quickly even for large subsurface volumes; and both can be run on a single data set for complementary information. Synthetic studies suggest that for induction dominated targets the magnetic and electric dipole inversions can be used to determine the center and top edge of the target, respectively. Furthermore, the orientation of the targets can be estimated from visual examination of the orientations of the 3D vector dipoles and/or using the interpreted location of the center and top edge of the target. In the first field example, ground data from a deep massive sulfide body (mineral exploration target) was inverted and the results were consistent with the conclusions drawn from the synthetic examples and with the existing interpretation of the body (shallow dipping conductor at a depth of roughly 400 m). A second example over a near-surface mine

tailing (near surface environmental/engineering study) highlighted the strength of being able to invert data using either magnetic or electric dipoles. While both models were able to fit the data, the electric dipole model was considerably simpler and revealed a SW-NE trending conductive zone. This fast approximate 3D inversion can be used as a starting point for more rigorous interpretation and/or, in some cases, as a standalone interpretation tool.

7.2 Introduction

The goal of most electromagnetic (EM) surveys is to produce an image of the electrical properties of the subsurface which can explain the measured EM response. In inductive EM there are a variety of methods available and they range from simple and approximate back-of-the-envelope style calculations to sophisticated and numerically intensive 3-dimensional (3D) inversions which adhere to the full physics of the problem. While full physics 3D inversions, such as the ones suggested in Haber et al. (2002), Cox et al. (2010) and Oldenburg et al. (2013), are increasing in popularity their widespread use is limited due to their inherent complexity which restricts their availability and increases their cost (both monetary and in time). As such, many prefer to use simplified approaches whereby the dominant method depends strongly on the system used, the geology and the goal of the survey.

In airborne EM, 1D apparent conductivity imaging methods (i.e. converting amplitude and time pairs into corresponding conductivity and depth pairs) and layered earth inversions are predominate and they are typically stitched into 2D sections or 3D volumes (Macnae and Lamontagne, 1987; Macnae et al., 1991; Smith et al., 1994; Sattel, 1998; Christensen, 2002; Huang and Rudd, 2008). While imaging and layered earth methods are still routinely used in ground EM, user driven iterative (i.e. trial-and-error) forward modelling using semi-fixed

conductor shapes (i.e. parametric models) are equally if not more popular especially in certain areas such as in mineral exploration within the Canadian Shield. The most frequently used conductor models are thin plates (West et al., 1984; Macnae and Lamontagne, 1987; Nabighian and Macnae, 1991; Liu and Asten, 1993; Smith, 2000; Kolaj and Smith, 2013), prisms (Murray et al., 1999; Sattel, 2004) and dipoles (King and Macnae, 2001; Smith and Salem, 2007; Sattel and Reid, 2006; Schaa and Fullagar, 2010; Kolaj and Smith, 2015). The forward operator in these parametric models is considerably less complicated than that in 3D models that describe the full physics and as such they can often be incorporated into automated inversion routines. This is especially true for the dipole model and as such there are many examples of semi-automated to fully-automated inversion routines using dipoles. For example, Smith and Salem (2007) and Kolaj and Smith (2015) used free-space magnetic dipole look-up tables to fit airborne and ground EM data. Sattel and Reid (2006) used a combination of magnetic dipoles and electric dipoles (cross-strike directed line current) embedded in a layered earth to fit spatially discrete airborne EM anomalies. There is also considerable research into dipole based interpretation within the unexploded ordinance community (Pasion and Oldenburg 2001; Beran et al., 2012 and references therein). While the other work generally fit discrete EM anomalies with single dipoles, using the concepts of moments (Smith and Lee 2001, 2002), Schaa and Fullagar (2010) and Fullagar et al. (2015) developed a 3D inversion which fit resistive-limit EM data using a discretized subsurface grid of magnetic dipoles. By using resistive limit data they were able to take full advantage of potential field style linear inversion which is significantly faster than traditional 3D EM inversion. As dipole based inversions can provide significant information at a low cost, it is an attractive choice, especially for preliminary, short turnaround interpretations.

Under the quasi-static assumption (i.e. negligible displacement current), the secondary magnetic field is a potential field at any given time and can thus be calculated from the subsurface current distribution at that time (Nabighian and Macnae, 1991). In our work, we assume that at a given fixed time, this current system can be approximated with a 3D subsurface grid of static magnetic (a unit area circular current loop) or electric (a small current element) dipoles. As such, we can use the measured secondary magnetic field at a fixed time or frequency to quickly solve for a 3D distribution of subsurface dipoles using a potential field style inversion similar to Schaa and Fullagar (2010). By using the resistive limit, Schaa and Fullagar (2010), can effectively only determine one current distribution, but our approach can determine the amplitude and orientation of the dipoles (which can be either magnetic or electric) at a single time or for a series of times and can therefore provide significant detail about the location and migration of currents in the subsurface. This knowledge can be used as is or as a starting model for more rigorous interpretation.

We begin by presenting our forward and inversion methodology which we test on a synthetic plate target example. The inversion is then tested on two fixed-loop ground surveys. The first example consists of a single receiver component survey over a deep massive sulfide body (mineral exploration example) while the second example uses 3-component receiver data collected over a near surface tailing pond which was the focus of an environmental and engineering study.

7.3 Methodology

In the forward model, the magnetic field at the measurement station is calculated from the sum of the magnetic fields generated by a discretized subsurface grid of 3D cells with three

orthonormal dipoles (dipoles oriented along the *x*, *y* and *z* axes) in each cell center. This can be written mathematically for *n* total cells as,

$$\mathbf{H}^{\mathrm{S}}(\mathbf{s}) = \sum_{k=1}^{n} \mathbf{M}_k \, \mathbf{G}_k(\mathbf{s}) \, V_k \,, \tag{7-1}$$

where **s** corresponds to the position vector of the station location, the vector, $\mathbf{M}_k$, corresponds to the moment of each dipole (units of Am^2 and Am for magnetic and electric dipoles, respectively) within cell *k*. $\mathbf{G}_k$ is a tensor corresponding to the nine components of magnetic fields generated by the 3 dipoles centered within cell *k* of volume V_k (dimensionless scalar). In our formulation, **G** is constructed from three separate vectors ($\mathbf{g}_i$), which for a magnetic dipole is (Ward and Hohmann, 1988)

$$\mathbf{g}_i(\mathbf{s}) = \frac{1}{4\pi|\mathbf{r}-\mathbf{s}|^3}\left[\frac{3\,\hat{\mathbf{m}}_i \cdot (\mathbf{r}-\mathbf{s})}{|\mathbf{r}-\mathbf{s}|^2}(\mathbf{r}-\mathbf{s}) - \hat{\mathbf{m}}_i\right], \tag{7-2}$$

and for an electric dipole is (Ward and Hohmann, 1988)

$$\mathbf{g}_i(\mathbf{s}) = \frac{\hat{\mathbf{m}}_i \times (\mathbf{r}-\mathbf{s})}{4\pi|\mathbf{r}-\mathbf{s}|^3}, \tag{7-3}$$

where **r** is the position vector of the cell center, $\hat{\mathbf{m}}$ is equal to the unit vector of the dipole in each of the three cardinal directions so that *i* refers to the directional axis of the dipole (either *x*, *y*, or *z*). The forward model (equations (7-1) to (7-3)) solves for the magnetic field produced by a subsurface distribution of orthogonal magnetic or electric dipoles and in this work we use the moment of those dipoles (**M**) as a proxy to the established current system.

In the inverse problem, we are attempting to solve for an equivalent distribution of dipoles that match the measured magnetic field at a particular instance in time (or at a specific frequency). The forward model does not explicitly take any background medium into consideration so the inverse problem is applicable for discrete targets embedded in a resistive half-space. If a background response is present a possible option would be to strip the background response (Smith and Salem, 2007) and/or simply use a late enough delay time (or low enough frequency) where the background response is small. Alternatively, our formulation could also be used to find a subsurface current distribution that explains the background response of the conductive host in addition to the anomalous response. Since there is no temporal variable in equations (7-1) to (7-3) the problem must be solved separately for each frequency or time. The system is typically overdetermined and can be solved by minimizing (2-norm) the functional, $f(\mathbf{M})$,

$$f(\mathbf{M}) = \left\|\mathbf{W}_\sigma(\mathbf{GM} - \mathbf{H}^{\mathrm{S}})\right\|^2 + \alpha_x\|\mathbf{W}_x\mathbf{ZM}\|^2 + \alpha_y\left\|\mathbf{W}_y\mathbf{ZM}\right\|^2 + \alpha_z\|\mathbf{W}_z\mathbf{ZM}\|^2 + \alpha_s\|\mathbf{W}_s\mathbf{ZM}\|^2 , \tag{7-4}$$

where $\mathbf{M}$ is the vector of dipole moments that are being solved for, $\mathbf{G}$ is the matrix representation of the forward model operator from equations (7-1) to (7-3) (with inclusion of the volume term V) and $\mathbf{H}^{\mathrm{S}}$ are the measured magnetic fields to be fit. The weighting matrices $\mathbf{W}_x$, $\mathbf{W}_y$, and $\mathbf{W}_z$ are smoothing regularization matrices (first finite difference operators) that smooth each dipole moment in each of the 3 Cartesian directions, $\mathbf{W}_\sigma$ is a weighting matrix corresponding to the inverse of the data error (if known) and $\mathbf{W}_s$ encourages model smallness (i.e. minimum complexity). Depth weighting is applied with the diagonal matrix $\mathbf{Z}$, which, like in potential field inversion, is necessary so as to counteract the rapid drop-off in amplitude of the magnetic field with distance (equations (7-2) and (7-3)). Without adequate depth weighting, the solution will

favour a near-surface model (i.e. the dipoles are concentrated in the top layer(s) of the discretized subsurface) regardless of the true depth of the causative features. To solve this issue we adopt the depth weighting scheme from Li and Oldenburg (1996),

$$Z_{ii} = z^{-\beta/2}\,, \tag{7-5}$$

where the values of Z_{ii} make up the entries of the diagonal matrix $\mathbf{Z}$, z is the depth from the average station elevation to the center of the subsurface cell. A natural choice for β would be the fall-off rate of the dipole amplitude (i.e. $\beta = 3$ for magnetic dipoles and $\beta = 2$ for electric dipoles) but in our experience leaving $\beta = 3$ in almost all circumstances produced favourable results. The regularization parameters (α_x, α_y, α_z and α_s) control the relative influence of the smoothing matrices and the model smallness (and together the influence of depth weighting) as compared to the data misfit (first term in equation (7-4)). Since equation (7-4) (the inverse problem) can be solved in a few seconds using a conjugate gradient method implemented in MATLAB, it is possible to solve it for many different regularization parameters. In our implementation, we generally solve for the optimum α values using a combination of an L-curve analysis (Zhdanov, 2002) and a qualitative analysis of the solutions obtained.

It should be noted that the inversion (equations (7-2) to (7-4)) solves for 3-orthogonal dipole moments within each cell (i.e. a vector dipole moment) and each dipole moment direction (x, y and z) can be analyzed/interpreted separately. However, for imaging and interpretation purposes it is preferably to convert the vector dipole moment into a scalar value by taking the magnitude of the dipole moment vector within each cell and we represent this value as $|\mathbf{M}_m|$ or $|\mathbf{M}_e|$ (magnitude of the magnetic or electric vector dipoles, respectively). As we lose the orientation information by using a scalar magnitude we also plot the vector dipole moments using vector

fields (generally only those with a magnitude above a certain threshold). In this manner, we use the magnitude as a proxy to strength of the established current system and the vector fields as an indication of the orientation of that current system.

7.4 Synthetic Examples

Two time-domain fixed-loop ground surveys using 400 m by 200 m 50 S conductive plates embedded in a resistive halfspace were simulated in GeoTutor (PetRos EiKon) using the VHPlate algorithm (Walker and West, 1991) and the survey geometry (line and station spacing was 150 m and 50 m, respectively), plate properties, and z-component response from the central line can be seen in Figure 7-1. For our inverse problem, the subsurface was discretized into 25 m by 25 m by 25 m cells (easting, northing and depth, respectively) and the inversion (equation (7-4)) was run for a late off-time channel (t = 9.4 ms; 30 Hz base frequency) for both magnetic and electric dipoles. The computation times for the inversions presented were all generally less than 10 seconds (per suite of regularization parameters) and the root mean squared error for all inversions was less than 10^{-2}.

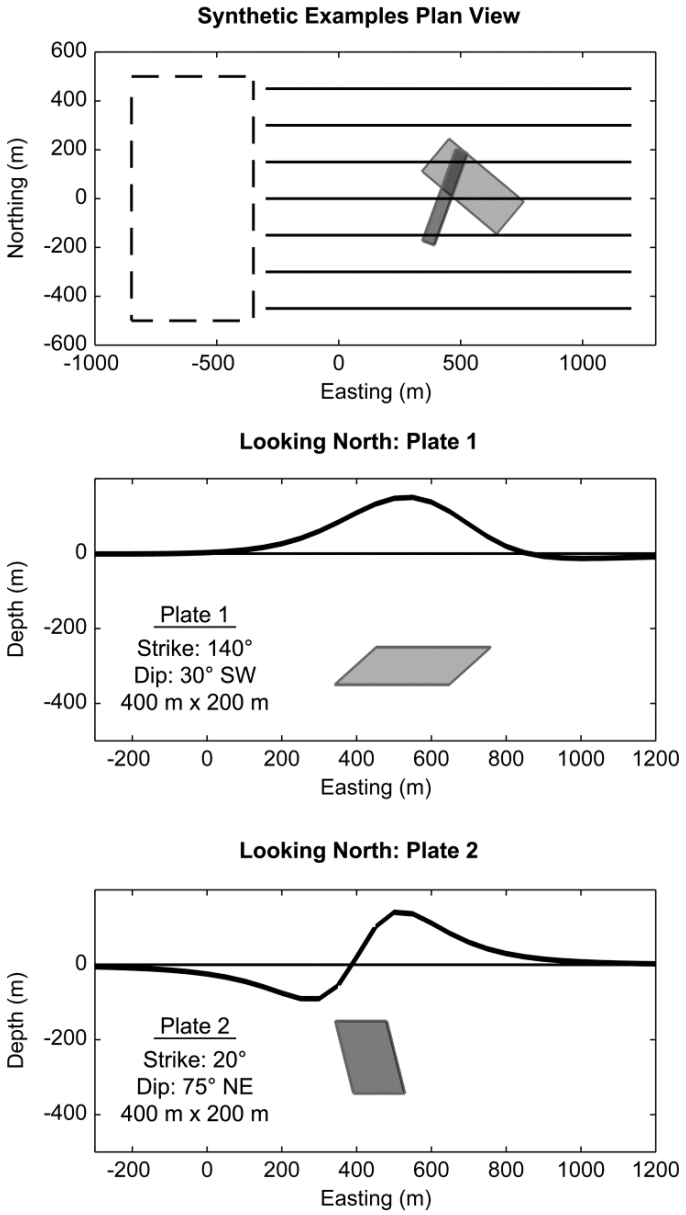

Figure 7-1: Top: Plan view of the survey geometry of the two synthetic models (Plate 1 and 2) simulated in GeoTutor. Transmitter loop is shown with a dashed line and the station lines are depicted with thin solid black lines. Middle: First synthetic example (Plate 1, grey plate) consisted of a 140°/30° SW (strike/dip) plate (plate 1) with a depth to top of 250 m. Bottom: Second synthetic example (Plate 2, black plate) consisted of a 20°/75° NE plate (plate 2) with a depth to top of 150 m. The z-component response (t = 9.4 ms) for the central line for both surveys is shown with a thick black line.

In the first example, a 140°/30° SW (strike/dip) plate (plate 1, Figure 7-1) with a depth to top of 250 m was used and the inversion results ($|\mathbf{M}_m|$ and $|\mathbf{M}_e|$) for both magnetic and electric dipoles can be seen in Figure 7-2. For the magnetic dipole inversion the dipoles were concentrated around the center of the plate with the largest amplitude dipole being located slightly SW (in the dip direction) of the plate center. While the location matches well with the actual location of the plate, the general shape of the anomalous zone does match the strike or dip of the plate. This information is better resolved with the electric dipole inversion which fit dipoles along the top edge of the plate (peak dipole at a depth of -225 m) with the anomalous zone oriented parallel with the true strike of the plate. Since the magnetic inversion indicated the center of the plate and the electric inversion indicated the top edge it is possible to estimate the dip of the target which in this case is calculated to be 31° which matches the true dip of 30°.

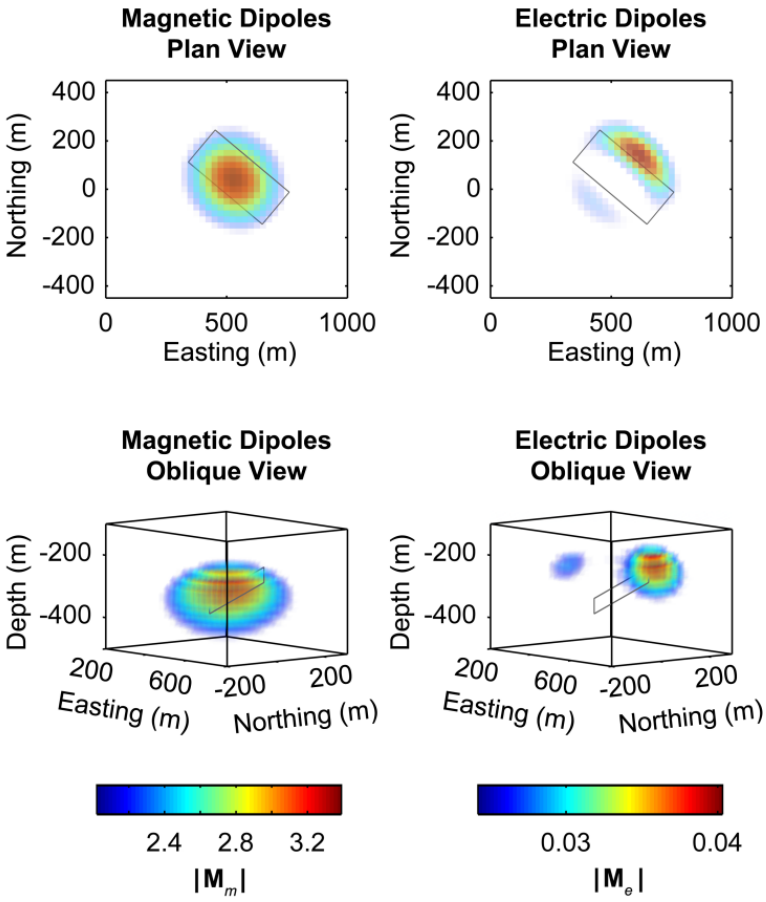

Figure 7-2: Plan (top) and oblique (bottom) view of the results of the magnetic (left column) and electric (right column) dipole inversion (equation (**7**-2) and (**7**-4); the regularization parameters α_x, α_y, α_z and α_s were equal to 0.007 and 0.03 for the magnetic and electric dipole inversion, respectively) for survey 1 (Plate 1, Figure **7**-1).The magnitude of the vector dipole moment ($|M_m|$ and $|M_e|$) at each location is depicted, whereby, hotter colors represent higher amplitude dipoles. Magnetic and Electric dipoles with magnitudes less than 2 Am^2 and 0.025 Am, respectively, are not shown. The outline of the plate target is shown with the dark-grey line.

In the second example, a 20°/75° NE (strike/dip) plate (plate 2, Figure 7-1) with a depth to top of 150 m was used and the inversion results ($|\mathbf{M}_m|$ and $|\mathbf{M}_e|$) for both magnetic and electric dipoles can be seen in Figure 7-3. As with the previous example, the magnetic dipoles were concentrated around the center of the plate and the largest amplitude dipole is located slightly away (in the dip direction) from the true plate center. However, unlike the previous example, the strike and dip direction is roughly reflected in the shape of the magnetic dipole anomaly whereby there is a 'tail' of anomalous dipoles which extends away from the plate opposite to the dip direction. This 'tail' was observed in other synthetic examples, especially, when the plate was steeply dipping. As before, the electric dipole inversion clusters parallel to the top edge of the plate (peak dipole at a depth of -125 m) and the strike direction can be clearly inferred. Calculating the dip using the location of the peak electric and magnetic dipoles suggests a dip of 60° which is smaller than the true dip of 75°. This discrepancy is likely due to the fact that the peak electric dipole is slightly above the true location of the plate and that the peak magnetic dipole is located away from the true center of the plate. The error these discrepancies introduce into the dip calculation is also predicted to increase with increasing dip of the target.

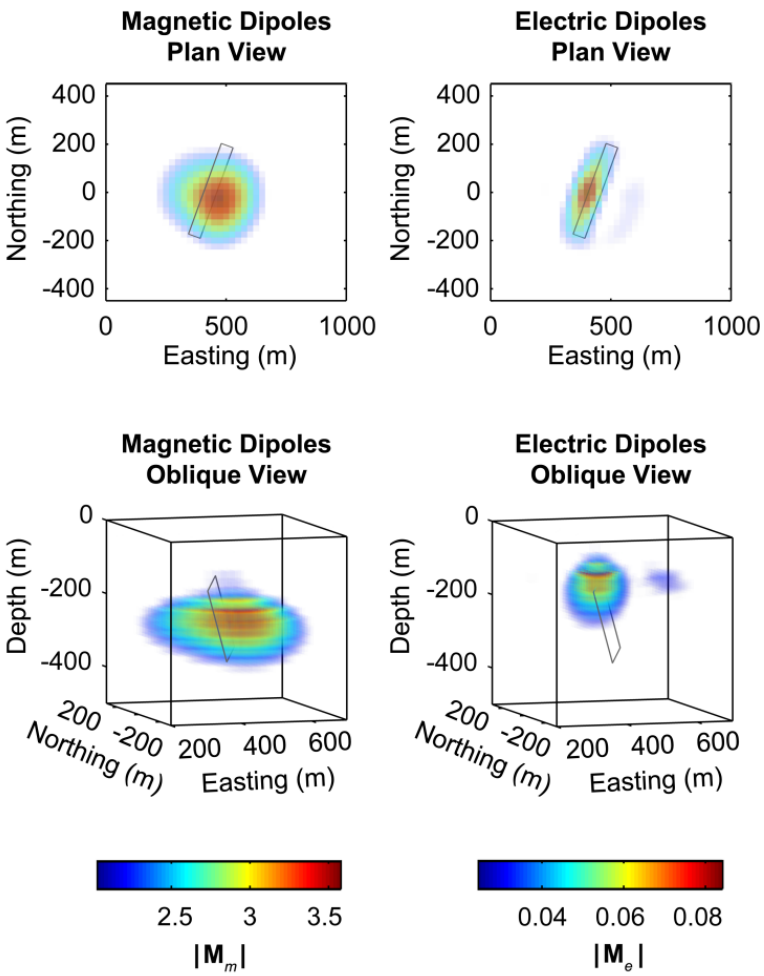

Figure 7-3: Plan (top) and oblique (bottom) view of the results of the magnetic (left column) and electric (right column) dipole inversion (equation (**7**-2) and (**7**-4); the regularization parameters α_x, α_y, α_z and α_s were equal to 0.006 and 0.009 for the magnetic and electric dipole inversion, respectively) for survey 2 (Plate 2, Figure **7**-1). Magnetic and Electric dipoles with magnitudes less than 2 Am^2 and 0.025 Am, respectively, are not shown. The outline of the plate target is shown with the dark-grey line.

As was mentioned in the methodology section, the orientation of the anomalous features can also be determined by examination of the vector orientation of the dipoles. A vector field map for both synthetic examples is plotted in Figure 7-4. In the top panel of Figure 7-4 the electric dipole vector orientations are shown in a plan view. The electric dipoles define a horizontal current system parallel with the strike of the target where, again, the largest amplitude dipoles are located roughly along the top edge of the plate target. In the bottom panel of Figure 7-4 the magnetic dipole vector orientations are shown in the exact oblique view as in Figures 7-2 and 7-3. In all cases, the peak amplitude magnetic dipole underestimates the true dip of the plate but the magnetic dipoles coincident with the actual location of the plate accurately reflect the true dip of the plate. In our experience, using all available information (magnitude, dip estimate from magnetic to electric dipole centers and the vector fields) it is possible to accurately and quickly estimate the location and orientation of plate targets. As these inversions are fast and simple to use, they do not require an initial guess and can be run as a preliminary step to gain insight into the subsurface geology. Moreover, the results could be used to guide a starting model for the more time-consuming interpretation routines such as iterative forward modeling or inverse modelling that requires an initial guess.

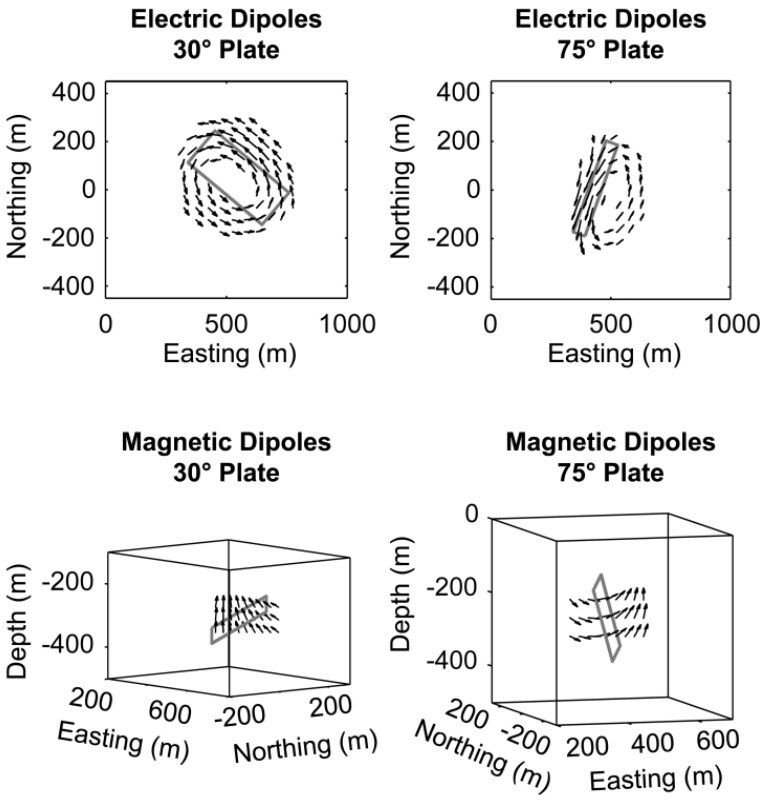

Figure 7-4: Plan (top) and oblique (bottom) view of the dipole moment vectors corresponding to the magnetic and electric dipole inversion models for both synthetic examples from Figures **7-**2 and **7-**3. The outline of the plate target is shown with the dark-grey line.

7.5 Field Examples

In the following section we present two field examples of the dipole inversions. In the first example, the inversion is run on a deep mineral exploration target whereas the second example is concerned with the characterization of a near-surface tailings pond surveyed for environmental

and engineering applications. The success of the inversion on these two very different examples aims to showcase the generality and potential applications of this method.

7.5.1 Deep mineral exploration

The Joe Lake property is located in the North range of the Sudbury Igneous Complex and contains a deep, shallow-dipping sulfide body which was discovered with a ground EM UTEM survey (Watts, 1997). The example showcases the ability of ground EM to discover deep conductive targets as the late time channel data showed a distinct anomaly over four to five lines. The ground EM survey consisted of single vertical component (B_z) data at a nominal station and line spacing of 50 m and 100 m respectively.

For the dipole inversion, the subsurface was discretized into 25 m by 25 m by 25 m cells (easting, northing and depth, respectively) up to a depth of 800 m and the results and the corresponding data fit (t = 0.7812 ms, 31 Hz base frequency) for four lines can be seen in Figures 7-5 and 7-6, respectively. It should be noted that the field data was lightly smoothed with a 3-point averaging filter in order to smooth the data at the ends of the lines where the signal-to-noise ratio was the poorest. The magnetic dipole inversion revealed a body centered at [4025 m, 1275 m, -400 m] (Figure 7-5, left column) and interpretation of the vector orientations of the dipole moments (Figure 7-5, bottom left) suggests that the body is shallow-dipping to the SE. The electric dipole solution (Figure 7-5, right column) is consistent with a SE dipping body as the peak electric dipole, [3900 m, 1450 m, -275 m], is NW of the magnetic anomaly and the orientation of the electric dipole moment vectors (Figure 7-5, top right) suggests a NE-SW striking body. The strike and dip were calculated to be 55° and 30° SE, respectively, using the peak magnetic and electric dipole locations which also agrees with the previous interpretations.

The ground EM survey data was previously modelled and interpreted using the plate modelling software MultiLoop (Lamontagne Geophysics). It was modelled with a south dipping (30°) plate centered at 1300 N with a depth to top ranging from 375 m to 425 m (Watts, 1997) which is consistent with the results of the magnetic and electric dipole inversion. There is a slight discrepancy between the predicted depth to the top edge of the plate (-275 m from the electric dipole inversion) but in the synthetic studies it was found that the peak electric dipole tended to be variably above the true location of the plate which may explain the difference.

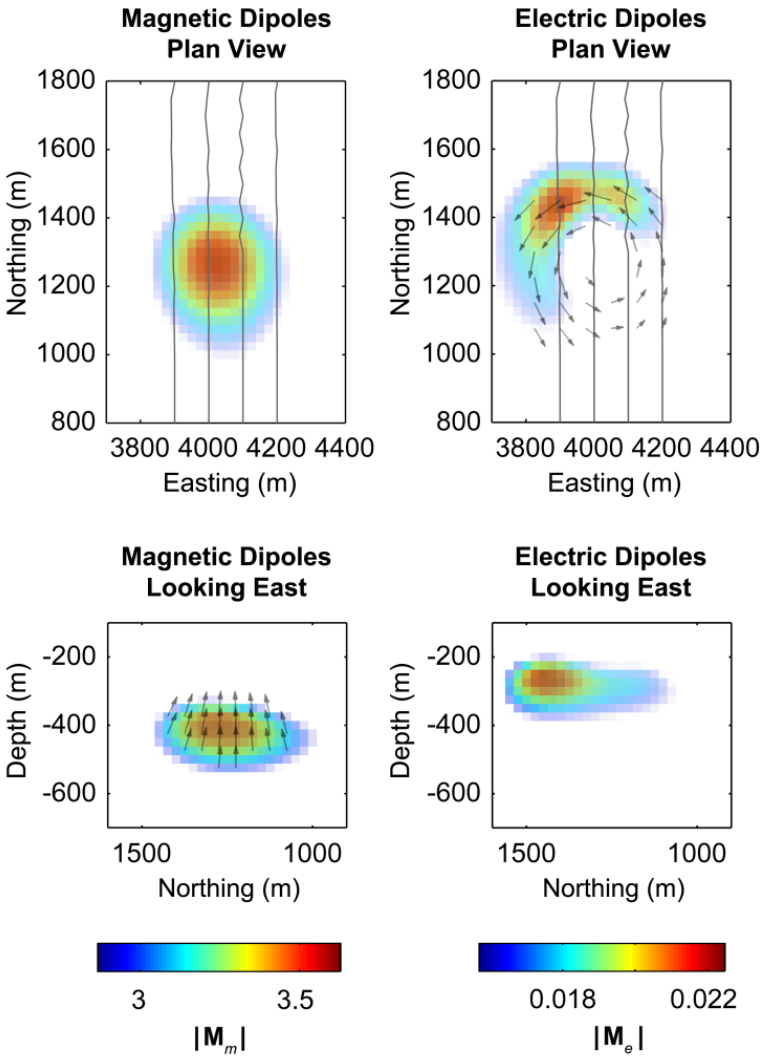

Figure 7-5: Plan (top) and looking east (bottom) view of the results of the magnetic (left column) and electric (right column) dipole inversion (equation (**7**-2) and (**7**-4); the regularization parameters α_x, α_y, α_z and α_s were equal to 0.008 and 0.08 for the magnetic and electric dipole inversion, respectively) for the Joe Lake survey (computation times in the order of a few seconds per inversion). Magnetic and Electric dipoles with magnitudes less than 2.9 Am^2 and 0.016 Am, respectively, are not shown. Station lines are depicted with thin solid grey lines. Select dipole moment vectors corresponding to depth = -275 m (top right panel) and easting = 4025 m (bottom left panel) are shown.

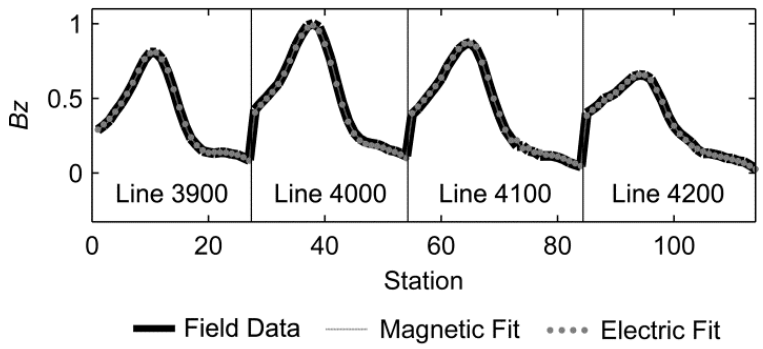

Figure 7-6: Comparison of the field data (thick solid black line) and the model data from the magnetic (solid grey line, Figure **7-**5 left column) and electric (dashed grey line, Figure **7-**5 right column) dipole inversion for the vertical component of the magnetic field. The data was normalized to the peak value. All four lines of data are shown in series (separated by solid black lines), whereby, the station number increases from west to east and south to north.

7.5.2 Near-surface environmental characterization

The second field example consists of a 3-component fixed in-loop survey collected overtop an old dry tailings pond in Sudbury, Ontario, Canada. Tailings are the waste material produced after processing ore to extract valuable metals and can be as large as several kilometers in length and several tens of meters in height. The original survey was carried out in an effort to map the electrical properties, which could be used as a proxy to map potential contaminants, fluids and/or anomalous concentrations of leftover metals (Kolaj and Smith, 2013 and Kolaj and Smith, 2014). The survey consisted of 5 lines with a station and line spacing of roughly 20 m and 40 m, respectively, inside of a 700 m by 350 m transmitter loop.

The subsurface was discretized into 10 m by 10 m by 3 m cells (easting, northing and depth, respectively) up to a depth of 120 m. An early off-time channel was fit (t = 0.295 ms, 30 Hz base

frequency) and the results of the magnetic and electric dipole inversion and the corresponding data fit can be seen in Figures 7-7 and 7-8, respectively. It should be noted that for this example, the depth weighting matrix (**Z** in equation (7-4)) was removed from the smoothing operators as without this change it was found that the inversion was unable to successfully fit a smooth near surface model to the data.

For the magnetic dipole inversion (Figure 7-7, left column), the majority of the response could be explained via two shallow anomalies located to the south of Line 50S. The vector dipole moments (Figure 7-7, bottom left panel) reveal that the two anomalies represent peak positive and negative *z*-directed dipole moments which appear to be circulating around a N-S trend located at 220 E. A potential explanation is that the data cannot be fit with discrete magnetic dipoles and in order to produce the dominate B_z cross-over type response (*z* response in Line 50S) the inversion mapped the distribution of the subsurface magnetic fields rather than an underlying causative feature. It is also possible that this is due to over-regularization but experimentation with coarser grids and smaller smoothness constrains did not remove this feature. On the other hand, the electric dipole inversion (Figure 7-7, right column) produced a more realistic solution; a shallow north to north-east directed line current. This can also explain the circulating magnetic dipoles as magnetic fields curl around a line current (i.e. Ampere's Law). There are some curling effects to the West and East of the peak electric dipole and this is likely an artifact due to the smoothing regularization and/or the necessity to also include a minor magnetic dipole component. The underlying cause of the line current is unknown but it could potentially include any conductive feature such as a buried pipe, conductive channel of fluids/material and/or a near vertical feature such as a conductive fault.

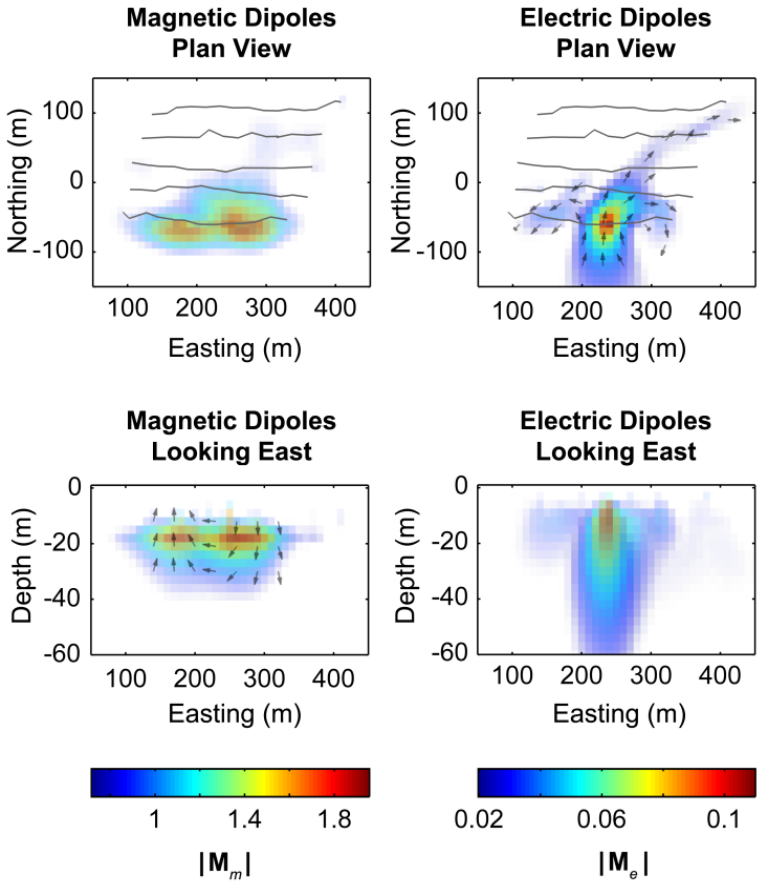

Figure 7-7: Plan (top) and looking east (bottom) view of the results of the magnetic (left column) and electric (right column) dipole inversion (equation (7-2) and (7-4); the regularization parameters α_x, α_y, α_z and α_s were equal to $2x10^{-3}$, $2x10^{-3}$, $6x10^{-3}$,$1x10^{-4}$ and $1x10^{-1}$, $1x10^{-1}$, $6x10^{-3}$, $2x10^{-2}$ for the magnetic and electric dipole inversion, respectively) for the tailing survey. Magnetic and Electric dipoles with magnitudes less than 0.7 Am^2 and 0.02 Am, respectively, are not shown. Station lines are depicted with thin solid grey lines. Select dipole moment vectors corresponding to depth = -15 m (top right panel) and northing = -60 m (bottom left panel) are shown.

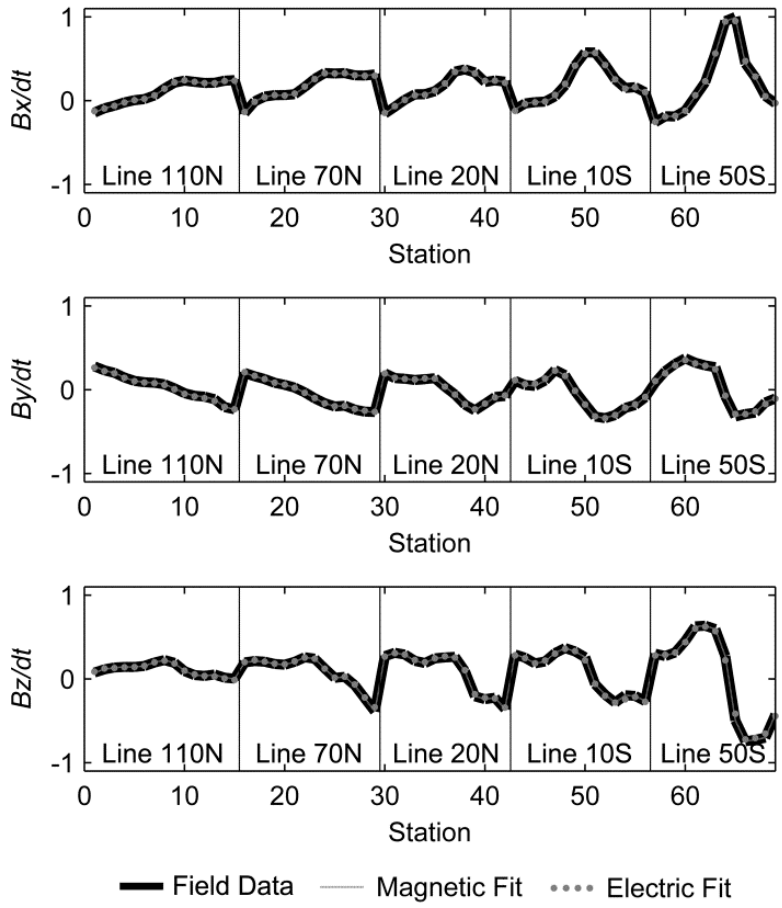

Figure 7-8: Comparison of the field data (thick solid black line) and the model data from the magnetic (solid grey line, Figure 7-7 left column) and electric (dashed grey line, Figure 7-7 right column) dipole inversion for the three components of the magnetic field. The magnetic field components were normalized to the peak value. All five lines of data are shown in series (separated by solid black lines), whereby, the station number increases from west to east and north to south.

7.6 Discussion

Both the synthetic and field examples show that typical discrete target responses can be reliably fit with a 3D volume of dipoles. In our experience, the near-center of the plate can be determined using magnetic dipoles. Using the magnetic vector dipole moments, the orientation corresponding to the peak dipole moment tends to underestimate the dip and a more accurate estimate can be made by an analysis of the adjacent vector dipole moments. However, this can be somewhat subjective and without prior knowledge of the true target location it is difficult to determine which vector dipole moments are the most reliable. For induction dominated targets, the electric dipole inversion, places the dipoles at positions and orientations that are consistent with the strike of the target and tend to be in close proximity to the top of the shallowest edge of the target. As magnetic dipoles tend to concentrate at the center of the target and the electric dipoles along the top edge, the orientation of the target can be estimated using the vector which defines the peak magnetic-to-electric dipole locations. This method has been found to be effective, especially for shallow dipping targets. Electric dipoles should be more applicable with highly elongated targets (which appears to be the case in the tailing field example) and when current channeling is the primary response (not tested in this work). Since both dipole inversions can be solved quickly even for large subsurface volumes, both can be performed for complementary information. For example, the magnetic-dipole inversion could be used to determine the center of the plate and the electric dipole inversion for the top edge as was predominantly done in this work.

It should be noted that while the smoothing regularization in the inversion encourages the electric dipole solutions to form closed current systems (see Figures 7-4 and 7-5) the inversion does not force zero divergence which implies that the current system that is solved for may not

be physically realizable. An attempt to apply a soft constraint on the divergence by adding a finite difference approximation of the divergence operator as an additional regularization matrix did substantially lower the divergence of the model but the results were inconsistent and contained significant artifacts. Overall, as the intent of the inversion is to provide fast approximate results to guide further interpretation, the lack of this constraint was not found to be significantly detrimental. A background geological response was also not included as it was not found to be necessary for our area of study (resistive Canadian Shield geology) and the methodology in its current state has only been tested on relatively discrete targets where the background response is negligible (i.e. resistive medium, late-time channel, stripped responses, etc.). A possible solution would be to incorporate a background half-space or layered earth forward model in addition to the 3D-dipole response (Sattel and Reid, 2006; Schaa and Fullagar, 2010) which would increase the generality of the methodology at the cost of increased complexity in the forward operator. Alternatively, this may be unnecessary as the electric and/or magnetic dipoles may be able to reliably fit a background response in addition to the anomalous response. For example, it should be possible to model the response of a conductive half-space using our formulation of electric dipoles as it can also be modelled with a closed current loop (with identical shape to the transmitter loop) which deepens and increases in horizontal dimensions with time (Nabighian, 1979; Nabighian and Macnae, 1991).

In our formulation of the inverse problem, we perform a potential field style inversion on a single-time channel which reduces the ability of the inversion to constrain the depth of the causative features (i.e. loss of time-depth relationships). We alleviate this problem by using potential field style depth weighting which is proportional to the spatial decay of the forward operator kernel. In our experience, if the regularization parameters are carefully chosen (L-curve

analysis) the inverted anomaly depths match the depth of the actual causative features. This problem could also be alleviated by incorporating a reliable starting model into the inverse problem as was suggested by Schaa and Fullagar (2010).

Future work aims to investigate inverting multiple time channels either simultaneously or iteratively and using the differences in both location and amplitude of the predicted current system to estimate the conductivity and the conductivity structure of the subsurface. Furthermore, the method can be extended to airborne data (or any multi-transmitter data) by incorporating primary-field coupling information and to borehole data by modifying the depth weighting to weighting based on the distance between cells and the observation point (Li and Oldenburg, 2000). Lastly, further research is being done into constraining the electric dipole inversion to form a consistent closed loop zero divergence solution.

7.7 Conclusion

Under the quasi-static assumption, the magnetic field measured in the air at any given fixed-time is a potential field and determined by the subsurface current system. Conversely, we can invert measured magnetic fields (at a given fixed time) to determine the causative subsurface current system. In our formulation we approximate these currents with a grid of 3D magnetic (closed loop current) or electric (line current) dipoles which are solved for with a potential field style smooth-model inversion. Currently the methodology has only been tested on relatively discrete bodies within a resistive medium (i.e. negligible background response) but future plans include investigating the potential to generalize the method to allow for an arbitrary background response. Synthetic work using plate models reveals that both electric and magnetic dipoles (magnitude and vector orientation) can reveal significant information about the subsurface

geology. Specifically, magnetic dipoles tend to concentrate near the center of targets while electric dipoles align themselves along the shallowest edge of the target. Orientation information can be estimated from the vector orientation of the dipole moments and/or from the locations of the peak magnetic and electric dipoles.

A field example over a deep mineral exploration target confirmed the conclusions drawn from the synthetic examples and the interpreted results (SW shallow dipping target at a depth of roughly 400 m) were consistent with previous interpretations and drilling. A second example over a near-surface mine tailing highlighted the strength of being able to invert data using either magnetic or electric dipoles. While both magnetic and electric dipole models were able to fit the data, the geological interpretation using the electric dipole model was simpler and was interpreted to be more consistent with the believed geology.

Since the developed inversions can be run in a few seconds even for large subsurface grids both magnetic and electric dipole models can be used and interpreted. This fast approximate 3D inversion can be used as a starting point for more rigorous interpretation and/or, in some cases, as a standalone interpretation tool.

7.8 References

Beran, L., B. Zelt, L. Pasion, S. Billings, K. Kingdon, N. Lhomme, L. Song, and D. Oldenburg, 2013, Practical strategies for classification of unexploded ordnance: Geophysics, **78**(1), E41-E46.

Christensen, N.B. 2002. A generic 1-D imaging method for transient electromagnetic data: Geophysics, **67**, 438-447.

Cox, L. H., G. A. Wilson, and M. S. Zhdanov, 2010, 3D inversion of airborne electromagnetic data using a moving footprint: Exploration Geophysics, **41**, 250–259.

Fullagar, P. K., G. A. Pears, J. E. Reid, and R. Schaa, 2015, Rapid approximate inversion of airborne TEM: Exploration Geophysics, **46**, 112-117.

Haber, E., D. W. Oldenburg, and R. Shekhtman, 2007, Inversion of time domain three-dimensional electromagnetic data: Geophysical Journal International, **171**, 550–564.

Huang, H., and J. Rudd, 2008, Conductivity-depth imaging of helicopterborne TEM data based on a pseudolayer half-space model: Geophysics, **73**(3), F115–F120.

King, A., and J. Macnae, 2001, Modelling of the EM inductive-limit surface currents: Geophysics, **66**, 476–481

Kolaj, M, and R. S. Smith, 2013, Using spatial derivatives of electromagnetic data to map lateral conductance variations in thin sheet models: Applications over mine tailings ponds: Geophysics, **78**, no. 5, E225-E235.

Kolaj, M, and R. S. Smith, 2014, Mapping lateral changes in conductance of a thin sheet using time-domain inductive electromagnetic data: Geophysics, **79**(1), E1-E10.

Kolaj, M, and R. S. Smith, 2014, A multiple transmitter and receiver electromagnetic system for improved target detection: 84th Annual International Meeting, SEG, Expanded Abstracts, 1754-1758

Li, Y., and D. W. Oldenburg, 1996, 3-D inversion of magnetic data: Geophysics, **61**, 394-408.

Li, Y., and D. W. Oldenburg, 2000, Joint inversion of surface and three-component borehole magnetic data: Geophysics, **65**, 540–552.

Liu, G., and M. Asten, 1993, Conductance–depth imaging of airborne TEM data: Exploration Geophysics, **24**, 655– 662.

Macnae, J., R. S. Smith, B. Polzer, Y. Lamontagne, and P. Klinkert, 1991, Conductivity-depth imaging of airborne electromagnetic step-response data; Geophysics, **56**, 102- 114

Macnae, J. C., and Y. Lamontagne, 1987, Imaging quasi-layered conductive structures by simple processing of transient electromagnetic data: Geophysics, **52**, 545–554.

Murray, R., C. Alvarez, and R. W. Groom, 1999, Modelling of complex electromagnetic targets using advanced non-linear approximator techniques: 69th Annual International Meeting, SEG, Expanded Abstracts, 271-274.

Nabighian, M. N., 1979, Quasi-static transient response of a conductive half-space – An approximate representation: Geophysics, **44**, 1700-1705.

Nabighian, M. N., and J. C. Macnae, 1991, Time domain electromagnetic prospecting methods, *in* M. N. Nabighian, ed., Electromagnetic methods in applied geophysics, Applications, Part A and B: SEG, Investigations in Geophysics No. 3, Volume **2**, 427–520.

Oldenburg, D. W., E. Haber, and R. Shekhtman, 2013, Three dimensional inversion of multisource time domain electromagnetic data: Geophysics, **78**(1), E47-E57.

Pasion, L., and D. Oldenburg, 2001, A Discrimination Algorithm for UXO Using Time Domain Electromagnetics: Journal of Environmental and Engineering Geophysics, **6**, 91-102.

Sattel, D., 1998, Conductivity information in three dimensions: Exploration Geophysics, **29**, 157-162.

Sattel, D., 2004, The resolution of shallow horizontal structure with airborne EM: Geophysics, **35**, 208-216.

Sattel, D., and J. Reid, 2006, Modelling of airborne EM anomalies with magnetic and electric dipoles buried in a layered earth: Exploration Geophysics, **37**, 254-260.

Schaa, R., and P. K. Fullagar, 2010, Rapid approximate 3D inversion of transient electromagnetic (TEM) data: 80th Annual International Meeting, SEG, Expanded Abstracts, 650–654.

Smith, R. S., 2000, The realizable resistive limit: A new concept for mapping geological features spanning a broad range of conductances: Geophysics, **65**, 1124–1127.

Smith, R. S., R. N. Edwards, and G. Buselli, 1994, An automatic technique for presentation of coincident-loop, impulse-response, transient, electromagnetic data: Geophysics, **59**, 1542-1550.

Smith, R. S., and A. S. Salem, 2007, A discrete conductor transformation of airborne electromagnetic data: Near Surface Geophysics, **5**, 87-95.

Smith, R.S., and T. J. Lee, 2001, The impulse response moments of a conductive sphere in a uniform field, a versatile and efficient electromagnetic model: Exploration Geophysics, 32, 113-118

Smith, R. S., and T. J. Lee, 2002, The moments of the impulse response: a new paradigm for the interpretation of transient electromagnetic data: Geophysics, **67**, 1095-1103.

Walker, P., and G. F. West, 1991, A robust integral equation solution for electromagnetic scattering by a thin plate in conductive media: Geophysics, **56**, 8, 1140-1152.

Ward, S. H., and G. W. Hohmann, 1988, Electromagnetic theory for geophysical applications, *in* M. N. Nabighian, ed., Electromagnetic methods in applied geophysics: theory, SEG, Volume **1**, 130–311.

Watts, A., 1997, Exploring for Nickel in the 90's, or 'Til Depth us do Part', *in* A.G. Gubins, ed., Proceedings of Exploration 97: Fourth Decennial International Conference on Mineral Exploration, 1003-1014.

West, G. F., J. C. Macnae, and Y. Lamontagne, 1984, A time-domain EM system measuring the step response of the ground: Geophysics, **49**, 1010–1026.

Zhdanov, M. S., 2002, Geophysical inverse theory and regularization problems: Elsevier Science.

Chapter 8

8 Conclusion

8.1 Summary of research findings

The primary goals of this thesis were to 1) develop surveying techniques to improve the near-surface resolution and the depth of exploration of inductive EM methods, and 2) develop efficient and simple-to-use methods for the interpretation of the inductive EM data.

In Chapters 3 and 4, surveying and interpretation methods were developed to provide improved near-surface resolution, specifically in the mapping of a laterally varying conductance. The mapping of a laterally varying conductance is an important step towards the improved characterization of near-surface geological regimes such as in nickel laterite exploration, in the characterization of mine, mill or smelter waste or in the characterization or exploration over variable overburden. The methodologies developed relied on the thin-sheet approximation and the measurement of the vertical spatial derivative using two sensors separated in height. In synthetic and field data, it was found that, similar to potential field methods, the spatial derivative had increased sensitivity to the near-surface. Two related methods were developed one being a simple direct transform of the measured data and the other, a slightly more complicated inversion approach. The direct transform method does not require grid or line data and is simple enough to be performed in the field, but, is less accurate than the inversion method when the

spatial gradient of the resistance is strong and/or when the horizontal magnetic fields are large. To identify potential errors in the direct transform method, two unreliability parameters, which assess the unreliability of the conductance calculated using the simplified solution, were suggested. A vertical spatial derivative survey was performed over an old mine tailing pond and both methods produced similar results (a large roughly N-S resistive zone in the tailings). The location of the zone matched the location of surface vegetation which may suggest it is correlated with favorable growing conditions and/or less conductive or thinner tailings material. Larger conductances in other areas may be related to zones of thicker tailings and/or more conductive material (possibly due to increased metal content).

In Chapter 5, it was recognized that for borehole EM data, the vertical spatial derivative does not need to be directly measured but could instead be estimated using adjacent downhole measurement stations. This allowed the developed methodology to be adopted for borehole EM data where the target could be approximated with a horizontal thin sheet. Moreover, it was shown that the direct transform method (the 'simplified inversion') presented in Chapters 3 and 4 could be generalized to use the vertical derivative of any secondary magnetic field component (or combination). Using the vertical derivative of the magnitude of the magnetic field (the 'full inversion') provided the most robust results. In a field example collected in a borehole a massive sulfide deposit in Sudbury, Ontario, Canada, the estimated conductance values were consistent with previous interpretations and models. This simple and robust conductance estimate is ideal as a first pass estimate for target discrimination, grade estimation and starting values for forward and/or inversion modeling.

Chapter 6 investigates how a multi-transmitter survey (repeating profiles with many transmitter locations) could be used to greatly improve both the resolution of inductive EM methods. The

multiple transmitter data is weighted and summed into a single high S/N ratio composite transmitter. The composite transmitter can be thought of as a post-processing method which uses the collected multi-transmitter data to construct/simulate a transmitter which maximizes the coupling to a particular target. The appropriate transmitter weights to use will depend on the target location and geometry and, as such, different weighting schemes allow for the construction of different composite transmitters, each of which will maximally highlight different targets. The method was successfully tested on both synthetic data and a field example from north east of Sudbury, Ontario, Canada. Target locations and orientations could be accurately determined and the S/N ratio of the composite transmitter was significantly higher than that of traditional methods and was easier to interpret. The methodology provides an alternative strategy for high-finesse surveys in complex conductor environments where many transmitter-to-target coupling angles are required and for deep focused exploration which will be required where deeper targets are being sought

Lastly, in Chapter 7, a general approximate 3D EM inversion was developed. The method relies on the fact that the magnetic field measured in the air is a potential field at any given fixed time. As such, the measured magnetic fields (at a fixed time or frequency) can be inverted for the causative subsurface current system which, in this method, is approximated with a 3D subsurface grid of 3D magnetic (closed loop current) or electric (line current) dipoles. Both the location and orientation of the dipoles can provide detailed information about the subsurface geology, whereby, magnetic and electric dipoles are generally located in the vicinity of the center and top edge of the targets, respectively. In its current state, the 3D dipole inversion can be run on any fixed-loop ground survey and two field examples were studied. In the first field example, ground data from a deep massive sulfide body (mineral exploration target) was inverted and the results

were consistent with the existing interpretation of the body (shallow dipping conductor at a depth of roughly 400 m). A second example over a near-surface mine tailing (same survey data as in Chapters 3 and 4) highlighted the strength of being able to invert data using either magnetic or electric dipoles. This fast approximate 3D inversion can be used as a starting point for more rigorous interpretation and/or, in some cases, as a standalone interpretation tool.

8.2 Future work

8.2.1 Mapping a laterally varying conductance (Chapters 3 and 4)

In Chapters 3 and 4, the conductance (or apparent conductance) was solved for independently at each delay time rather than for a single conductance which is consistent with all delay times. This was done to potentially to track for variations in conductance with time that may be associated with changes in the conductivity with depth. A thin sheet is an idealized parametric model and in reality most geological regimes can be thought of as layered half-space of varying resistivity. After initial excitation of the subsurface with an EM pulse, the subsurface currents diffuse downwards with increasing time. As such, the zone of sensitivity at each delay time is different, whereby, as time increases, the measured magnetic fields have an increased sensitivity to the deeper geological features. Therefore, the developed methods solve for a conductance which represents an equivalent thin sheet for the zone of sensitivity at that particular delay time. In a layered geological regime, the calculated conductance should therefore be thought of as a ‘cumulative conductance’ up to the particular delay-time at which it was calculated (Macnae and Lamontagne, 1987; Nekut, 1987). If the sensitivity function with depth at each delay time could be calculated and the cumulative conductance was solved for at each delay time, then a conductivity versus depth section could be generated. This is the basis of many ‘conductivity-

depth-imaging' routines with the exception that most methods instead solve for a cumulative conductivity. One way to estimate the sensitivity function is to use Maxwell's receding image concept (Macnae and Lamontagne, 1987; Nekut, 1987; Eaton and Hohmann, 1989; Macnae et al., 1991; Eaton 1998) or the depth to maximum current or maximum sensitivity to a layer in a half-space (Fullagar, 1989; Fullagar and Reid 1992; Smith et al., 1994; Christensen, 1995; Fullagar and Pears, 2010). Converting the cumulative conductance into conductivity versus depth using depths calculated from Maxwell's receding image resulted in mixed results. It is suggested that the depth calculation be attempted using an alternative method such as the depth to the maximum electric or magnetic field.

In order to determine the value of the developed methods for mapping the mine tailings pond, the underlying cause in the spatial variability of the conductance should be determined. Whether the conductance variability is controlled due to thickness and/or conductivity variations can be calculated through the conductivity depth imaging future work suggested above. The resulting data can then be used to guide a sampling program to determine the controls (i.e. conductive fluids/minerals) on any observed conductivity variations. Specifically, it would be important to determine the cause of the spatial relationship between areas of low conductance and surface vegetation.

8.2.2 Robust borehole conductance estimate (Chapter 5)

As was mentioned in Chapter 5, the conductance of a body can also be estimated from the time constant and empirical rules. For instance, for a thin sheet, the empirical relationship is $C \approx 10\tau/\mu L$, where L is generally the smallest sheet dimension (Nabighian and Macnae, 1991). As was shown in Chapter 5, it may be possible to estimate L by using an estimated time constant

and the conductance derived from using the direct transform method. To date, this method has only been tested on a single field example and warrants further research.

Another potential area of research on the interpretation of borehole data would be in solving the full thin-sheet equation rather than the simplified uniform sheet equation. As opposed to Chapter 4 where inversion along a grid was required, it may be possible to solve the equation for a single borehole by using multiple readings along that borehole. This would allow for the determination of the resistance derivatives which could be used as guides to find the edges of targets and/or as a vector towards increased conductance (B. Polzer, personal communication). This method was briefly investigated and while it was possible to solve the full equation, the calculated resistance vectors were inconsistent and no general conclusions could be drawn. Further research into this topic is warranted.

8.2.3 Multiple transmitter surveying (Chapter 6)

Resurveying station positions with many transmitter positions results in a large amount of unique data. In this thesis, the data is combined to produce a single high S/N ratio composite transmitter dataset. The main drawback with the current processing/interpretation scheme is the dipole approximation which limits the methodology to cases where the background geological response is negligible (resistive half-space, stripped fields, late time, etc.). The method could be modified to include a more complex forward operator in the coupling calculations to allow for a conductive background but this increases the complexity of the problem. However, it should still be considerably less numerically intensive than a general multi-transmitter 3D EM inversion. Further research into the applicability of the method, or how it can be modified, to include a background response is suggested.

Furthermore, since the near-surface field trial was relatively successful, a full-scale deep field experiment is warranted. In addition, a more rigorous S/N ratio comparison between the small multiple-transmitter method and standard large loop surveys should be performed to determine whether the increase in overall S/N ratio is worth the increase in logistics and cost of the multiple transmitter survey.

8.2.4 3D magnetic and electric dipole inversion (Chapter 7)

Future work should investigate how multiple time channels could be inverted either simultaneously or iteratively in order to track the change in both location and amplitude of the dipoles. Tracking the dipoles in time could be used to determine how the current system changes with time which would reveal significant information about the conductivity and conductivity structure of the subsurface. Furthermore, the method could be extended to airborne data (or any multi-transmitter data) by incorporating primary-field coupling information and to borehole data by modifying the depth weighting to weighting based on the distance between cells and the observation point. Lastly, it may be worthwhile to apply a hard constraint on the electric dipole solution to form a zero divergence current system. This would create more physically realizable current systems which may reveal new uses for the method. However, a hard constraint would make the inversion non-linear which would increase the complexity of the inverse problem.

8.3 References

Christensen, N. B.,1995, Imaging of central-loop transient electromagnetic soundings: Journal of Environmental and Engineering Geophysics, **0**, 53–66.

Eaton, P. A., and Hohmann, G.W., 1989, A rapid inversion technique for transient electromagnetic soundings: Physics of the Earth and Planetary Interiors, **53**, 384–404.

Eaton, P. A., 1998, Application of an improved technique for interpreting transient electromagnetic data: Exploration Geophysics, **29**, 175–183.

Fullagar, P. K., 1989, Generation of conductivity-depth pseudo-sections for coincident loop and in-loop TEM data: Exploration Geophysics, **20**, 43–45.

Fullagar, P. K., and J. E. Reid, 1992, Conductivity-depth transformations of fixed loop TEM data: Exploration Geophysics. **23**, 515–520.

Fullagar, P. K., and P. Glenn, 2010, High resolution conductivity-depth transformation of TEM data: Australian Society of Exploration Geophysics Extended Abstracts 2010. 1-4.

Macnae, J. C., and Y. Lamontagne, 1987, Imaging quasi-layered conductive structures by simple processing of transient electromagnetic data: Geophysics, **52**, 545–554.

Macnae, J., R. S. Smith, B. Polzer, Y. Lamontagne, and P. Klinkert, 1991, Conductivity-depth imaging of airborne electromagnetic step-response data; Geophysics, **56**, 102- 114

Nabighian, M. N., and J. C. Macnae, 1991, Time domain electromagnetic prospecting methods, *in* M. N. Nabighian, ed., Electromagnetic methods in applied geophysics, Applications, Part A and B: SEG, Investigations in Geophysics No. 3, Volume **2**, 427–520.

Nekut, A.G., 1987, Direct inversion of time-domain electromagnetic data: Geophysics, **52**, 1431–1435.

Smith, R. S., R. N. Edwards, and G. Buselli, 1994, An automatic technique for presentation of coincident-loop, impulse-response, transient, electromagnetic data: Geophysics, **59**, 1542–1550.